Universität Zürich^UZH

Department of Geography

# Rock glacier kinematics and driving processes at depth: seasonal to decadal trends in borehole records from the ice-rich Murtèl rock glacier.

GEO 511 Master's Thesis

**Author:** Giulio Saibene, 23-723-109

**Supervised by:** Dr. Isabelle Gärtner-Roer

**Faculty representative:** Prof. Dr. Andreas Vieli

24.04.2025

# Abstract

Understanding rock glacier creep is essential for assessing mountain permafrost change in a warming climate. Although the monitoring of rock glacier creep began about a century ago, most studies have been limited to annual rock glacier deformation measurements at the surface. There is a lack of high temporal resolution data to observe seasonal changes in rock glacier deformation, and even more so at depth. As rock glacier velocity has been added as a parameter within the mountain permafrost ECV, it is important to understand how these surface velocity measurements represent the entire rock glacier movement at depth. The first objective of this thesis is to use the almost 40-year record of borehole temperatures at Murtèl rock glacier to describe the long-term changes in rock glacier permafrost temperatures in relation to climate. The second is to outline the depths at which seasonal fluctuations of rock glacier creep can be observed in a 8-year borehole deformation record. The third is to explore the potential drivers of seasonal rock glacier deformation by combining the borehole deformation data with meteorological and permafrost temperature data.

Murtèl rock glacier is a relatively slow-moving rock glacier in the Engadin region, Switzerland, that has been intensively studied for the past decades. The data used in this analysis comes from the borehole drilled in 1987 focusing on temperatures, the borehole drilled in 2015 focusing on deformation, the surface deformation measurements from the GNSS and geodetic stations, and the *in-situ* meteorological data. Since 1994 the permafrost temperatures at Murtèl rock glacier have been warming at a rapid rate of 0.3°C/year and are well correlated with the MAAT. The borehole and GNSS deformation reveal a consistent seasonal deformation peak in September that is limited to the active layer (AL), with lower winter deformation rates driven by the shear zone. On average, the AL, the ice-rich core and the shear zone make up 20%, 24%, and 56% of surface deformation. The total surface deformation from 2016 to 2023 is approximately 90 cm and the measurements by the borehole and the geodetic station differ only by 2 cm. The surface annual velocity is not always representative of the annual velocity at depth. From the 2016-23 period, 2021 had the lowest annual deformation while 2022 the highest. The winter of 2020-21 was especially snow-rich and the summer mild, while the winter of 2021-22 was snow-poor, and the summer of 2022 was the warmest since 2016. The seasonal response time of the AL deformation after the snow-melt is especially slow, up to one month. The combination of these findings suggests that the thermal conditions are dominant over the hydrological to drive the seasonal acceleration of the AL for Murtèl rock glacier. The high ice-content and slow deformation rates of Murtèl rock glacier limit the extrapolation of such interpretation; however, they show how, for some rock glaciers, the RGV as an ECV parameter might be limited to the signal coming from the AL movement. Future borehole deformation monitoring efforts, such as the one installed at Muragl rock glacier in the summer of 2024, should consider the approaches used in this thesis for future analysis.

# Acknowledgments

First, I would like to acknowledge the support of my supervisor, Dr. Isabelle Gärtner-Roer, and express my gratitude for giving me the opportunity to work on the rich data set from Murtèl rock glacier. I also would like to thank Dr. Isabelle Gärtner-Roer for inviting me to the annual site visit at Murtèl and to present at the DACH Conference in Davos this January. Then, I would like to recognize the many insightful discussions with the faculty representative, Prof. Dr. Andreas Vieli, throughout these nine months of work. I would like to highlight that almost all of the borehole and meteorological data in this thesis would not be available without the effort of PERMOS to install and maintain the stations at Murtèl rock glacier. Dr. Alexander Bast was heavily involved during the PERMOS drilling of the 2015 borehole at Murtèl and kindly allowed me to use his photos in this thesis. Within the PERMOS efforts, Prof. Dr. Jan Beutel installed and collected the GNSS station data to then share it through the PermaSense project. I also would like to acknowledge Dr. Dominik Amschwand for installing the PERMA-XT station on Murtèl and express my gratitude for the exchange of ideas and questions about the Murtèl data. For the stratigraphy cores, Theo Manuel Jenk and Michelle Marie Worek from the Paul Scherrer Institute (PSI) were extremely welcoming in showing me the cores extracted from Murtèl stored at PSI and providing access to the stratigraphy data. Lastly, I would like to thank my friends in the Geography Master thesis room, the members of the Glaciology and Geomorphology Group at UZH, and my family for their continued support.

# Contents

# List of Figures

# List of Tables

# 1 Introduction

## 1.1 Rock glaciers definition and distribution

The origin of the term ‘rock glacier’ was far from immediate consensus. The first references to a rock glacier-like landform called it a ‘*peculiar form of talus*’, ‘*fossil glacier*’, or ‘*rock stream*’ (Spencer, 1900; Brown, 1925; Griffiths, 1958). Cross and Howe (1905) in Colorado were the first to coin the term ‘rock glacier’. A rock glacier is defined as a lobe-shaped creeping body of permafrost that is covered by unconsolidated material (Haeberli, 1985). Permafrost is defined as ground that remains frozen and below $0°$C for at least two consecutive years (Muller, 1947). Rock glaciers are the main landform of mountain permafrost that shapes the long-term evolution of periglacial geomorphology. They are found on slopes where substantial debris accumulation intersects permafrost conditions (Haeberli et al., 2006). The debris may originate from sustained rockfall activity, debris-filled snow avalanches, and rock avalanches (Haeberli et al., 2006). For non-glacially derived rock glaciers, the permafrost ice can develop at depth from within the debris where ground temperatures remain below freezing (Knight et al., 2019). Glacially derived rock glacier ice comes from a degrading glacier that becomes buried from debris (Ishikawa et al., 2001). This type of ice-cored rock glacier contains ice that originates from snow accumulation rather than interstitial water freezing into ice. Other suggested origins of rock glacier ice may be snow avalanches, snow field deposits at the rooting zone of the rock glacier, or ice-cored glacial moraines (Haeberli et al., 2006). The internal structure of a rock glacier is highly dependent on the processes that formed it over thousands of years.

Rock glaciers are found in permafrost conditions and usually below the regional snow line and the equilibrium line altitude (ELA) of glaciers (Haeberli, 1985; Kellerer-Pirklbauer et al., 2012). The lower limit of the mountain permafrost zone is found where the mean annual air temperatures (MAAT) is between $-1°$ C to $-2°$ C (Haeberli, 1985). Mountain permafrost is found with high confidence in areas where the MAAT < $-2°$C and with low confidence when the MAAT > $0°$ C (Cremonese et al., 2011). In drier continental climates the ELA is often at higher elevations, and thus there is a wider elevation range where rock glaciers can develop (Kellerer-Pirklbauer et al., 2012). In the Alps 60% of the permafrost evidence locations are within 2500 and 3000 m a.s.l. (Cremonese et al., 2011). The proportion of mountain permafrost composed of rock glaciers largely depends on the topography. Rock glaciers are creeping bodies, so the slope needs to be between $5°$ and $30°$ (Haeberli, 1985). Most of the rock glaciers in the Alps have slopes between $10°$ and $45°$ (Cremonese et al., 2011). Aspect also seems to play a role in the distribution of rock glaciers as 60% of them in the Alps are found on either North or West facing slopes (Cremonese et al., 2011). Rock glaciers can be classified as *active rock glaciers* if they creep and have ice content; *inactive rock glaciers* if they don’t creep but still have ice content; and *relict (fossil) rock glaciers* which don’t creep and do not contain any ice (Haeberli, 1985). Out of the 4795 rock glaciers inventoried in the Alps 75% of them are relict and only about 400 of them are still intact (Cremonese et al., 2011). The lower limit of mountain permafrost is expected to rise by 170 m per $1^{\circ}$C increase in air temperature (Hoelzle and Haeberli, 1995). Hoelzle and Haeberli (1995) projected a loss of permafrost area of 65% in the Engadin, Swiss Alps, given an increase in air temperature of $3^{\circ}$C by 2100. Compared to the loss of clean ice glacier area in the Alps, this rate is slower because the permafrost ice is better insulated by the surface debris.

## 1.2 Rock glaciers vertical structure

Rock glaciers have a highly heterogeneous internal structure composed of a mixture of rocks, ice, air, and water. Most rock glaciers lack information about the vertical stratigraphy because of the large amount of effort needed to drill in a rock glacier in a non-destructive manner to extract cores. This is about 3-4 times more expensive than destructive or percussion drilling (Noetzli et al., 2021). There are less than 10 stratigraphy records from rock glacier cores and most of them are only from the European Alps (Haeberli et al., 1988; L. Arenson et al., 2002; Buchli et al., 2013; Monnier and Kinnard, 2013; Kenner et al., 2020; Fey and Krainer, 2020). Ground penetrating radar (GPR) has also been used in an attempt to gain knowledge about the internal structure of rock glaciers (Fukui et al., 2008; Monnier et al., 2008; Monnier et al., 2011; Monnier and Kinnard, 2013). Even though this method is more accessible, it only provides information about the location of specific layers or transition zones rather than their composition and structure (Buchli et al., 2013; Merz et al., 2015).

The layer making up the top few meters of a rock glacier is called the active layer (AL). It is active as it seasonally thaws and freezes due to its temperature being highly coupled to the atmosphere (Dobiński, 2020). This layer consists of coarse blocks that create large air voids near the surface and smaller grains lower down closer to the permafrost table (Haeberli et al., 2006). Its depth depends on the local MAAT that controls how far down thawing reaches during the summer (Dobiński, 2020). The bottom of the AL is the depth at which the $0^{\circ}$ C isotherm is found below which the ground remains frozen perennially and permafrost is found (Fig. 1). The AL acts as an insulator with high thermal resistance to the ice-rich core found below. The seasonal temperature fluctuations in the AL are substantially greater than below it (Fig. 2). During the summer, the coarse-blocky AL uses 90% of the incoming solar net radiation through turbulent heat fluxes and only the rest are able to penetrate to the underlying permafrost ice (Amschwand et al., 2023).

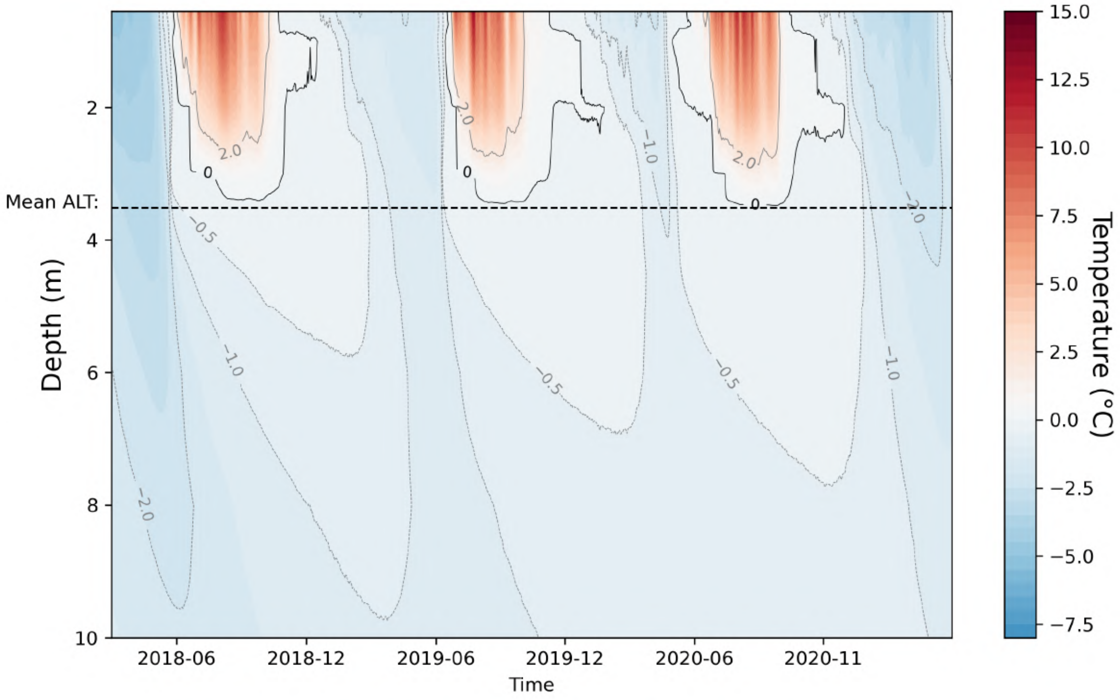

Figure 1: Temperature contour plot from the thermistor chains installed in the 2015 borehole on Murtèl rock glacier. Only years 2018 to 2020 are shown. The mean ALT depth is calculated from the 2016-2023 period.

Below the AL the ice-rich core is found, where the permafrost ice makes up 40-90% of the volume (Cicoira et al., 2021). The debris material in this layer is on average much finer than in the AL (Haeberli et al., 2006). The main control of permafrost temperature is heat conduction, which is exponentially attenuated with depth (Fig. 2). At a certain depth, the penetration of the temperature signal takes more than one year such that intra-annual temperature variations become zero (Dobiński, 2020). This depth of zero annual amplitude is typically found between 10 and 20 m (Cicoira et al., 2021). Temperatures within the permafrost layer stay below 0° C, however, they can approach the melting point under permafrost degrading conditions. This layer experiences different degrees of plastic deformation depending on its ice content, grain size and temperature (Cicoira et al., 2021). However, for some rock glaciers this component of deformation can be negligible (Buchli et al., 2018).

Further down is the shear zone, where most of the deformation occurs (L. Arenson et al., 2002) (Fig. 2). The fraction of surface deformation at this layer can vary a lot even within a single rock glacier. At Schafberg rock glacier in the Swiss Alps the fraction of surface deformation at the shear zone varies from 50% to 97% (L. Arenson et al., 2002). The shear zone is an ice-poor ‘soft’ layer with fine debris that differs drastically from the structure of the adjacent layers. This anisotropy causes strain localization at this zone and explains why most of the deformation occurs here (Moore, 2014). The shear zone typically spans a few meters within the depths of 15 - 30 m (Cicoira et al., 2021). A single rock glacier landform can consist of multiple overriding lobes and thus multiple shear zones at different depths can exist (Merz et al., 2015; Buchli et al., 2018). Information about the shear zone requires the laborious drilling of boreholes to install inclinometers and extract the stratigraphy. The depth of zero annual amplitude is often above the shear zone, so this layer does not experience seasonal fluctuations in temperature. However, on longer timescales changes in temperature in the shear zone may alter the mechanical properties of the material and thereby its deformation. Water has been found in the shear zone and this likely influences its deformation (Ikeda et al., 2008). A higher pore water pressure increases the applied shear stress and, consequently, the strain rates (Nye, 1952; Glen, 1955). Bast et al. (2024) did indeed detect water pressure at depths within the shear zone at Schafberg rock glacier and they suggest that this water must originate from seasonal snowmelt. Understanding shear zone processes is critical to explain the driving factors of rock glacier deformation and so far such studies are scarce.

Below the shear zone and above bedrock there is an ice-poor stiff layer with sediment of varying size which does not deform. Ice may be present in the voids between the coarse debris grains. Water can be found in the form of baseflow from groundwater or taliks (Haeberli et al., 1998; Fey and Krainer, 2020). Taliks are pockets of unfrozen water at depth that can be detected from borehole temperatures that exceed the melting point (Mühll and Haeberli, 1990; Mutter and Phillips, 2012). The Muragl rock glacier is an example in which stratigraphy cores have shown very large air voids present in this layer (L. Arenson et al., 2002). The very high porosity of this layer in some rock glaciers means that if the bottom of the permafrost melted, the resulting meltwater would run off as baseflow and cause a net loss in permafrost volume. However, attempts to measure baseflow at rock glacier outlets reveal that its magnitude is almost not detectable (Amschwand, Tschan, et al., 2024). The bedrock below, depending on the local geology, can be impermeable or fissured, allowing groundwater to infiltrate (Haeberli et al., 1998).

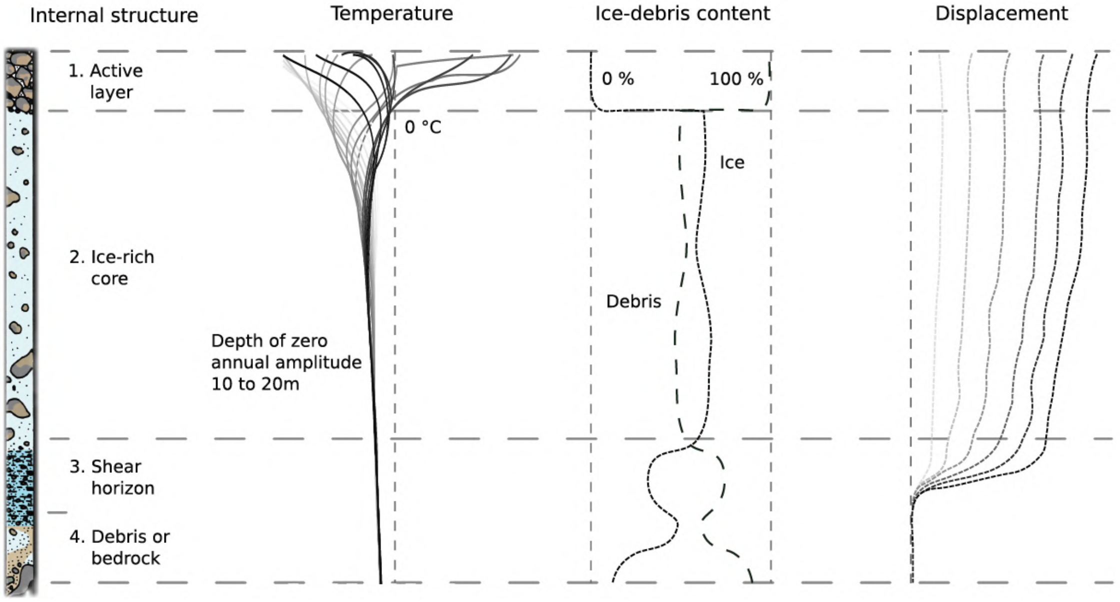

Figure 2: Rock glacier internal structure, temperature profile, ice debris content profile and displacement profile (Cicoira et al., 2021)

## 1.3 Rock glacier creep dynamics

Rock glaciers are a unique landform of permafrost as they deform and flow like a viscous material with gravity. The downslope displacement of rock glaciers acts as a conveyor belt that transports material from the base of rock walls to lower elevations (Haeberli et al., 2006). As mass moves from the rooting zone towards the front of the rock glacier, horizontal compression must be accompanied by vertical extension (*heaving*) exemplified by the alternating transverse ridges and furrows typically found on the surface of a rock glacier. Rock glacier creep varies vertically based on the internal structure. In the active layer the coarse blocks can slip and tilt and contribute to the movement detected at the surface (Cicoira et al., 2021). This is particularly important near the over-steepened front, where mobilization of such loose material during high intensity rainfall events can trigger debris flows (Haeberli et al., 2006). In the ice-rich core plastic deformation can take place depending on the ice-to-debris content ratio. Lastly, at the shear zone substantial shearing occurs which represents the majority of total rock glacier displacement (Haeberli et al., 1998; L. Arenson et al., 2002). Rock glacier creep also varies horizontally based on topography and the morphology of the specific rock glacier lobe. Usually, the highest surface velocities are measured in the lower central part of a rock glacier (Haeberli, 1985). The lowest velocities are found at the rooting zone and around the margins where the thickness is low (Haeberli et al., 2006). Compared to pure ice glaciers, rock glaciers move at much slower rates of a few centimeters per year (Haeberli, 1985; Martin and Whalley, 1987; Kääb et al., 2007).

### 1.3.1 Methods to monitor rock glacier velocity

Rock glacier kinematics has been monitored since the early 1900s (Chaix, 1923). There are four categories of approaches to measure rock glacier velocity: geodetic, GPS, photogrammetry, and inclinometers. Most of the first measurements were carried out with on-ground geodetic measurements. In Alaska, Wahrhaftig and Cox (1959) measured rock glacier displacement by painting markers on large surface boulders and measuring their change in position via on-ground total or theodolite surveys (Haeberli, 1985; Benedict et al., 1986). This was the first method which allowed for a low temporal resolution but spatially distributed record of rock glacier displacement. The use of theodolites allowed for high accuracy of ±0.002 m in the position of the marked boulders (Haeberli, 1985). However, this requires physically visiting the rock glacier during weather conditions with high visibility, thereby limiting the temporal resolution. At Gruben rock glacier, in the Swiss Alps, the first seasonal velocity patterns were assessed due to more frequent field visits every three months (Haeberli, 1985).

Eventually in the early 2000s automatic GPS stations started being installed on rock glacier surfaces to provide higher temporal resolution up to a measurement per minute and only require yearly visits to perform maintenance (Lambiel and Delaloye, 2004; Krainer et al., 2015; Kenner et al., 2020; Cicoira et al., 2022; Kellerer-Pirklbauer et al., 2024). A successful case study of implementing this technology is the PermaSense project which installed 54 wireless GNSS stations in periglacial landscapes around Switzerland to provide close to real-time monitoring of mountain permafrost landforms (Cicoira et al., 2022). The ability to remotely monitor the displacement of rock glaciers has important applications for natural hazard warning systems.

The third approach, which began in the European Alps, was aerial photogrammetry. One of the first records of this method being used was by Barsch and Hell (1976) who looked at the movement of surface boulders from aerial photographs of Murtèl rock glacier from 1932, 1955 and 1971 to estimate rock glacier displacement. The spatial resolution of this method was limited to ± 0.5 m in the vertical direction and ± 0.7 m in the horizontal direction (Barsch and Hell, 1976). More recently, aerial photogrammetry techniques, such as structure from motion, started being used to construct digital terrain models (DTMs) to then extract fully spatially-distributed rock glacier displacement from multiple DTMs over time (Messerli and Zurbuchen, 1968; Kääb et al., 1997). The use of UAVs (unmanned aerial vehicles) to capture aerial images of rock glaciers has drastically improved the spatial resolution of DTMs to then use image correlation analysis to extract surface velocities (Bearzot et al., 2022; Crivelli, 2024).

Lastly, the fourth approach is the use of inclinometers that are placed in boreholes drilled into rock glaciers that collect deformation data. The first borehole drilled with the aim of measuring deformation was drilled in 1987 on Murtèl rock glacier (Haeberli et al., 1988). This method, for the first time, provides deformation data distributed also in the vertical direction with depth.

This, in combination with knowledge about the internal structure, advanced the understanding of the kinematic processes below the surface of rock glaciers. As the magnitude of rock glacier displacement is much lower than that of clean ice glaciers, such boreholes can survive for several months up to decades. However, drilling in rock glaciers is very costly and requires a large amount of effort (Noetzli et al., 2021). As a result, up to 2006 there have only been 15 boreholes drilled in Swiss rock glaciers (Haeberli et al., 2006). In the Global Terrestrial Network for Permafrost database there are 18 boreholes drilled in rock glaciers (Biskaborn et al., 2019). Most of them are installed solely for the purpose of measuring temperature, and only four rock glacier boreholes have published deformation data from inclinometer measurements (L. Arenson et al., 2002; Buchli et al., 2013; Fey and Krainer, 2020). This exemplifies the value of such rock glacier borehole deformation measurements for which this thesis will focus on.

Rock glacier velocity (RGV) has been added as a parameter to the GCOS Mountain Permafrost Essential Climate Variable (ECV) as of 2021 (Delaloye et al., 2021). This means that GCOS, GTOS, and GTN-P have recognized it globally as an important climate indicator within the realm of permafrost along with the active layer thickness, and temperature parameters of permafrost (Delaloye et al., 2021). RGV as an ECV parameter is defined as a spatially averaged horizontal surface velocity of the entire rock glacier (Kellerer-Pirklbauer et al., 2024). Numerous studies have found correlations between annual RGV and mean annual air temperature (MAAT) (Kääb et al., 2007; Delaloye et al., 2010; Buchli et al., 2018). However, not all rock glaciers respond similarly to external drivers. Kellerer-Pirklbauer et al. (2024) correlated annual trends in RGV between different rock glaciers in the Alps and found that there are only 15 rock glaciers out of 50 that correlate significantly with at least 60% of other rock glaciers. The authors defined a threshold of correlating with less than 10% to classify a rock glacier as an outlier in terms of its velocity behavior (Kellerer-Pirklbauer et al., 2024). These statistical results show that RGV can be a good ECV if taken as a regional large-scale average. However, the velocity of one single rock glacier should be checked in context with other rock glaciers before considering it a climate indicator.

### 1.3.2 Timescales of rock glacier creep

Rock glacier creep can be studied at a wide variety of timescales. At a millennial timescale kinematic studies give insight into the origin of rock glaciers or how they eventually become relict (Frauenfelder and Kääb, 2000). On a decadal timescale, changes in the climate and thermal regimes of rock glaciers can be inferred from changes in long-term velocity (Kääb et al., 1997; Roer et al., 2005). At an interannual or seasonal scale, RGV is related to the fundamental mechanism that causes rock glaciers to move in the first place (L. Arenson et al., 2002; Wirz et al., 2016). Most rock glaciers in temperate climates exhibit a strong seasonal cycle (Wirz et al., 2016). During spring, when the seasonal snowpack begins to melt, the inflow of meltwater and the increase in ground temperatures start the yearly acceleration of rock glacier velocity. The period in which the ground temperature remains constant at 0°C due to the latent energy from the melting snow or ice is called the *spring zero curtain* (Hinkel and Outcalt, 1994). Once the snow or the AL ground ice melts away, its insulating effect disappears and the increased air temperatures are allowed to penetrate into the rock glacier permafrost. The increase in ice temperature at depth induces viscosity-driven creep, however, this is believed to have an influence on creep mostly at timescales greater than a few years (Mühll and Haeberli, 1990; Roer et al., 2005). The production of meltwater runoff is also known to drive seasonal acceleration in RGV (Wirz et al., 2016; Cicoira et al., 2019; Kenner et al., 2020). The duration of the spring zero curtain is an important proxy for the magnitude of meltwater production. After the seasonal melt, the rock glacier creep accelerates until the maximum annual velocity occurs in autumn or sometimes in early winter.

Toward the end of autumn the surface begins to freeze again as the air temperature cools and the snow begins to fall. The freezing period of the AL is called the *autumn zero curtain* as the temperature remains at 0°C due to latent heat effects. The date when this happens is important because it signifies the onset of the AL seasonal ground ice and then the snowpack which insulates the underlying permafrost. The later the onset of the autumn zero curtain occurs, the more time the cold air temperatures in the early winter have to penetrate into the exposed rock glacier surface and cool the permafrost ice (Hoelzle et al., 2002). For years when the early winter snow is poor, winter minimum permafrost temperatures occur earlier and are more pronounced (Kenner et al., 2020). So, a late start to the freezing of the AL and insulation by snow cover likely means that the acceleration of the following year will be slower as the ice will be colder. On the other hand, an early autumn snow storm anticipates the beginning of the autumn zero curtain, and then deep permafrost temperatures will remain milder during winter (Mühll et al., 1998). After the AL is fully frozen and the autumn zero curtain has ended, the rock glacier begins to decelerate during the winter until the snow starts to melt again. Whereas the snowpack characteristics or the summer temperatures are the dominant driver of the annual maximum RGV is still a topic of debate (Kenner et al., 2020; Crivelli, 2024).

## 1.4 Rock glacier hydrology

Rock glaciers can be an important source of freshwater as clean ice glaciers continue to melt and some transition to rock glaciers. So, the hydrological role of rock glaciers will become increasingly valuable in the future (Bolch and Marchenko, 2009; Millar and Westfall, 2008). The discharge outflowing from the front of a rock glacier is derived from different sources. Isotope studies suggest that outflow from a rock glacier is composed of 32-38% baseflow of groundwater, 30% seasonal snowmelt, only 2.3% from permafrost ice melt, and the rest is unclear (Williams et al., 2006; Krainer and Mostler, 2002). The baseflow originating from permafrost ice melt was measured to be much lower than 3 L/min at the front of Murtèl rock glacier (Amschwand, Tschan, et al., 2024). The water from snowmelt or rainfall mostly runs off over the permafrost table, which explains the flashy hydrographs measured at rock glacier outlets during summer rainfall events (Amschwand, Tschan, et al., 2024).

Until a decade or so ago, the general consensus was that very little to no water was able to infiltrate into the permafrost ice-rich core of a rock glacier (Krainer and Mostler, 2002). However, some studies suggest that a temporary channelized drainage system may exist in a rock glacier ice-rich core (Krainer and Mostler, 2002; Mutter and Phillips, 2012; Wirz et al., 2016; Amschwand, Tschan, et al., 2024). Krainer and Mostler (2002) measured water temperatures at the outflow of a rock glacier to be lower than 1°C during the melt season, indicating that the water must have flowed while in contact with ice. They also carried out a tracer experiment and measured water flow velocities through the rock glacier of 0.9 - 5.5 m/min which is in the range of channelized flow speed. Mutter and Phillips (2012) found deep seasonal taliks with above freezing temperatures that formed a few days after the onset of the seasonal melt, also suggesting the rapid transport of water within the rock glacier. L. U. Arenson et al. (2022) claim that discontinuous patches of warmer permafrost creating intrapermafrost taliks may contribute to the formation of temporary preferential channelized flow paths. During borehole drilling at Murtèl rock glacier pressurized water has been observed shooting out of the borehole at 5 m and also down at 20 m (L. Arenson et al., 2002). There is strong evidence that during periods of large water inflow, the rock glacier develops a drainage system that behaves similarly to that of a pure ice glacier. This could have important implications for understanding the drivers of seasonal rock glacier acceleration.

### 1.4.1 Measuring water content in a rock glacier

The amount of liquid water within a rock glacier ice-rich core is difficult to measure directly and has been estimated mostly indirectly. For example, Amschwand, Tschan, et al. (2024) calculated a lower ice infiltration capacity than the ice melt rate in the AL and thus assumed that water should be able to infiltrate into the permafrost ice. Measurements of temperatures above freezing within a rock glacier ice-rich core can only be a proxy for the presence of liquid water. There are two more direct methods to measure water content in the ice-rich core of a rock glacier: electrical resistivity tomography (ERT) and piezometric pressure measurements. Bast et al. (2024) have been the only ones to have installed piezometers in shallow rock glacier boreholes to measure the piezometric pressure. They found a patch at 6 m depth with positive pore water pressures at Schafberg rock glacier indicating the presence of water. ERT, on the other hand, measures the electrical properties of a medium which for an ice-debris mixture is related to its water content, porosity and state of matter (Emmert and Kneisel, 2017). Resistivity values lower than around 7-8 kΩm indicate an unfrozen state (Emmert and Kneisel, 2017). At Schafberg rock glacier there are low resistivity values at around 7 - 10 m, even though the temperature is below freezing (Phillips et al., 2023; Bast et al., 2024). The combination of internal structure, short-term kinematic, thermal and hydrological processes is the foundation of this thesis.

## 1.5 Motivation and research questions

Rock glacier boreholes have a life span that can range from months to decades depending on the magnitude of the deformation, which bends and eventually destroys the borehole. Murtèl rock glacier is unique as it only moves about 10 cm a year, whereas most rock glaciers in the Alps move at a few decimeters to a meter per year (Kellerer-Pirklbauer et al., 2024). For this, Murtèl has the longest standing record of borehole temperature data with the first borehole drilled in 1987 which has been running for almost 40 years. There are a few other rock glaciers in Switzerland that have active borehole thermistor chains since the early 2000s; however, before the 1990s Murtèl is alone (Noetzli and Pellet, 2024). At Murtèl rock glacier the PERMOS weather station has also been running since 1994. This gives an opportunity to have a substantially large sample at a timescale usually considered for climate studies. For this, the first research question of this thesis is: **what are the long-term trends in the thermal regime and climate of Murtèl rock glacier?** This first objective also sets the temporal context for the later short-term analysis. The long-term signals can often behave differently than the short-term patterns.

Although rock glacier kinematic studies are abundant, those that have vertically distributed data on the deformation and internal structure of a rock glacier are very rare. There are only four rock glaciers (Furggwanghorn, Murtèl, Muragl and Schafberg) with boreholes measuring deformation (L. Arenson et al., 2002; Buchli et al., 2013). The inclinometer installed in the most recent borehole at Murtèl rock glacier gives an opportunity to assess how rock glacier deformation varies with depth at a high temporal resolution. Most rock glacier kinematics studies are limited to using surface velocity measurements, often from GNSS or photogrammetry, and assume that surface velocity is representative of the velocity at depth. A vertical deformation profile offers valuable insight needed to evaluate this assumption, addressing the second research question: **what are the main spatial and temporal patterns in the vertical deformation profile of the Murtèl rock glacier?**

As rock glacier velocity (RGV) is a parameter within the ECV of Mountain Permafrost it is important to know what the external drivers of RGV are. It is still unclear why different active rock glaciers react differently to climate changes (Kellerer-Pirklbauer et al., 2024). In order to understand the controlling processes of rock glacier deformation, high temporal resolution deformation data is needed to resolve short-term fluctuations. There are a multitude of studies with high-frequency surface RGV data, however, only Buchli et al. (2018) have so far examined seasonal patterns in rock glacier deformation with depth. However, due to the high deformation rates, the life span of the Furggwanghorn boreholes was only up to 10 months (Buchli et al., 2018). The inclinometer data from Murtèl rock glacier lasts for over seven years consisting of daily measurements down to 40 m. The rich data set available at Murtèl can be used to improve the understanding of the dominant processes controlling its kinematics at short timescales. This thesis aims to answer the third question of: **what are the controlling processes of the interannual to seasonal fluctuations of the borehole deformation of Murtèl rock glacier?**

# 2 Study site

## 2.1 Murtèl rock glacier

As the aims of this thesis are largely about process understanding it requires a site with sufficient data and Murtèl rock glacier offers just that. Murtèl rock glacier is located in southeastern Switzerland in the region of Engadin (see Fig. 3) and its one of the most studied rock glaciers in the Alps (Haeberli et al., 1988; Mühll and Haeberli, 1990; Haeberli et al., 1998; Mühll et al., 1998; Hoelzle et al., 1999; Mittaz et al., 2000; L. Arenson et al., 2002; Haeberli et al., 2006; Hoelzle et al., 2022; Noetzli et al., 2021; Amschwand, Tschan, et al., 2024; Amschwand, Wicky, et al., 2024; Kellerer-Pirklbauer et al., 2024). Its rooting zone starts at 2800 m under the prominent rock wall of Piz Corvatsch. The frontal margin is found at 2640 m and in total the rock glacier is 0.08 $km^2$ large, 450 m long and 200 m wide and it faces NW. Murtèl is a single lobe rock glacier with a slope of $20°$ in the upper part and $10°$ in the lower part (Kääb et al., 1997). Near its front in the center the typical surface ridge-furrow topography features can be seen as evidence of compressional flow (Fig. 3). The mean annual air temperature (MAAT) at this location is $-1.5°$C which is within the lower limit of $-2°$C to $-1°$C for the occurrence of mountain permafrost (Haeberli, 1985). The mean annual precipitation of the Engadin region is 1000-1200 mm and typical annual maximum snow cover is of 1-2 m (Schwarb et al., 2000; Scherler et al., 2014; Hoelzle et al., 2022).

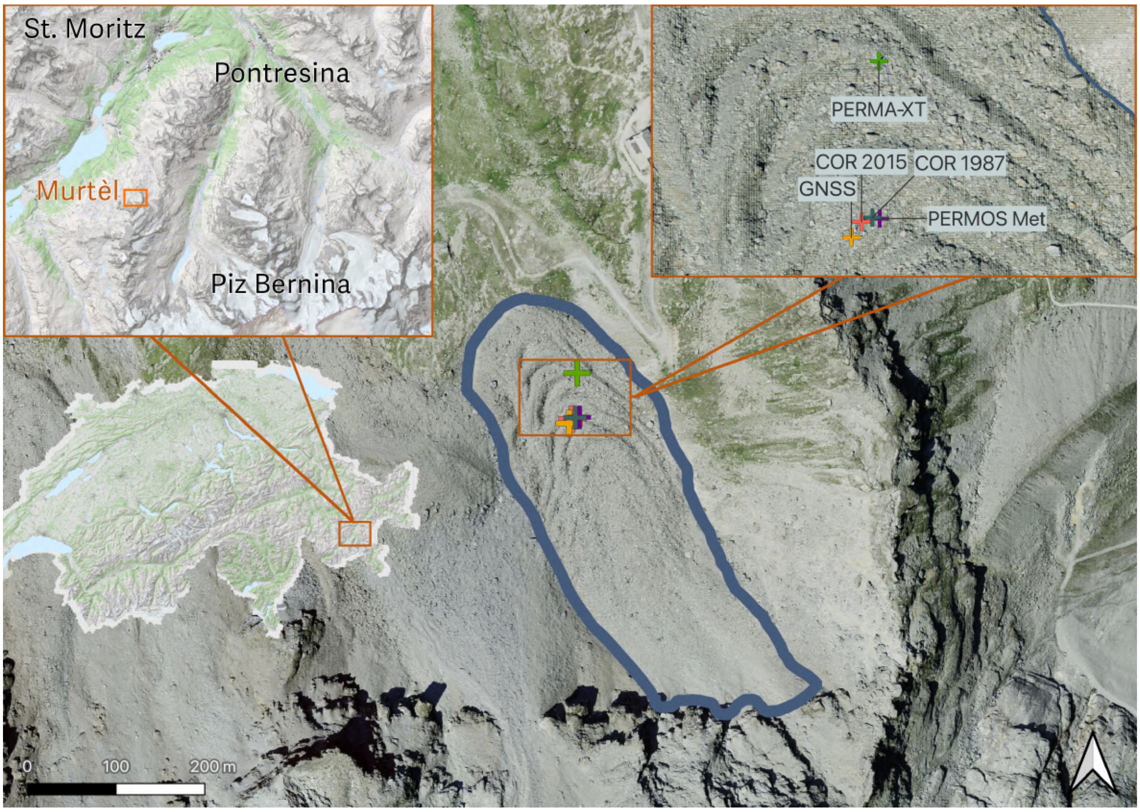

Figure 3: Study site of Murtèl rock glacier (blue outline) with the locations of the two boreholes (COR 1987 and 2015), the GNSS station and the two meteo stations (PERMOS and PERMA-XT). Orthophoto derived from SwissTopo.

Murtèl rock glacier has been a hotspot of mountain permafrost research largely due to its accessible nature thanks to the Piz Corvatsch cable car, which can also be used to transport heavy equipment. The first borehole drilled on Murtèl was in 1987 which reached a depth of 60 m (Haeberli et al., 1988). The aim of this borehole was to establish a long term series of mountain permafrost temperatures down to bedrock. The thermistor sensors chains for the first few years had to be taken out to read out the values manually. For years 1987 to 1995 they also had manual measurements of deformation by taking out the inclinometer from the borehole (L. Arenson et al., 2002). The core drilling was non-destructive which allowed for describing the internal structure of Murtèl for the first time (Haeberli et al., 1988). In 1994 an automatic data logger station was set up to record meteorological data continuously (Mittaz et al., 2000). Murtèl is an unusually slow-moving rock glacier, which has allowed most of its sensors to still operate to this day. As a result, it has the longest continuous time series of depth-distributed rock glacier permafrost temperature measurements in the world. After the success of the 1987 borehole campaign two more boreholes were drilled in the spring of 2000. They were drilled upslope by 19 and 32 m relative to the 1987 boreholes (L. Arenson et al., 2002). Unfortunately, the thermistor chains in these newer boreholes were faulty due to unclear reasons (personal communication, 2024). The useful data collected from the 2000 boreholes are the stratigraphy records (L. Arenson et al., 2002). More recently, in 2015 one more borehole was drilled a few meters West of the 1987 borehole (Fig. 3). Its aims are to continue in parallel the long term temperature series from the 1987 borehole. The new borehole has an increased spatial resolution of 0.5 m in the top 5 m of the borehole compared to the 1 m resolution in the 1987 borehole. It also establishes the first continuous record of borehole rock glacier deformation data in Switzerland, which will be the main focus of this thesis. Other than the boreholes Murtèl has an on-site weather station maintained by PERMOS, weather and energy budget station in an AL cavity, annual displacement data measured at 10 points on the surface, and ground surface temperature loggers. All of which will be used to different extents in this thesis and described in more detail in the *Methods* section.

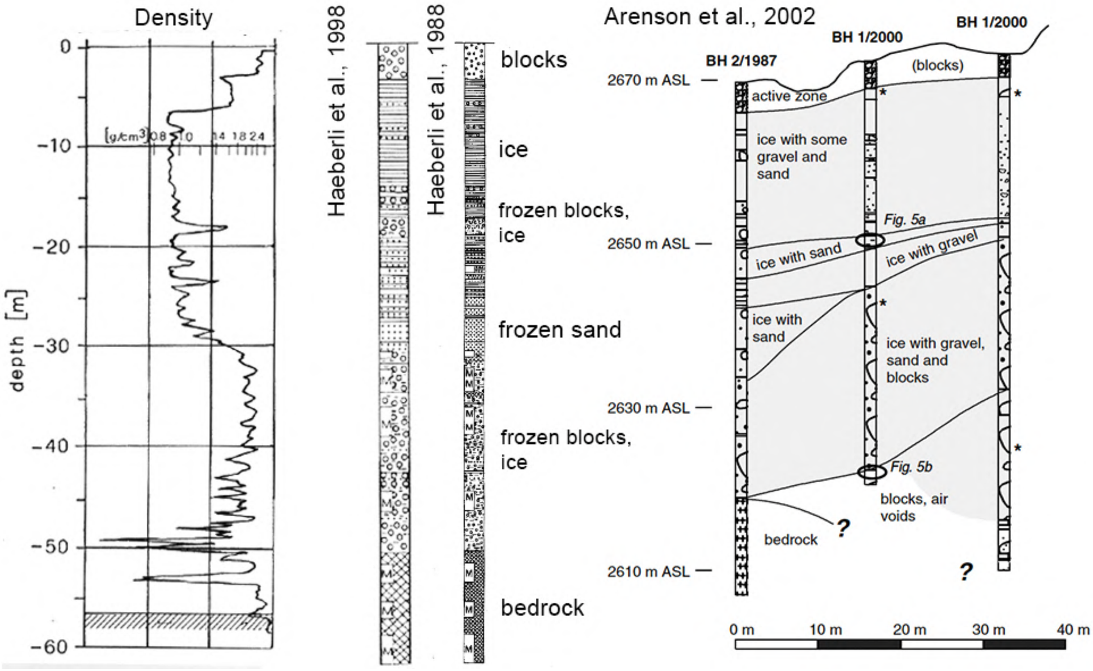

Figure 4: Murtèl internal structure stratigraphy cores from 1987 core drilling (two left columns) (Haeberli et al., 1988; Haeberli et al., 1998) and also two drilled in 2000 on the right (Arenson et al., 2002).

### 2.1.1 Internal structure

The stratigraphy records from the various core drilling campaigns on Murtèl have produced detailed internal structure information. Near the surface, Murtèl has a very coarse-blocky active layer (AL) that is on average 3.5 m thick (Noetzli and Pellet, 2024). The blocks found in the AL have diameters that range from decimeters to a few meters (Scherler et al., 2014). The thickness of the AL varies spatially, for instance, on the ridges it is thicker than in the furrows (Hoelzle et al., 1999). Below the AL there is close to pure ice from about 4 m down to 15 m (Haeberli et al., 1988) (Fig. 4). At about 15-17 m there is some higher debris content as represented by the spike in density in the left plot in Fig. 4. Generally from 15 m to 28 m there is frozen saturated fine debris such as gravel, sand and silt (Haeberli et al., 1988). Below that to 32 m the ice content decreases and density increases. The shear zone is found in this range with lower ice content and more fine debris at about 30 m (L. Arenson et al., 2002). Further down from 32 m to 50 m there are coarser grains with the air spaces mostly filled with ice (Haeberli et al., 1988). The permafrost extent is said to be down to 51 m (Mühll and Haeberli, 1990). There has been a subpermafrost talik found at 51 m to 57 m where seasonal variations in temperature exceeded 0°C (Haeberli et al., 1998; Mühll et al., 1998). The bedrock is found at about 60 m deep and is considered to be relatively permeable and fissured (Haeberli et al., 1988). The internal structure and mechanical properties of different layers are important in determining at what depth deformation occurs.

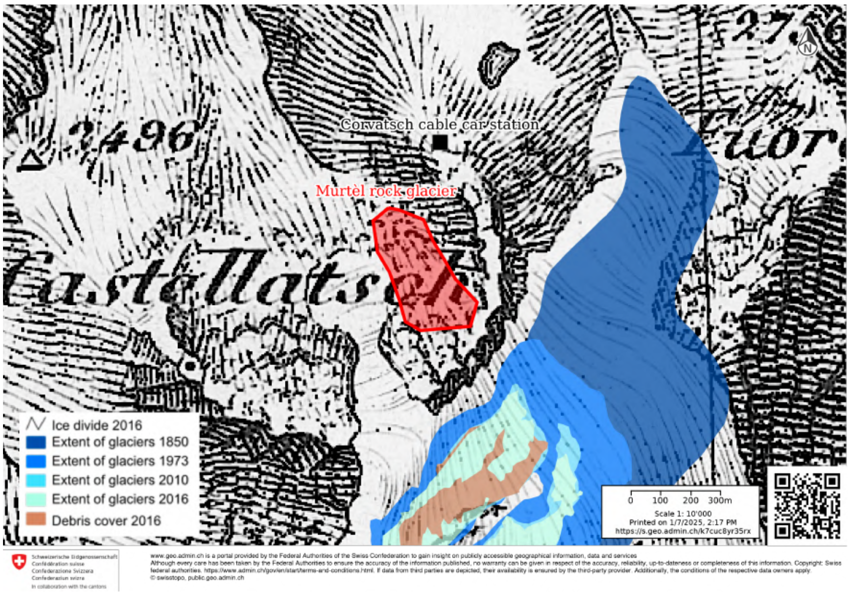

Figure 5: The first edition of the 1864 Dufour Map with the historical recontruction of the glacier extent back to 1850.

The origin of the 4 - 28 m ice in Murèl rock glacier is still up to debate, as it could either be talus-derived permafrost or of glacial origin. The purity and lack of debris from 4 - 15 m would suggest that it is from glacial origin, however, by inspecting historical maps from 1864 the glacier extent did not overlap with the area of Murtèl rock glacier (Fig. 5). The modelled permafrost and glacier distribution by Hoelzle and Haeberli (1996) also supports that at least since 1850 there likely was no glacier where Murtèl rock glacier is located today (Fig. 6). Moreover, Haeberli and Mühll (1996) found a chemical signature in the Murtèl ice to be more similar with that of refrozen groundwater rather than atmospheric precipitation. From the more recent 2015 borehole on

Murtèl C-14 dating analysis of the ice core revealed one core section at about 25 m depth to be around 9000 years old (source). If the ice of such age then it would suggest that the possibility of it being glacial ice is not to be ignored. Part of the implication of more knowledge about the vertically-distributed deformation is to re-build the origin story of rock glaciers and enhance theories about how rock glaciers were formed, but this is outside the scope of this thesis.

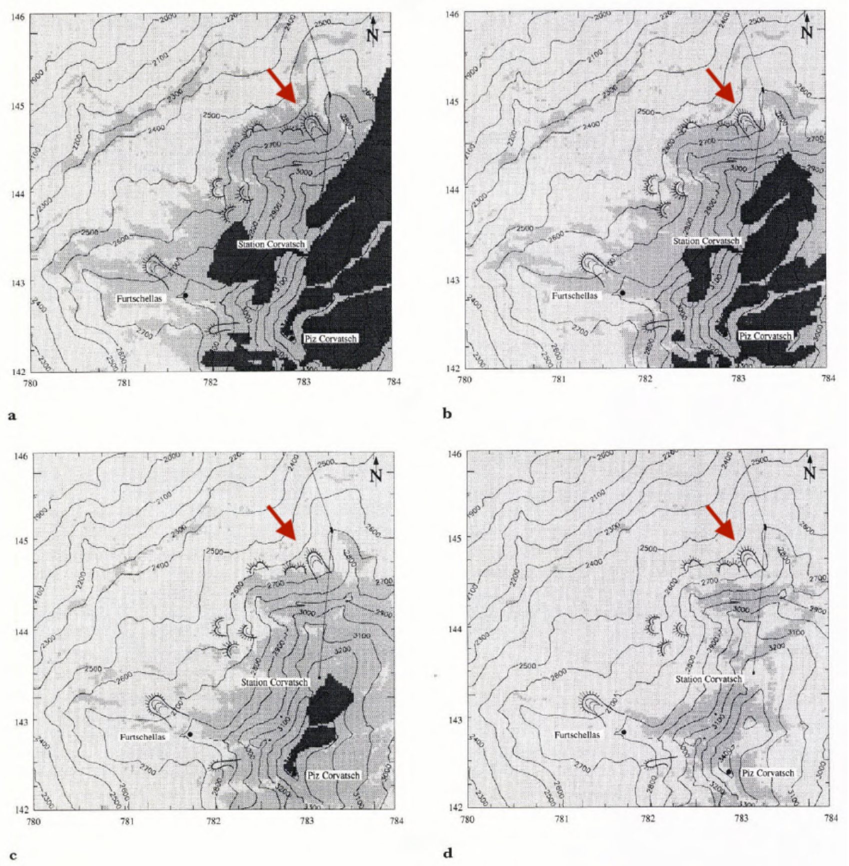

Figure 6: Estimated extent of permafrost (dark grey) and glacier area (black) for: a) 1850 reconstructed by Maisch (1992); b) 1990; c) 2025; d) 2100. Red arrow indicates position of Murtèl rock glacier. Adopted from Hoelze and Haeberli (1996).

### 2.1.2 Kinematics

Murtèl rock glacier, when compared to nearby rock glaciers, has unique kinematics. It is the slowest rock glacier out of the five well-monitored rock glaciers in the Engadin region (Kellerer-Pirklbauer et al., 2024). Murtèl moves horizontally about 10 cm/year on average, while the other nearby rock glaciers move about 40 - 140 cm/year (see Fig. 7). The other slow rock glacier in 7 is Marmugnun rock glacier which is located just west of Murtèl rock glacier. There is a third rock glacier in the same cirque further west that is Chastelets, which interestingly has substantially larger velocity than the other two (Durisch, 2023). In the period where the five series overlap the pattern in RGV varies between rock glaciers (see Fig. 7). In fact, Kellerer-Pirklbauer et al. (2024) correlated annual RGVs between all long-term monitored rock glaciers and found that Murtèl is one of three Swiss rock glaciers that correlates with less than 10% of the other rock glaciers in the Alps. This is an important caveat to acknowledge when extrapolating the processes controlling the velocity of Murtèl rock glacier to other rock glaciers.

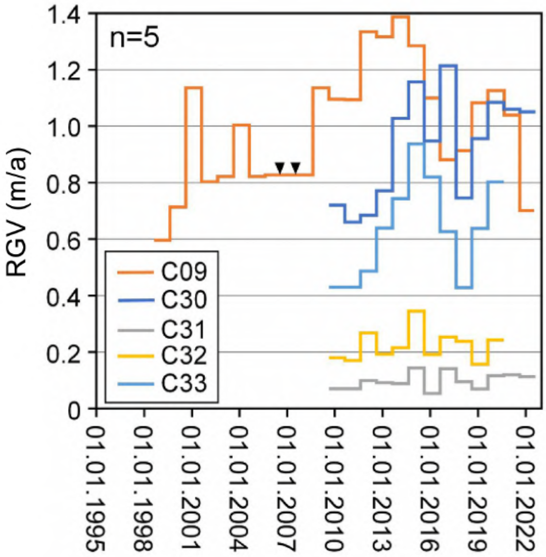

Figure 7: Annual average rock glacier velocity (RGV) for five rock glaciers in the Engadin region in Switzerland. C09: Büz North, C30: Muragl, C31: Murtèl, C32: Marmugnun, C33: Chastelets rock glacier. Retrieved from Kellerer-Pirklbauer et al., 2024.

Murtèl rock glacier is formed by one tongue-shaped lobe that is flowing as one body (Fig. 8). Its upper steeper part below the rooting zone experiences longitudinal extension which is associated with AL thinning, while the lower less steep part near the front consists of longitudinal compression causing the stiff blocky AL to fold and create the typical ridge-furrow surface topography features near the front (Haeberli et al., 1998). The location of both the 1987 and the nearby 2015 borehole are located within this lower zone of horizontal compression with relatively lower horizontal surface velocity (Fig. 8).

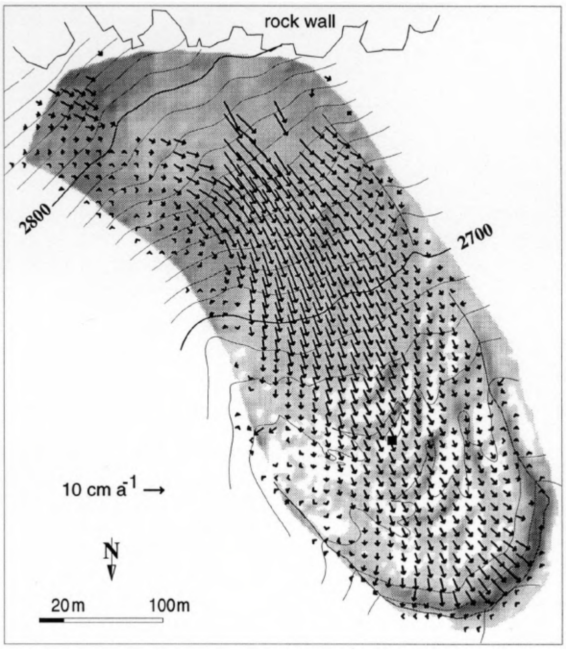

Figure 8: Horizontal surface velocity field of Murtèl rock glacier derived from photogrammetry techniques with images from 1987 and 1996. The location of the 1987 borehole is marked by the black square. Derived from Kääb et al., 1998.

The long term trends in the surface velocity of Murtèl rock glacier have been analyzed by performing co-registration on historical orthophotos from SwissTopo and summarized by Durisch (2023). The oldest image used is from 1955. The results confirm that even on longer timescales, on average, the surface of Murtèl moves on a scale of a few decimeters per year (Durisch, 2023). Murtèl had experienced some acceleration with annual velocities over a meter per year during the 1970s and 80s. After 1985 Murtèl slowed down to its present average magnitude of 10 cm/year movement. The historical reconstruction of velocity from orthophotos from 1985 to 1998 produced similar velocities compared to the deformation measured from 1987 to 1995 at the surface by the inclinometer installed in the 1987 borehole (L. Arenson et al., 2002; Durisch, 2023). This is an indication that the location of the borehole has evidence to be representative of the average surface velocity of Murtèl. The new 2015 borehole has been drilled to renew the deformation record which ended in 1995 and will be the focus of this thesis.

# 3 Methods

## 3.1 The boreholes instrumentation and processing

After the successful borehole installation back in 1987 which is still recording temperature data down to 53 m to this day, a new 60 m deep borehole was drilled in September and October 2015 a few meters away from the old borehole (Fig. 9). This new borehole reinforces the long-standing temperature record at Murtèl while also adding novel continuous rock glacier deformation data. The instruments installed in the 2015 borehole on Murtèl rock glacier are three thermistor chains and an inclinometer chain. Data from both boreholes will be assessed in this thesis.

Figure 9: Photograph of the instruments on Murtèl rock glacier with starting from the left: the new 2015 borehole (red arrow), the GNSS station with its solar panel, the 1987 borehole (red arrow), data logger and solar panels, and the PERMOS meteo station (very right). Photo source: Noetzli et al. (2021).

### 3.1.1 Thermistor chains

The thermistor chains in the 1987 borehole will be used for long-term analysis. For most sensors there is a continuous record of temperatures since 1994 until the end of 2008 when around two-thirds of the sensors stopped working (Fig. 11). The sensors are located every one meter until depth of 21.5 m where there is a two-meter gap and then from 23.5 to 27.5 m there is again a sensor every meter. Between 27.5 and 29.5 m the spatial interval goes back to two meters. After that there is a sensor every meter until 31.5 m, then a 1.5 meter gap. The next three sensors are found every three meters. The last cluster of sensors from 45 to 58 m are spaced one meter apart (Fig. 10). The second part of the thesis will focus on the 2016-23 period, using the three 60 m long thermistor chains in the 2015 Murtèl borehole, covering a total of 38 depths (Fig. 10). The sensors are placed with non-uniform spacing to produce higher spatial resolution within the more relevant depth ranges. In the top 1 m the sensors are spaced by 25 cm. From 1-5 m there is a sensor every 50 cm. Then until 20 m the sensors are spaced by 2 m. There is a sensor at 25 m and then from 28-42 m there is a sensor every 2 m. The last sensors are located at 45, 50, 55, 58 and 60 m. Across the three different chains, the sensor depths are staggered, except at the depths of highest relevance for permafrost monitoring where sensors are found in multiple chains to provide redundancy (Fig. 10, Appendix 8.1). The sensors used to measure temperature are NTC high resistance YSI 46031 thermistors (ALPUG, 2015). They are calibrated in a double ice-water bath with a reference thermometer and have an accuracy of ± $0.02°$C (ALPUG, 2015; Noetzli et al., 2021). The time interval is one day and measurements start on the 2016-01-06 and end on 2023-11-23. Some of the sensors have stopped working, but the majority are still functional (Fig. 12).

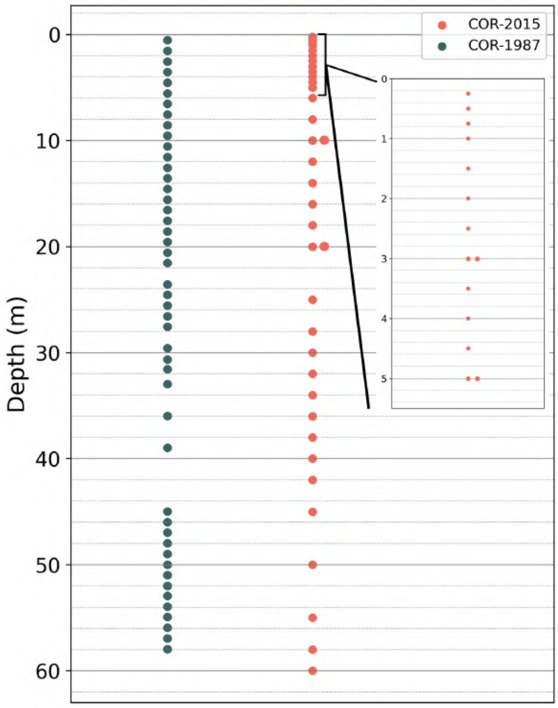

Figure 10: Vertical spatial distribution of thermistor sensors for the COR-1987 borehole and the COR-2015 borehole on Murtèl rock glacier. For the latter, all sensor positions from the three chains are shown and depths with replicated sensors have two circles drawn.

Figure 11: Data availability of each thermistor sensor in the 1987 borehole.

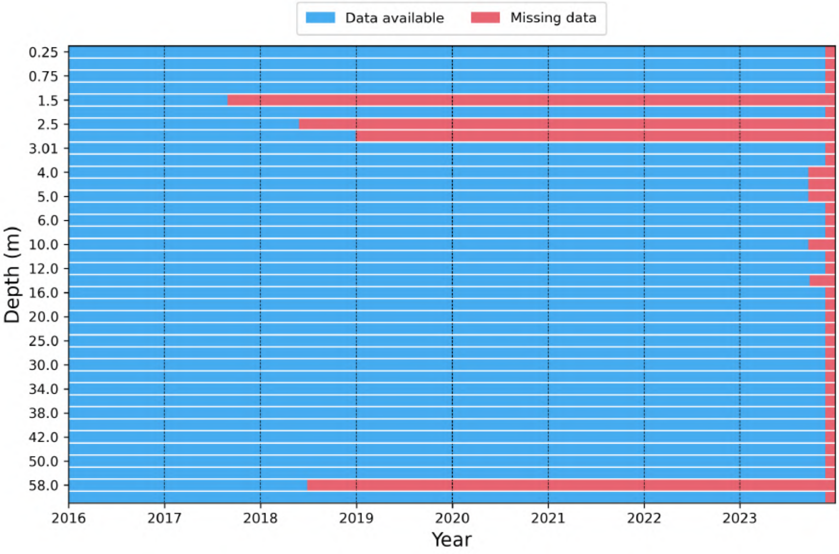

Figure 12: Data availability of each thermistor sensor in the 2015 borehole.

### 3.1.2 Inclinometer

In the middle of the three thermistor chains, a ShapeAccelArray (SAA) field inclinometer is placed. The inclinometer is made up of 50 cm long rigid segments held together by flexible joints. In each segment, triaxial MEMS gravity sensors measure the tilt angle. As the inclinometer is inserted vertically into the rock glacier the tilt angle measured gives an indication of the horizontal deformation. A relative vertical component can still be extracted. The maximum tilt angle in the vertical direction is $\pm 60°$. The conversion from tilt angle to deformation in the *x, y, z* components is performed by the Measurand software. The SAA sensors also measure temperature. The temporal resolution of the inclinometer measurements is 6 hours. The inclinometer chain is covered with an insulated material and then wrapped with the three thermistor chains (Fig. 13).

### 3.1.3 Borehole drilling and set-up

In late summer 2015, a new borehole was drilled on Murtèl rock glacier. A combination of destructive and core drilling was used to optimize costs. In the top five meters, destructive drilling was done to pass through the blocky ice-poor AL. From 5-30 m, a Triplex drill was used to drill the core non-destructively and extract core sections that are automatically packed with a thin plastic casing and then stored in an on-site freezer (Noetzli et al., 2021). The drilling is done at a slow penetration speed to prevent heat disturbance especially at the higher ice content depths. A compressor-drive air flushing system is used to prevent permafrost ice from melting (Haeberli et al., 1988). The individual cores of typically around 50 cm length were later transported to be sampled at the Paul Scherrer Institute for C-14 dating and isotopes, but this is beyond the scope of this thesis. The cores that contained a substantial ice content were removed from the casing, while those with mainly debris were not. The qualitative stratigraphy descriptions and photos from the cores are then used to construct a visual representation of the internal structure of Murtèl rock glacier.

After drilling is complete, a thin watertight 11 cm wide PVC casing is quickly inserted into the borehole to prevent wall collapse in sections with more loose debris (Fig. 13). The bottom of the casing pipe has a closed cap to prevent groundwater infiltration (Noetzli et al., 2021). Inside the casing the inclinometer-thermistor bundle is inserted and anchored at the top of the borehole (Fig. 13). A concrete surface well protection is placed around the borehole (Fig. 9 and 13). The bottom of this concrete chamber is drainable to prevent the build up of water during melt or precipitation events. The lid of the chamber must be high enough to avoid having the top of the thermistor-inclinometer bundle pressing onto it as the permafrost melts and the surface level subsides. All the thermistors and the inclinometer are connected to an on-site Campbell CR1000 data logger powered by an external battery. The data is transmitted remotely by a GSM network. The borehole was allowed to stabilize for a few months until January 27, 2016 when sand was inserted around the thermistor-inclinometer bundle to ensure thermal and kinematic connectivity with the surrounding rock glacier material.

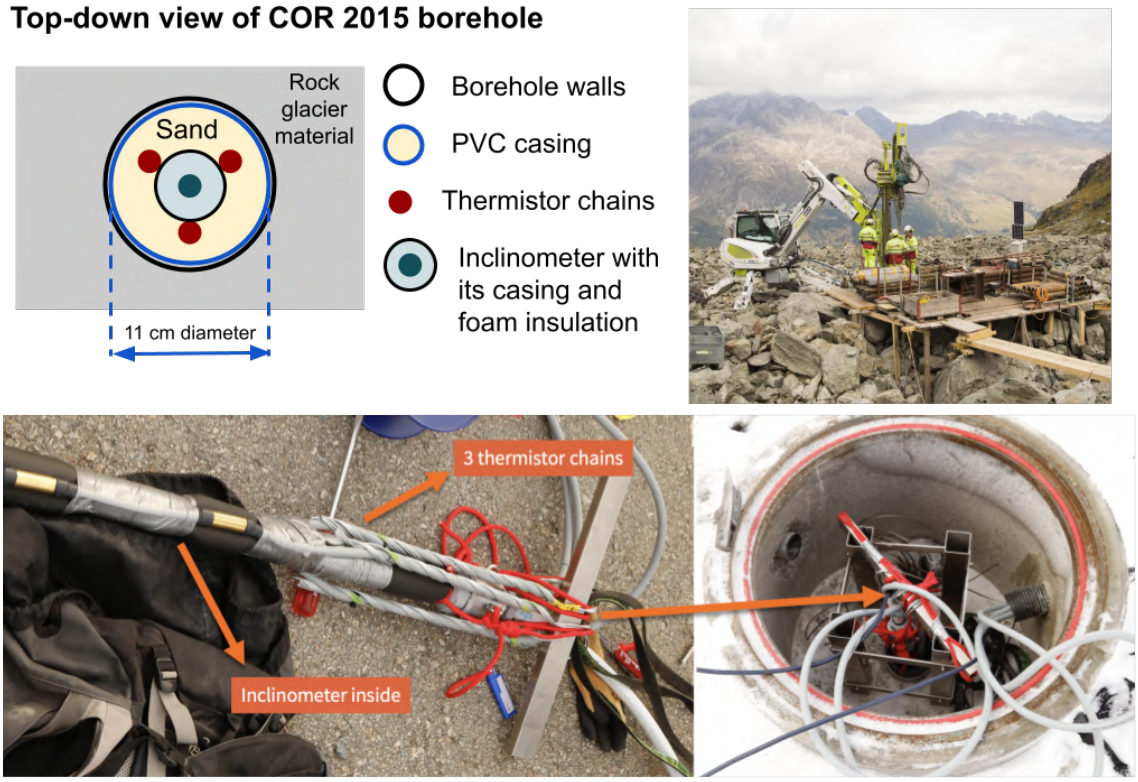

Figure 13: The borehole set up from the 2015 drilling at Murtèl rock glacier. Photos by Alexander Bast.

### 3.1.4 Borehole temperature processing

The borehole temperature data series has many data gaps as seen in Fig. 11 and 12. The sensor at depths above 4 m are relevant for the extraction of the AL. At these depths, data gaps of up to 14 days were filled using linear interpolation. For depths below 4 m data gaps of up to 3 days were filled using linear interpolation. After cleaning the data, the ground heat flux is calculated using the temperature difference between the adjacent thermistor sensors. The Fourier heat conduction equation is used as follows:

$$Q_G(t) = k\frac{dT(t)}{dz}$$

Where the temperature difference for a given sensor at depth $z_i$ is $dT_{z_i}(t) = T_{z_i}(t) - T_{z_{i-1}}(t)$ where $z_{i-1}$ is the sensor at the depth above the sensor at depth $z_i$. The thermal conductivity $k$ is taken to be constant at 2.5 $\mathrm{Wm^{-1}K^{-1}}$ as used by Scherler et al. (2014) and Mühll et al. (1998). Measurements of the thermal conductivity of rock and ice mixtures from a cold lab produced values ranging from 2.3 to 3.0 $\mathrm{Wm^{-1}K^{-1}}$ (Mühll and Haeberli, 1990). The effect of the liquid water content on the thermal conductivity is not taken into account here as it can be assumed that at least in the highly drainable AL there should be no substantial amount of stagnant water present (Scherler et al., 2014).

Active layer thickness (ALT) is calculated using the borehole temperatures. ALT is defined by the maximum depth of the $0°$C isotherm during the warm phase. So, to find the $0°$C isotherm, it is necessary to linearly interpolate between the thermistor sensor that is lowest in the AL, where temperatures remain above freezing during the warm phase, and the sensor that is just below the AL where temperatures stay below freezing during the warm phase. The time series of the depths of the $0°$C isotherm is extracted using the contour plot function from the *matplotlib* Python library. Then, for every calendar year the maximum depth of the $0°$C isotherm is found. The uncertainty is defined as the difference between this maximum value and the depth value of the 95th percentile in the annual depth series of the $0°$C isotherm.

Another important permafrost variable that can be induced from borehole temperatures is the zero curtain (ZC). This is the period when the temperature in the AL remains constant at $0°$C due to the latent heat effects as the seasonal snow or ice melts (spring ZC) or freezes (autumn ZC). There is no established approach for deciding at which depth in the AL the temperature should be considered to extract the ZC. So, various depths within the AL are used to find ZC periods and assess which depth is the most appropriate. For the 1987 borehole the sensors in the AL are at 0.55 m, 1.55 m and 2.55 m. For the 2015 borehole the sensors in the AL are at 0.25 m, 0.5 m, 0.75 m, 1 m, 1.5 m, 2 m, 2.5 m and 3 m. However, the 1.5 m and 2.5 m sensors are not used as they stopped recording data on 2017-09-01 and 2018-06-01 respectively (Fig. 12). An algorithm is built to identify periods longer than two weeks for which the temperature is considered constant on the basis of two criteria. First, the temperature does not exceed a *period tolerance* defined by a change in temperature relative to the start of the period. The period tolerances are $0.04°$C or $0.01°$C for the 1987 and 2015 borehole data, respectively. Second, the temperature does not exceed a *step tolerance* defined by a change in temperature relative to the temperature of the previous day. The step tolerances are $0.02°$C or $0.01°$C for the 1987 and 2015 borehole data, respectively. The tolerance values were selected by inspecting the results of what was considered a reasonable ZC period (Fig. 14). The constant period is defined to end when either both tolerances are exceeded or just the period tolerance is exceeded. In the first case where both tolerances are exceeded, it means that the temperature has changed too much relative to the value at the start of the period and also changed too much from the previous day (Case 1 in Fig. 14). In the second case, the temperature has shifted away from the starting temperature but in a gradual way which never exceeded the step tolerance, but only the period tolerance (Case 2 in Fig. 14). The algorithm without the step tolerance often identified ZC periods that ended too early for cases when the temperature may be very gradually drifting out of the period tolerance but really it is still in a ZC phase, and should only end when the daily temperature difference is really substantial.

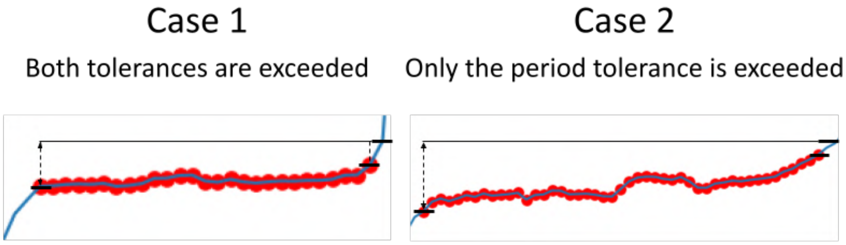

Figure 14: Visualization of the algorithm to extract the constant temperature periods for the zero curtains using a double tolerance approach.

### 3.1.5 Borehole deformation processing

The SAA inclinometer measures the inclination angle which is then converted into displacement in the *x*, *y* and *z* components (see 3.1.2). The main focus of rock glacier creep is horizontal deformation, so the SAA *z* component is neglected for this thesis. Each *x* and *y* point for each depth $Z$ in time is converted into a displacement scalar quantity $\delta_{x,Z}(t)$ and $\delta_{y,Z}(t)$ by subtracting the initial coordinates $x_o$ and $y_o$ measured on 2016-01-06.

$$\delta_{x,Z}(t) = x_Z(t) - x_{o,Z}$$

$$\delta_{y,Z}(t) = y_Z(t) - y_{o,Z}$$

Then the magnitude of the 2D deformation vector at a given depth and time is computed as follows:

$$\delta_{total,Z}(t) = \sqrt{\delta_{x,Z}(t)^2 + \delta_{y,Z}(t)^2}$$

Where $\delta_{total,Z}$ is the 2D horizontal deformation at time *t* and at depth $Z$ and $\delta_{x,Z}(t)$ and $\delta_{x,Z}(t)$ are the two scalar deformation values at time *t* for *x* and *y* respectively. This results in a cumulative deformation magnitude as the values of $\delta_{x,Z}(t)$ and $\delta_{x,Z}(t)$ are still relative to the initial position; this, however, for simplicity will be referred to as deformation. The temporal resolution is resampled from 6 hours to daily resolution and then smoothed using a 5-day moving window average. The monthly and yearly deformation are calculated by taking the last value of the month or year of $\delta_{total,Z}$. The first four months of measurements are unreliable as the instrumentation needs initialization time to stabilize, and so the useful start date of the inclinometer record is 2016-04-01. The last date with deformation data is 2023-09-15 before the rockfall event on Murtèl interrupted the measurements. Then, the deformation rate or creep velocity is calculated by differentiating the deformation time series across all temporal resolutions (daily, monthly, and yearly) for each depth $Z$.

$$v_Z(t) = \frac{d\delta_{total,Z}(t)}{dt} = \frac{\delta_{total,Z}(t_i) - \delta_{total,Z}(t_{i-1})}{\Delta t}$$

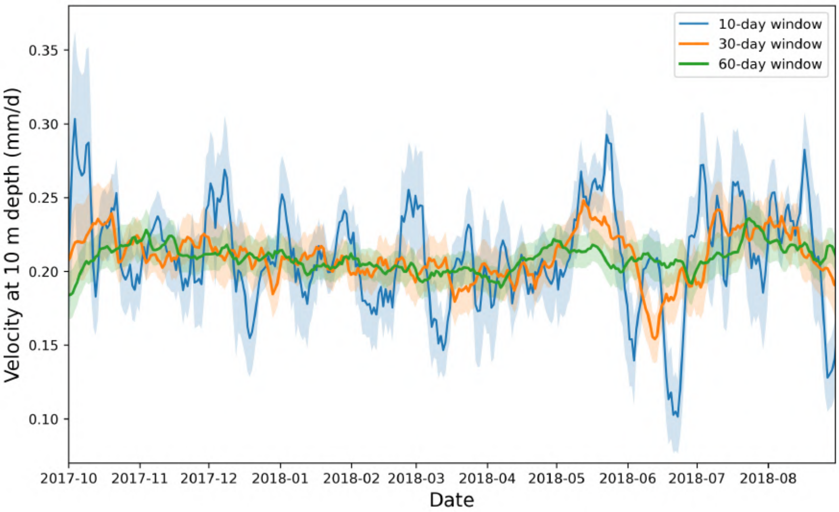

Figure 15: Example of sensitivity analysis for moving window size to remove noise from velocity data at 10 m depth for the 2017 hydrological year.

For a daily temporal resolution, the deformation rate required further smoothing. A 10, 30 and 60-day moving window was considered to remove noise and of those the 30-day moving window was considered the most suitable to maintain a sufficient signal-to-noise ratio (Fig. 15). The monthly and yearly deformation rates are calculated by differentiating the monthly and yearly deformation values respectively. The strain rate $\dot{\varepsilon}$ is a useful variable to assess how the deformation rate changes with depth. It is defined as the rate of change of the creep velocity with depth.

$$\dot{\varepsilon}(t) = \frac{dv(t)}{dz} = \frac{v_Z(t) - v_{Z-1}(t)}{z_Z - z_{Z-1}}$$

The velocity at depth $Z$ is subtracted by the velocity of the sensor above it at depth $Z - 1$. The denominator $z_Z - z_{Z-1}$ is always equal to 50 cm, which is the space between each segment joint of the inclinometer. The strain rate is calculated from the monthly creep velocity data as the daily velocity has too much noise even after taking the 30-day moving window average. The strain rate is especially useful for identifying the depth ranges of the shear zone where the highest strain rates are found. This is done using the annual strain rates and calculating an annual mean strain rate profile with depth. The depth range of the shear zone is then visually extracted from the top and bottom of the main peak in the strain rate in the annual mean vertical profile. With all the depth ranges of the three identified layers: AL, ice-rich core and shear zone; it is now possible to compute layer-specific deformation rates. This is done for all timescales: daily, monthly, and yearly.

$$v_{AL}(t) = v_{0m}(t) - v_{3.5m}(t)$$

$$v_{core}(t) = v_{3.5m}(t) - v_{25m}(t)$$

$$v_{shearzone}(t) = v_{25m}(t) - v_{29m}(t)$$

An ALT of 3.5 m is used as this is the mean ALT for most years and changing this to 4 m or 4.5 m makes negligible difference on the $v_{AL}(t)$ results. The shear zone depth range is taken to be 0.5 - 1 m outside the depth bounds of the shear zone to ensure that all shear zone deformation is accounted for. The fraction of total surface deformation that each layer contributes to is calculated as follows:

$$\%\delta_{total,AL}(t) = \frac{\delta_{total,0m}(t) - \delta_{total,3.5m}(t)}{\delta_{total,0m}(t)} \times 100$$

$$\%\delta_{total,core}(t) = \frac{\delta_{total,3.5m}(t) - \delta_{total,25m}(t)}{\delta_{total,0m}(t)} \times 100$$

$$\%\delta_{total,shearzone}(t) = \frac{\delta_{total,25m}(t) - \delta_{total,29m}(t)}{\delta_{total,0m}(t)} \times 100$$

The deformation $\delta_{total}(t)$ is used to compute the percentage of annual total surface deformation happening at each layer. This provides useful information on how the deformation is vertically distributed in Murtèl rock glacier.

## 3.2 GNSS

A few meters next to the 2015 borehole a GNSS (Global Navigation Satellite System) station was built on a large surface boulder (Fig. 9). The large boulder was chosen in the hope that it is connected to the movement of the nearby blocks. The GPS sensor system measures surface displacement and inclination at 30-second intervals (Cicoira et al., 2022). The station consists of a GPS Trimble Bullet III antenna, a DAQ system containing a data logger, transmission system, and a two-axis inclinometer (Fig. 16). The GNSS receiver used is a *u-blox LEA-6T* (Cicoira et al., 2022). The power supply comes from a 30 W solar panel mounted on a fiberglass mast and a 12 V backup battery also placed on the boulder (Cicoira et al., 2022). The GPS measurements are stored using a double difference GNSS post-processing method based on a reference stable GPS station taken from the national reference network located within the Engadin region. The reference station used is located at a similar altitude and is surrounded by similar topography (Cicoira et al., 2022). The GNSS surface displacement data begin on 2016-07-15 and end on 2023-08-27, also before the 2023 rockfall. The GPS antenna measures East and North coordinates which are first processed by Jan Beutel to remove noise using a LOWESS function following the procedure from PermaSense data management. Then, the smoothed *x* and *y* coordinates are translated into 2D displacement, similar to the steps taken for the SAA data (Section 3.1.5). The resulting cumulative horizontal surface displacement is differentiated to obtain a deformation rate or surface velocity, as was done for the SAA data.

Figure 16: GPS sensor system components used for the GNSS station at Murtèl rock glacier. Adopted from Cicoira et al., 2022.

## 3.3 Geodetic measurements

Since 2009, PERMOS has conducted geodetic surveys every August at Murtèl rock glacier to measure surface displacement at 11 different locations. During a survey, a Leica FlexLine theodolite device is placed in a fixed position on a nearby stable ridge with a good view on the rock glacier. At another location along the ridge, a fixed reference marker is placed and its distance from the station is measured to establish a stable position. One person visits all the marked locations on the rock glacier and places a reflector for the theodolite station to measure its distance. Using the fixed positions of the theodolite station and the reference marker on the ridge, the coordinates of the markers on the rock glacier can be calculated via triangulation. Then, the difference in the position of the coordinates from one year to the next is used to calculate the annual velocity of each marker. The geodetic surface displacement measured annually using the theodolite station is used for the target years of 2016-2023. Of the 11 points with data available, only one of them (COR_021) is a few meters away from the boreholes and the GNSS station. So, the geodetic horizontal surface deformation is derived from this one point also using similar processing steps as for the SAA and GNSS data where the coordinates are compared to compute relative 2D displacement vectors for each year.

## 3.4 Meteorological station

The *in-situ* PERMOS weather station was installed at Murtèl rock glacier in January 1997 at around 2700 m altitude and 5 m away from the 1987 borehole (Fig. 9) (Scherler et al., 2014). The station measures air temperature, surface temperature, relative humidity, wind speed, incoming and outgoing short-wave and long-wave radiation, and snow height (see Table 1). The sampling rate is 15 seconds, after which 30 minute averages are taken and the data is transmitted remotely via GSM cellphone network. From 2019-03-31 to 2019-10-01 there is a major data gap when data transmission was interrupted. The handling of this data gap is outlined in Section 3.4.1. The PERMA-XT project also built a micrometeorology station in August 2020 near the PERMOS weather station. The only measurement from the PERMA-XT station used in this thesis is the rainfall. The rainfall data from the PERMA-XT is used in combination with the Piz Corvatsch MeteoSwiss rainfall to generate a complete *in-situ* record of rainfall from 1997 to 2023 (see Section 3.4.1).

Table 1: List of relevant weather variables and the corresponding sensors and accuracy. Adopted from Scherler et al. (2014).

| **Variable** | **Sensor** | **Sensor type** | **Accuracy** |
|---|---|---|---|
| Air temperature / humidity | MP-100A ventilated hygrometer (Rotronic) | RTD Pt-100; C94 hygrometers | $\pm 10\%$ |
| Snow height | SR50 (Campbell) | Ultrasonic electrostatic transducer | $\pm 0.01$ m |
| Surface temperature | Infrared thermometer | Irt/c.5 | $\pm 1.5\,°\mathrm{C}$ |
| Borehole temperature | YSI 44006 (Yellow Springs Instruments) | NTC thermistors | $\pm 0.02\,°\mathrm{C}$ |
| Precipitation | MeteoSwiss (Piz Corvatsch summit) | Rain gauge | $\pm 30\%$ |

### 3.4.1 Weather data processing

The relevant meteorological variables considered are air temperature, surface temperature, rainfall, and snow height. The air, surface temperature, and snow height are available with an hourly temporal resolution from the *in-situ* PERMOS weather station at Murtèl rock glacier. The hourly data are then resampled by computing daily averages from 1997 to 2023. The weather station stopped recording data from 2019-04-01 to 2019-09-30. Data filling was only possible for air temperature based on the values measured at the Piz Corvatsch MeteoSwis station. The regression coefficient between the daily *in-situ* PERMOS air temperature and the Piz Corvatsch air temperature was 0.98. The regression equation was used to calculate the daily air temperature at the *in-situ* PERMOS weather station using the Piz Corvatsch air temperature as input. The complete air temperature series was then smoothened using a 10 day moving window average. The smoothing function for a given value at time $t_i$ takes the average between the values ranging from times $t_{i-n/2}$ to $t_{i+n/2}$ where $n$ is the size of the moving window.

The Piz Corvatsch weather station is also used to extend the rainfall measurements backward in time at the short-term *in-situ* PERMA-XT station which only lasted from 2020-08-22 to 2023-12-24. A regression correlation is built between the two daily rainfall measurements within this period. The unheated PERMA-XT rain gauge does not measure snowfall during the cold phase, so the regression only uses the warm phase rainfall data for both the PERMA-XT station and the Piz Corvatsch station. The regression coefficient between the warm phase PERMA-XT and Piz

Corvatsch rainfall is 0.88. The *in-situ* daily rainfall from 1997 to 2023 was calculated using the regression equation and the Piz Corvatsch warm-phase rainfall as input. Given that the regression is built using only the warm phase data, the output for the cold phase *in-situ* precipitation is likely to be less reliable, however, this is only used to compute annual sums of precipitation, so high accuracy at a daily timescale is not required during the cold phase. This continuous long-term record of *in-situ* rainfall is used to extract the number of dry periods in a given warm phase. This is done by finding periods of at least 5 consecutive days where the *in-situ*-derived precipitation is below 0.3 mm. The reason for this elevated threshold is that after the conversion done using the regression coefficients, the nonzero intercept lifted the 0 mm to approximately 0.26 mm.

There are a variety of snow variables that are relevant for rock glacier dynamics. First, the large data gap from 2019-03-31 to 2019-10-01 needs to be filled. The mean daily snow height for these missing dates is found using these daily mean values for the according missing dates from the other years. Now all the relevant snow variables can be extracted using the continuous snow record. For each year, the snow onset date is extracted by finding the date that first measures a snow height above measurement error (0.05 m) and stays above this threshold for at least two weeks. Then, Amschwand et al. (2023) found that when the snow height exceeds 0.7 m, and there is a continuous snow cover over the rock glacier, the permafrost thermal regime becomes decoupled from atmospheric conditions. The onset of an insulating snow cover is found by extracting the date when the snow height first exceeds 0.7 m. The duration of the presence of an insulating snow cover is also calculated until the snow height drops below 0.7 m as it starts to melt. The mean snow height in the early winter is calculated by taking the average of daily snow heights from November to January for each hydrological year. The late spring mean snow height is calculated from the daily snow heights from April to June.

The seasonal melt period is important in dictating the meltwater supply, the timing of the seasonal creep response, and the transition from the cold to the warm phase. The start of the snow-free period is calculated as the first date when the snow height remains below the measurement error of 0.05 m for at least two weeks. During the snow melt period, the melt energy is calculated based on the decrease in the measured snow height (Scherler et al., 2014). Snow is assumed to melt only on days when the measured air temperature is above $-3°$C. The snow height time series is smoothed using a 10-day moving window average and then differentiated with time to get a daily difference in snow height. Only negative differences are kept, and positive differences are set to zero. The snow melt energy (W/m$^2$) is computed as follows:

$$Q_m = \frac{\Delta h \rho_s L_f}{\Delta t}$$

Where $\Delta h$ is the daily decrease in snow height for days when the air temperature is above $-3°$C, $\rho_s$ is the snow density taken to be 300 kg/m$^3$, $L_f$ is the specific latent heat of fusion of water

($334 \times 10^3$ J/kg) and $\Delta t$ is the number of seconds in a day (Scherler et al., 2014). This definition does not account for any refreezing of snow melt water and is thus likely to overestimate the snow melt energy.

## 3.5 Process-based phases

As this thesis considers short seasonal timescales, it is useful to define two distinct physically based phases (Schneider et al., 2012). The two defined phases are the cold and warm phase. The temporal bounds of these phases have flexible dates based on the seasonality of the given year. The start of the warm phase and the end of the cold phase are defined by the beginning of the snow-free period. Namely, the date before the first two week period in the year that has no snow cover. For this, the snow height data measured at the on-site PERMOS weather station is used. The end of the warm phase and the start of the cold phase is defined as the date when the temperature measured at 0.5 m depth in the borehole drops below $0°$C. The two phases are defined as such to account for the seasonal acceleration of rock glacier creep that begins after the snow melt period has ended. If the date for the start of the snow-free period or the first freezing date of surface borehole temperatures is missing for a given year, then these are set to their respective mean dates which are June 15 and October 19 respectively. The phase definitions are then used to summarize phase-specific driving variables, such as meteorological, borehole temperatures, ground heat flux to relate to the deformation.

The start of the hydrological year is varied to start on September 1 instead of the usual October 1. Murtèl rock glacier typically reaches its peak deformation in mid-September. So, by setting the start of the hydrological year to September 1 it ensures that the measured seasonal acceleration belongs to a hydrological year that is the same as the calendar year. For example, a peak in deformation measured in mid-September 2022 should belong to the hydrological year of 2022 and not 2021 which would happen if the October 1st start date would be used.

## 3.6 Statistical analysis

For a variety of variables the daily data was used to compute the annual mean, annual maximum, and minimum, and the dates when the maximum and minimum occurred. This was done for variables such as: air and surface temperature, borehole temperatures, snowmelt energy, ground heat flux, GNSS deformation rate, and SAA deformation rate. Annual statistics are only stored if for the given year there are at least 360 days with available data. So, for example, for the 2023 for the air temperature the data ends on September 19, therefore the annual statistics were not extracted. For precipitation variables, such as snow height and rainfall, instead of an annual mean, the sum was taken. The mean or sum of all of these variables were also taken individually for the cold and warm phases of each year. The standard error of the mean (SEM) is used as the uncertainty of the means. These descriptive statistics will be used to assess the controls of rock glacier deformation on an annual timescale.

The long-term trends in climate are summarized using the linear regression equation and the corresponding confidence intervals. The change in a meteorological variable over a given period is calculated by taking the difference between the final and initial values of the regression line. The uncertainty of the initial and final values of the regression line is taken as half the width of the 95% confidence interval. Then, the uncertainty in the change magnitude over the period is taken as the addition of the uncertainty of the initial and final values. Linear correlation analysis was performed to analyze how different annual variables related to each other. The reported results are the correlation of determination $R^2$ and the p-value. The $R^2$ shows how much of the variance of the response variable is explained by the independent variable. The correlation is considered statistically significant when the p-value $< 0.05$. Multiple regression (MLR) models will be trained on the relationship between the driving variables: air temperature, surface temperature, mean AL temperature, and $Q_G$ at 3.5 m and the response variables of SAA and GNSS surface deformation rates at a monthly resolution. 80% of the data is used for training and 20% to test and validate the model results. To evaluate the results of the MLR models the ratio between the mean square regression (MSR) and mean square error (MSE), known as the F-statistic, is used in combination with its corresponding p-value. So, a large F-statistic and a p-value less than 0.05 mean that at least one of the driving variables contributes significantly to the model. The coefficients for each driving variable in the MLR equation are used to evaluate the relative contribution of each variable.

# 4 Results

## 4.1 Long term climate trends

This first section of the results will explore long-term temporal trends in both atmospheric conditions and borehole temperatures measured since 1997 from the 1987 borehole at Murtèl rock glacier. The first part will focus on the climate, including air temperature, surface temperature, and precipitation. Then patterns in annual borehole temperatures at important permafrost depths will be analyzed and compared to climate. Lastly, using the 1987 borehole temperature data, long-term trends in AL thickness and zero curtain (ZC) trends will be explored.

### 4.1.1 Air and surface temperature

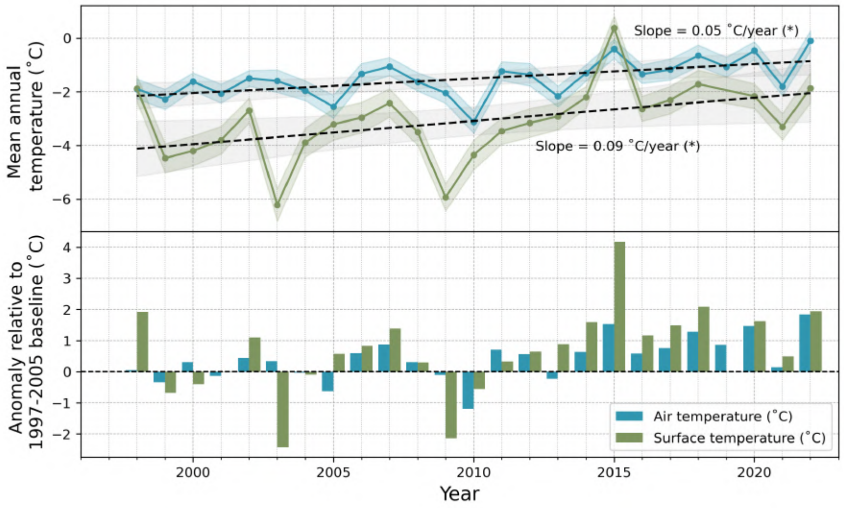

Figure 17: Long term trends in mean annual air and surface temperature measured at the PERMOS weather station using data from 1997 to 2022. The (*) next to the slope means that the linear regression is statistically significant. Data source: PERMOS.

From 1997 to 2022 there is a significant increasing trend in both air and surface temperature (Fig. 17). The mean annual air and surface temperatures are increasing by $0.05$°C and $0.09$°C per year, respectively. The general warming trend in atmospheric conditions is also illustrated by the more positive annual air and surface temperature anomalies after 2010. The surface temperature is generally $1-2$°C cooler than the air temperature. For most years, the interannual trends in air and surface temperature are in sync and the annual anomalies are similar in magnitude and direction. For years 2003 and 2009 the surface temperature is much lower than the air temperature. The year 2015 had the highest surface temperature for this station's record and is the only year when the annual surface temperature is higher than the annual air temperature. The year 2022 was the warmest in terms of air temperature in the record. The MAAT has increased from $-2°$C in 1997 to $-0.9°$C in 2022 (Table 2).

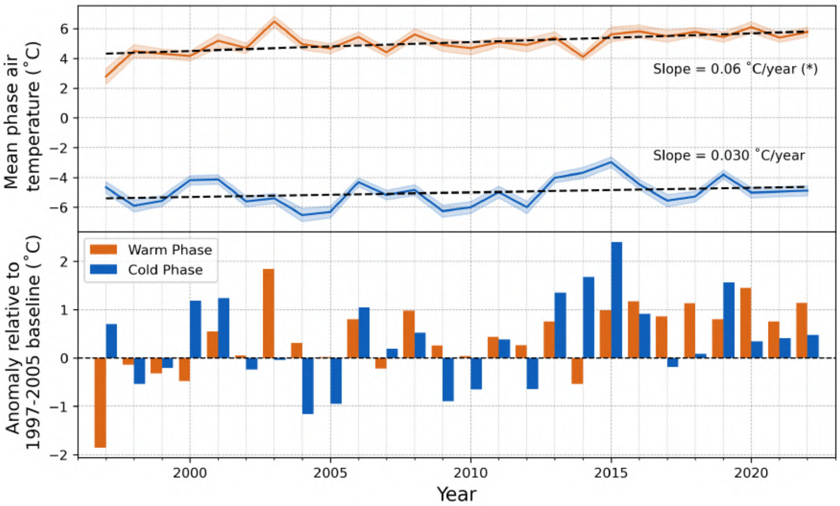

Figure 18: Long term trends in mean air temperature for the warm and cold phase separately. Temperature is measured at the PERMOS weather station using data from 1997 to 2023. The (*) next to the slope means that the linear regression is statistically significant. Data source: PERMOS.

The mean air temperature in the warm phase is typically approximately $10°$C warmer than during the cold phase. The warm phase mean air temperature is steadily increasing at a rate of $0.06°$C per year, while the cold phase mean air temperature shows no significant trend. The warm phase of year 2003 had especially high temperatures, while the cold phase temperature reaches its peaks in 2000, 2001, 2006, 2015 and 2019; with 2015 having the warmest cold phase on record. The switch to constant positive temperature anomalies for both phases is seen a bit later in 2014 instead of 2010 as for the MAAT anomalies (Fig. 18).

Table 2: Trends of temporal linear regressions of atmospheric conditions measured at the PERMOS weather station on Murtèl rock glacier. The (*) means significant regression (p-value < 0.05). Uncertainty extracted from width of 95% CIs. Data source: PERMOS.

| | **Temperature 1997 (°C)** | **Temperature 2022 (°C)** | **Change (°C)** |
|---|---|---|---|
| **Annual air (*)** | $-2.0\ (\pm 0.5)$ | $-0.9\ (\pm 0.6)$ | $1.1\ (\pm 1.1)$ |
| **Annual surface** | $-3.6\ (\pm 1.2)$ | $-2.3\ (\pm 1.2)$ | $1.3\ (\pm 2.4)$ |
| **Warm phase air (*)** | $4.3\ (\pm 0.5)$ | $5.9\ (\pm 0.6)$ | $1.5\ (\pm 1.1)$ |
| **Cold phase air** | $-5.4\ (\pm 0.7)$ | $-4.6\ (\pm 0.7)$ | $0.8\ (\pm 1.4)$ |

### 4.1.2 Precipitation

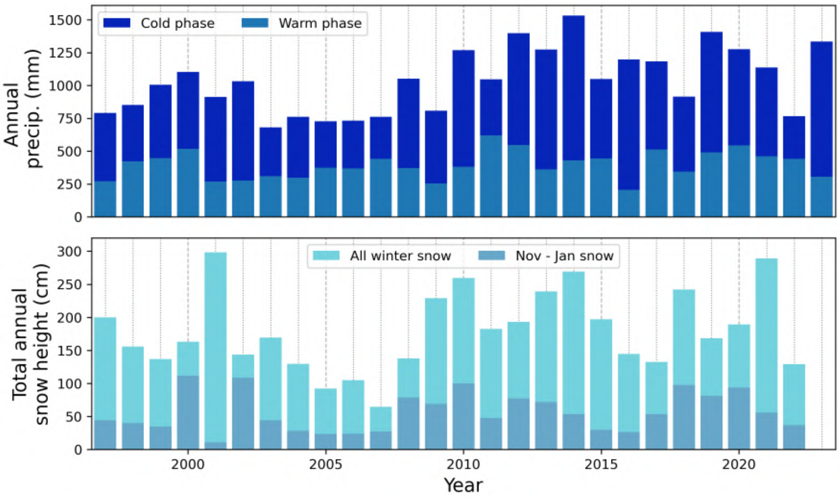

Figure 19: Annual cold and warm phase precipitation sums extrapolated using the combination of PERMA-XT and Piz Corvatsch data (top), and annual sum of snow height measured at on-site weather station (bottom). Data source: PERMOS and MeteoSwiss.

There is no significant long-term trend in the annual precipitation data at Murtèl rock glacier (Fig. 19). The mean annual precipitation measured during the entire period at Murtèl rock glacier is 1015 mm (Table 3). There is a drier period from 2003 to 2008 followed by an increase in precipitation from 2012 to 2014. The total annual mean snow height is 183 cm (Table 4). The inter-annual variability in snow height is much greater than that of total precipitation. The total winter snow accumulation is not necessarily representative of the early winter snow accumulation (Fig. 19). For example, the early winter snow accumulation was similar between winters of 2018-19 to 2020-21, but the winter of 2020-21 as a whole received significantly more snow compared to 2018-19 and 2019-20. In the more recent years, the winters of 2016-17, 2021-22 and 2022-23 were relatively snow-poor. After the winter of 2000-01, the 2020-21 winter was the second snowiest in the entire measurement period.

Table 3: Annual precipitation statistics from the extrapolated data at the PERMA-XT station using the Piz Corvatsch data. Uncertainty taken from SEM. Data source: PERMOS and MeteoSwiss.

| | **Precipitation (mm)** | **Year(s)** |
|---|---|---|
| **Annual mean** | 1015 ($\pm$44) | 1994–2023 |
| **Annual minimum** | 680 | 2003 |
| **Annual maximum** | 1533 | 2014 |

Table 4: Annual snow statistics from the snow height measurements at the PERMOS weather station on Murtèl rock glacier from 1997 to 2022. Data source: PERMOS.

| | **Snow height (cm)** | **Year(s)** |
|---|---|---|
| **Annual sum mean** | 183 (±13) | 1997–2022 |
| **Annual sum minimum** | 64 | 2007 |
| **Annual sum maximum** | 307 | 2001 |

## 4.2 Long term permafrost temperature trends

The previous section showed how atmospheric temperatures have been steadily warming, especially during the warm phase. Now, using the long-term borehole temperature record from the 1987 borehole, the permafrost temperature trends can be analyzed. Figure 20 shows a consistent increase in the warm phase maximum temperatures measured in the top 4.5 m of the borehole. At these depths, the cold phase temperature has much greater inter-annual variability. At depths from 9.5 to 21.5 m the trend is less clear. From 2008 to 2016 the temperature at deeper depths is increasing steadily followed by a strong cooling period until 2019 when warming resumes. At these depths, the cold phase temperatures follow the warm phase temperatures more closely.

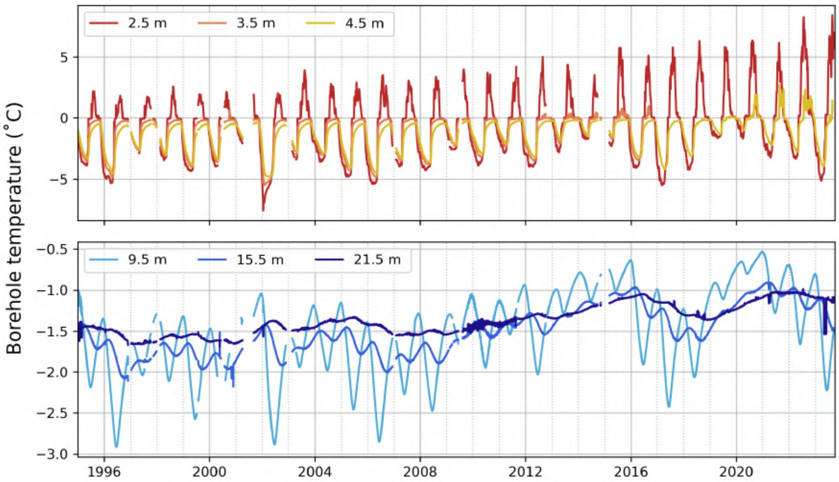

Figure 20: Complete time series of daily temperatures measured in the 1987 borehole on Murtèl rock glacier for depths with close to continuous measurements. Data source: PERMOS.

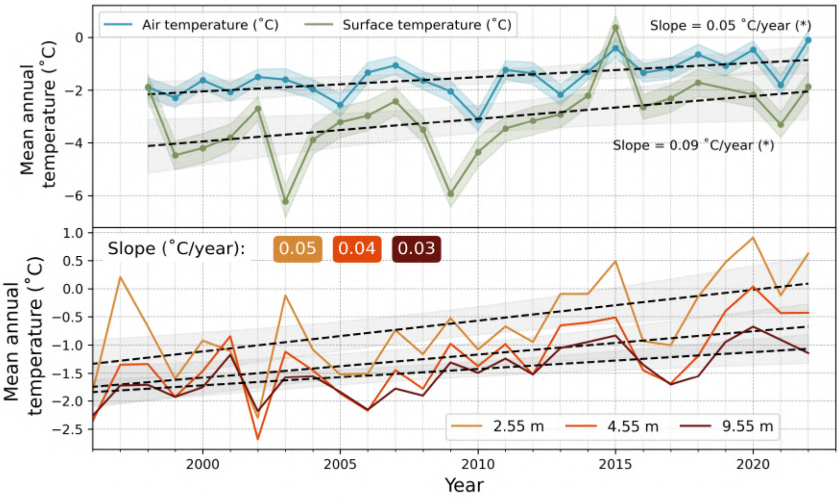

Figure 21: Long term time series of MAAT and MAST with linear regression lines (top); mean annual temperature at 2.55 m, 4.55 m, 9.55 m in the 1987 borehole at Murtèl rock glacier with corresponding linear regression lines and slopes (bottom). Data source: PERMOS.

To allow for a better comparison between the atmospheric conditions and the permafrost conditions, an annual temporal resolution is now used. Figure 21 shows that the thermistor at 2.55 m is warming at the same rate of $0.05°$C as the air temperature. The yearly warming rate of borehole temperatures then decreases with depth. The especially cold years at the surface of 2003 and 2009 are actually relatively warm years in the borehole. However, the 2015 heatwave can also be observed in the borehole temperatures. The warmest year for borehole temperatures was 2020. The temperatures at depths from 2.5 to 9.5 m are well synchronized. Linear correlation analysis shows that the regression between MAAT and mean annual borehole temperature is strongest at shallow depths but also at depths approaching the depth of zero annual amplitude (Fig. 24). Whereas, in the higher part of the ice-rich core from 4.5 to 12.5 m the correlation between MAAT and borehole temperatures is not significant.

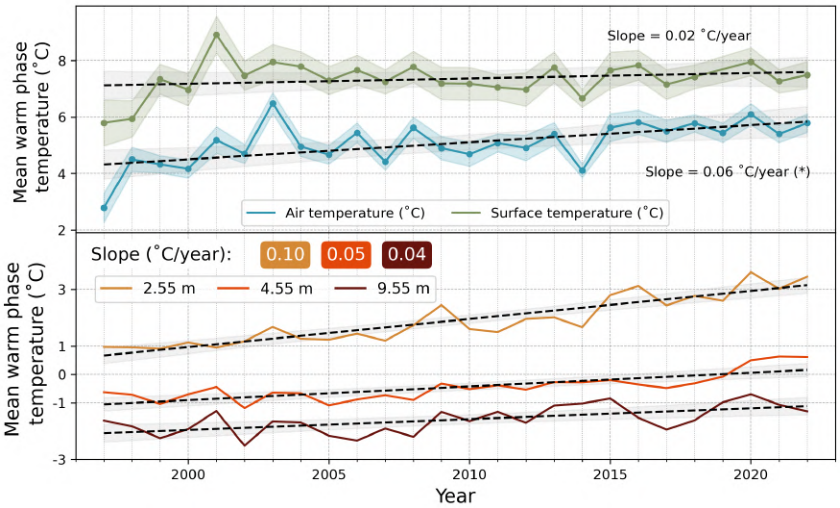

Figure 22: Long term time series of mean warm phase air and surface temperature with linear regression lines (top); mean warm phase temperature at 2.55 m, 4.55 m, 9.55 m in the 1987 borehole at Murtèl rock glacier with corresponding linear regression lines and slopes (bottom). Data source: PERMOS.

The same time series analysis as before can also be performed for the warm and cold phases separately by using the corresponding phase-specific annual averages. The warm phase borehole temperature at 2.55 m is increasing at a substantially faster rate (0.10°C/year) than the surface temperature (0.02°C/year) (Fig. 22). The surface temperature is always a few degrees higher than the air temperature during the warm phase. The warm phase mean borehole temperature at 2.55 m is also always above freezing. Whereas, the 4.55 m warm phase mean temperature is below freezing until 2019 after which it exceeds 0°C. The especially warm summer of 2001 seen in the surface temperature signal is only observed at 4.55 and 9.55 m, but not at 2.55 m in the borehole. The cold summer in 2014 is only reflected at 2.55 m, while this cannot be observed deeper in the rock glacier. The air temperature of the warm phase has a significant correlation with the warm phase borehole temperatures at depths: 1.55 to 7.55 m and 15.57 to 21.56 m (Fig. 24). This is a similar pattern seen at the annual timescale where the correlations are significant only for the shallow or deep thermistors. For the cold phase, there are no significant temporal trends in either the air or the surface temperature (Fig. 23). The temporal trends in the three shown borehole cold phase temperatures are also weak with warming rates of at most 0.04°C/year for the 4.55 m thermistor. The periodicity of the periods with high and low cold phase temperature do not align between the atmosphere and below ground in the borehole. There is no significant correlation between the mean cold phase air temperature and the cold phase borehole temperatures from 1.55 m to 8.55 m (Fig. 24). However, for thermistors from 9.55 m to 16.57 m there is a significant positive correlation with the mean cold phase air temperature.

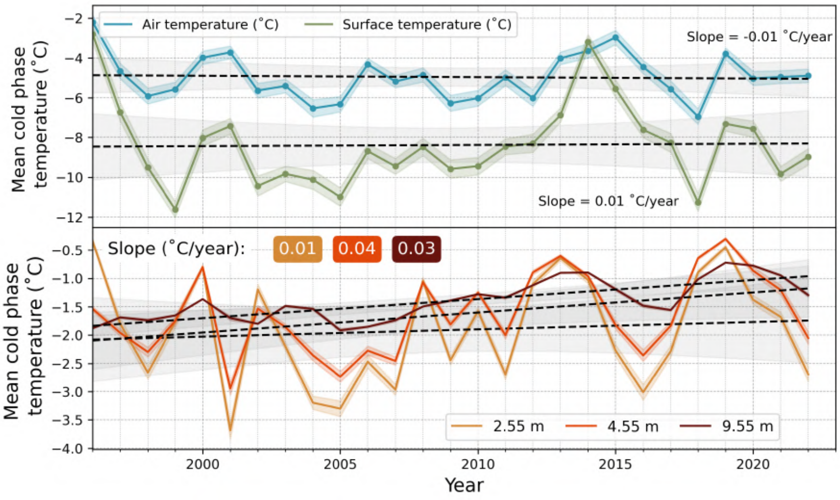

Figure 23: Long term time series of mean cold phase air and surface temperature with linear regression lines (top); mean cold phase temperature at 2.55 m, 4.55 m, 9.55 m in the 1987 borehole at Murtèl rock glacier with corresponding linear regression lines and slopes (bottom). Data source: PERMOS.

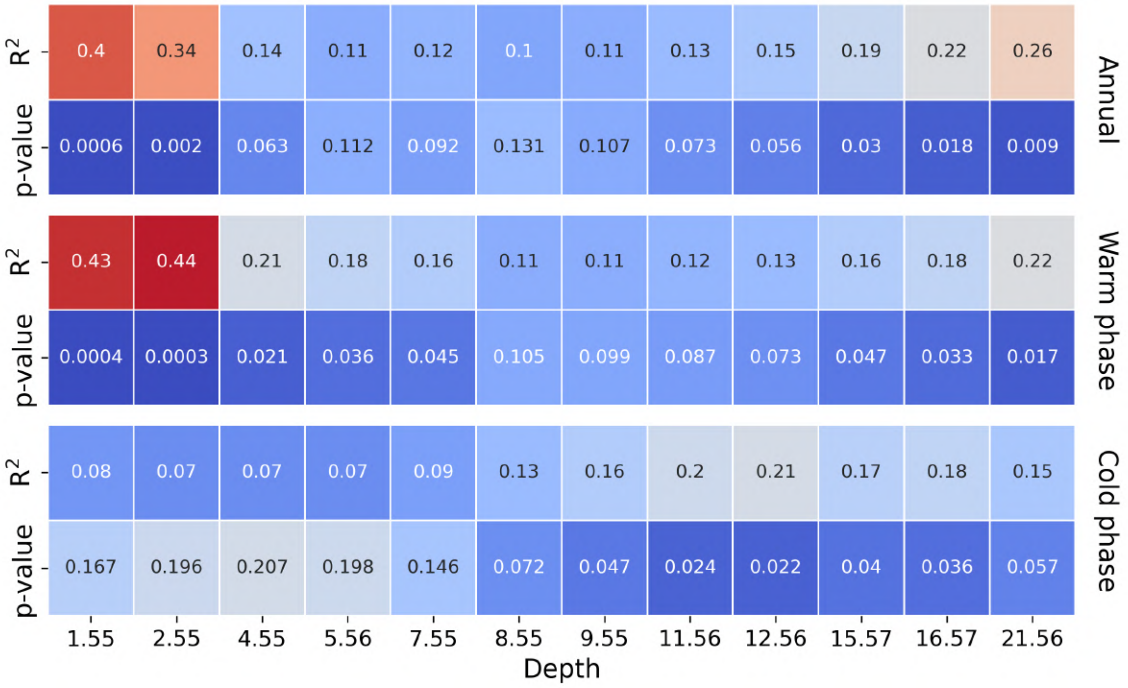

| | | 1.55 | 2.55 | 4.55 | 5.56 | 7.55 | 8.55 | 9.55 | 11.56 | 12.56 | 15.57 | 16.57 | 21.56 |
|---|---|---|---|---|---|---|---|---|---|---|---|---|---|
| Annual | $R^2$ | 0.4 | 0.34 | 0.14 | 0.11 | 0.12 | 0.1 | 0.11 | 0.13 | 0.15 | 0.19 | 0.22 | 0.26 |
| | p-value | 0.0006 | 0.002 | 0.063 | 0.112 | 0.092 | 0.131 | 0.107 | 0.073 | 0.056 | 0.03 | 0.018 | 0.009 |
| Warm phase | $R^2$ | 0.43 | 0.44 | 0.21 | 0.18 | 0.16 | 0.11 | 0.11 | 0.12 | 0.13 | 0.16 | 0.18 | 0.22 |
| | p-value | 0.0004 | 0.0003 | 0.021 | 0.036 | 0.045 | 0.105 | 0.099 | 0.087 | 0.073 | 0.047 | 0.033 | 0.017 |
| Cold phase | $R^2$ | 0.08 | 0.07 | 0.07 | 0.07 | 0.09 | 0.13 | 0.16 | 0.2 | 0.21 | 0.17 | 0.18 | 0.15 |
| | p-value | 0.167 | 0.196 | 0.207 | 0.198 | 0.146 | 0.072 | 0.047 | 0.024 | 0.022 | 0.04 | 0.036 | 0.057 |

Figure 24: Linear correlation analysis results between the mean air temperature and mean borehole temperatures at various timescales (annual, warm and cold phase) at depths with continuous records from 1998 to 2022 in the 1987 borehole at Murtèl rock glacier. Data source: PERMOS.

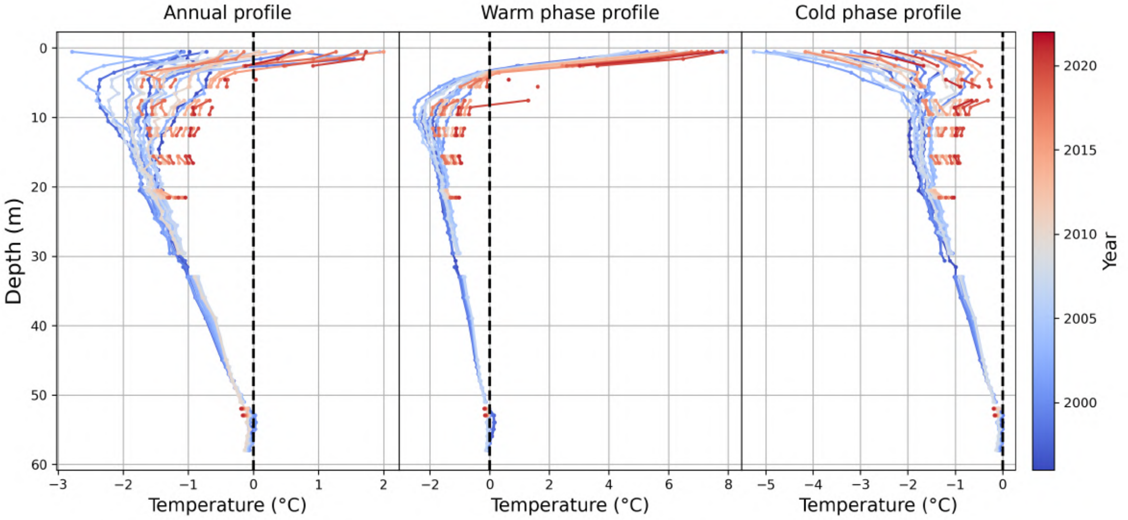

Figure 25: Temperature profiles with depth computed using annual, warm and cold phase mean temperatures from 1994 - 2022 data of 1987 borehole at Murtèl rock glacier. Data source: PERMOS.

The almost 30 year record of borehole temperatures from the 1987 Murtèl borehole can be plotted with depth to visualize long-term changes in borehole temperatures at all depths (Fig. 25). At the annual timescale the top of the borehole temperatures range from close to -3°C to 2°C. Across the three timescales, there is a general warming trend across the top around 20 m of the borehole. There is a total temperature increase of about 1.5°C at 10 m, 1°C at 15 m, and 0.5°C at 20 m over the 28 years of data. At a very approximate level this gives the same order of magnitude of yearly warming rates in borehole temperatures as seen in Fig. 21. For the warm phase mean temperature profile, the warming is even more pronounced in the AL where temperatures increased from 4.5°C to 8°C. In the cold phase profile the AL warming is not as evident, however, the depths ranging from 10 m to 20 m still experience warming of about 1°C. The top of the borehole cold phase mean temperatures range from below -5°C to -0.5°C. Near the bottom of the borehole at around 53 m to 58 m a talik can be observed where temperatures are slightly above 0°C. The presence of this talik increases during the warm phase and decreases during the cold phase.

### 4.2.1 Long term trends in ALT

The ALT describes how deep the top layer of the rock glacier thaws during the summer. The average ALT of Murtèl rock glacier is 3.6 m (±0.1 m) and 3.5 m (±0.1 m) measured in the 1987 and 2015 boreholes respectively. In the 1987 borehole the ALT is very stable at about 3.5 m from 1987 to 2010 and then increases from 2010 to 2015 by about 0.8 m to values around 4.3 m (Fig. 26). For the two overlapping years of 2016 and 2017, the 1987 borehole ALT is about 1 m deeper than the ALT from the 2015 borehole. In the 2015 borehole the ALT is stable at around 3.5 m for six years and then increases from 2021 to 2024 by 0.6 - 0.9 m. The ALT reported by the PERMOS team is also illustrated in Figure 26. The ALT extracted by PERMOS shows very similar patterns as to that calculated in this thesis.

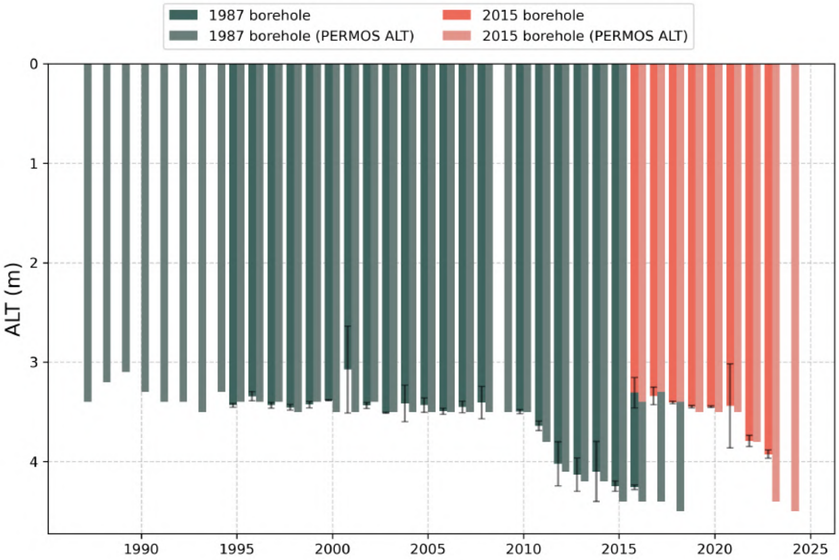

Figure 26: Annual active layer thickness (ALT) of Murtèl rock glacier from the two boreholes. The values extracted from PERMOS are also illustrated for comparison. Data source: PERMOS.

### 4.2.2 Long term trends in seasonal phases

The mean duration of the warm and cold phases is 125 and 239 days, respectively. The start of the warm phase is defined by the disappearance of the snow cover, and this happens on average on June 15 at Murtèl rock glacier. The start of the cold phase is defined by the temperature near the top of the borehole dropping below the freezing point, and this happens on average on October 19. There is no clear general trend in the duration of the cold or warm phase (Fig. 27). However, for the most recent period from 2016 to 2022, the warm phase begins earlier each year. The years of 2007, 2011 and 2022 have the longest warm phases observed, while the years 2001, 2008 and 2015 have the longest cold phases. The start of the cold phase is gradually more delayed from the 2000 to 2022.

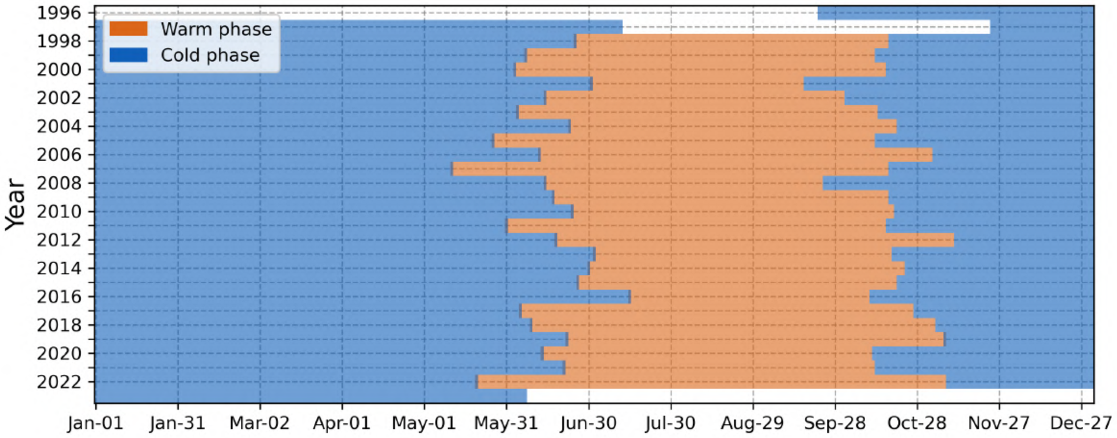

Figure 27: Temporal extent of warm and cold phase duration for each year based on the PERMOS weather station and 1987 borehole on Murtèl rock glacier. Data source: PERMOS.

### 4.2.3 Long term trends in zero curtains

The zero curtain period is found either in the spring when the seasonal ground ice and snow in the AL are melting or in the autumn when the water in the AL freezes. The spring ZC (SZC) starts on average in late May and lasts about a month until end of June or the beginning of July (Table 5). There are some exceptions with the SZC starting as early as the beginning of May (2019) and ending as late as the beginning of August (2009). The autumn ZC (AZC) on average starts in the end of October and also lasts about a month until the end of November. In some cases the AZC can start as early as the end of September (1996) and end as late as the end of December (2013). The extraction of the ZC periods is carried out for both the 1987 and 2015 borehole temperature data and this allows to compare how the ZCs have changed over time. Figure 28 shows that both SZC and AZC start earlier as measured from the 1987 borehole data compared to the 2015 borehole data (p-value = 0.06, 0.07 respectively). There are no differences when it comes to the end of either ZC period between the two boreholes.

Table 5: Average, minimum and maximum duration, start and end to the spring zero curtain (SZC) and the autumn zero curtain (AZC) based on data from the 1987 borehole on Murtèl rock glacier. Data source: PERMOS.

| | Mean | Min. (year) | Max. (year) |
|---|---|---|---|
| **SZC duration** | 33 | 16 (1997) | 74 (2009) |
| **SZC start** | 05-29 | 05-03 (2019) | 06-22 (2013) |
| **SZC end** | 07-01 | 05-21 (2019) | 08-11 (2009) |
| **AZC duration** | 33 | 15 (2022) | 64 (1996) |
| **AZC start** | 10-24 | 09-21 (1996) | 11-21 (2019) |
| **AZC end** | 11-26 | 11-05 (2003) | 12-28 (2013) |

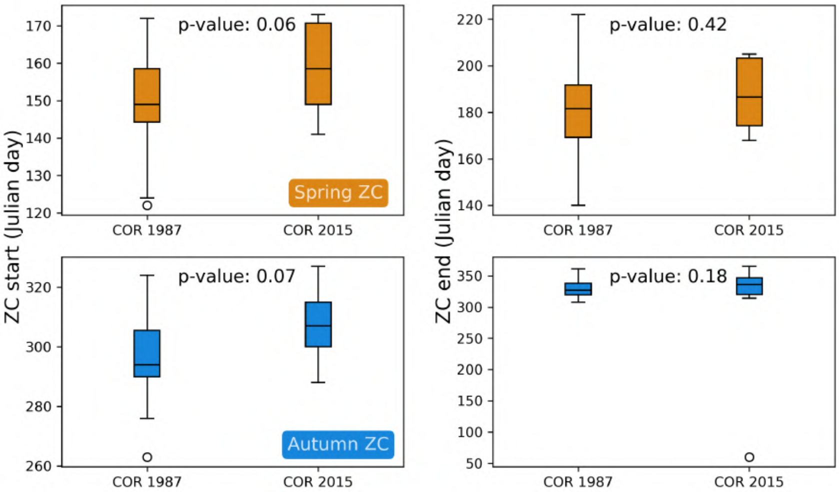

Figure 28: Comparison of distribution of spring (top) and autumn (bottom) ZC start and end dates between the 1987 and 2015 borehole data on Murtèl rock glacier. The p-values are computed using an independent two-sample t-test. Data source: PERMOS.

As there is no depth to measure temperature that is optimized to extract ZC periods, a variety of depths are assessed. For the 1987 borehole, the SZC could only be detected using the temperatures at 0.55 m to 2 m (Fig. 29). The timing of the SZC did not change substantially when comparing the results from different depths for the 1987 borehole. In the 2015 borehole the SZC could only be detected more than once using the temperatures at depths of 2 m and 3 m and starts and ends earlier at 2 m compared to 3 m (Fig. 30). For the 1987 borehole, the AZC could only be detected more than once using temperatures measured at 1 m or 2 m depths. The timing of the AZC in the 1987 borehole did not differ between depths. In the 2015 borehole the AZC could be extracted from temperatures ranging from 0.25 m to 3 m. There is a weak tendency for the AZC to start and end earlier when the temperature is used from a larger depth.

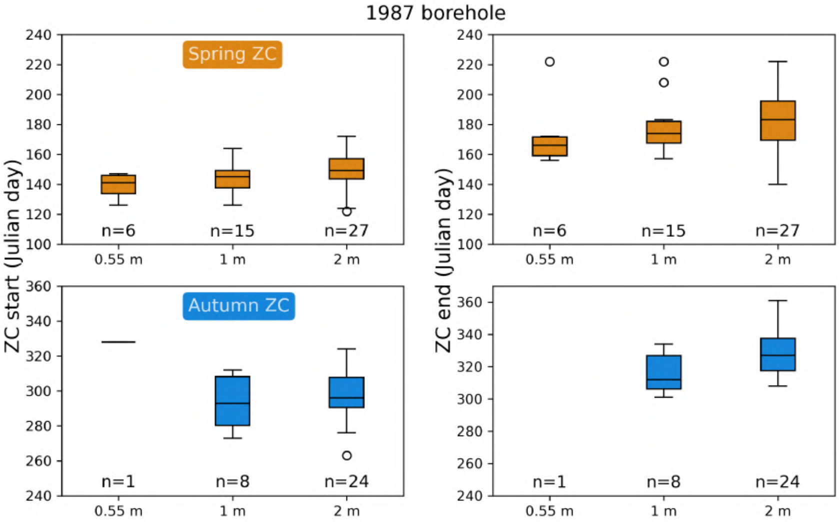

Figure 29: Comparison of distribution of spring (top) and autumn (bottom) ZC start and end dates between all possible thermistors depths within the AL used to extract the ZC periods for the 1987 borehole data. The *n* values show the sample size of ZC periods extracted using that given depth temperature series. Data source: PERMOS.

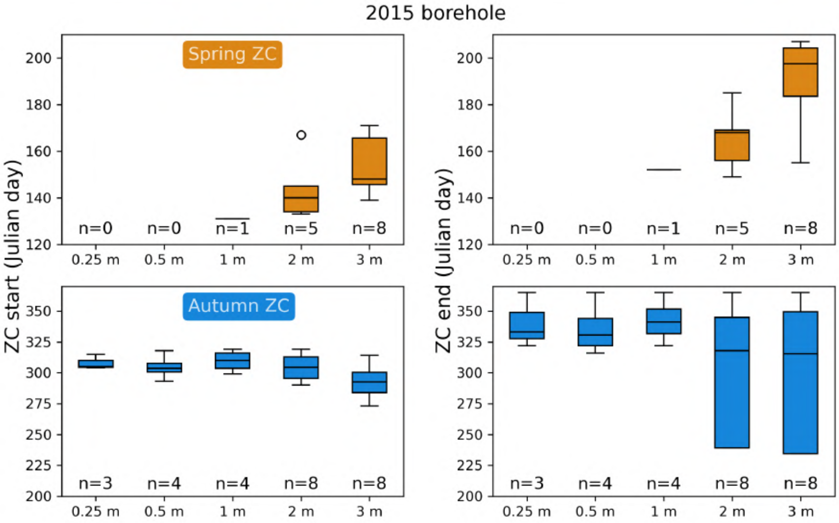

Figure 30: Comparison of distribution of spring (top) and autumn (bottom) ZC start and end dates between all possible thermistors depths within the AL used to extract the ZC periods for the 2015 borehole data. The *n* values show the sample size of ZC periods extracted using that given depth temperature series. Data source: PERMOS.

The long term trends in the duration, start and end dates of the spring and autumn ZCs are illustrated in Figure 31. There is a weak decreasing trend in the duration of the SZC which is driven by the end of the SZC shifting earlier in the year while the start of the SZC is not changing. The AZC has no clear pattern in how its duration is changing from 1994 to 2023. However, from the 2015 borehole, the AZC has been getting longer in duration from 2016 to 2023. The relatively constant 1994 - 2023 AZC duration aligns with its later start and end each year canceling each other out. This is especially observed in the 2015 borehole where the AZC is occurring later and later in the year. Note that the 2019 AZC detected from the 2015 borehole was not included in this analysis as it was considered an outlier with a duration of 98 days and an end date in March 2020. Now that the long-term context of climate and permafrost temperatures has been described, the next section will focus on the 2016 - 2023 period for the stratigraphy and deformation data recorded in the 2015 borehole.

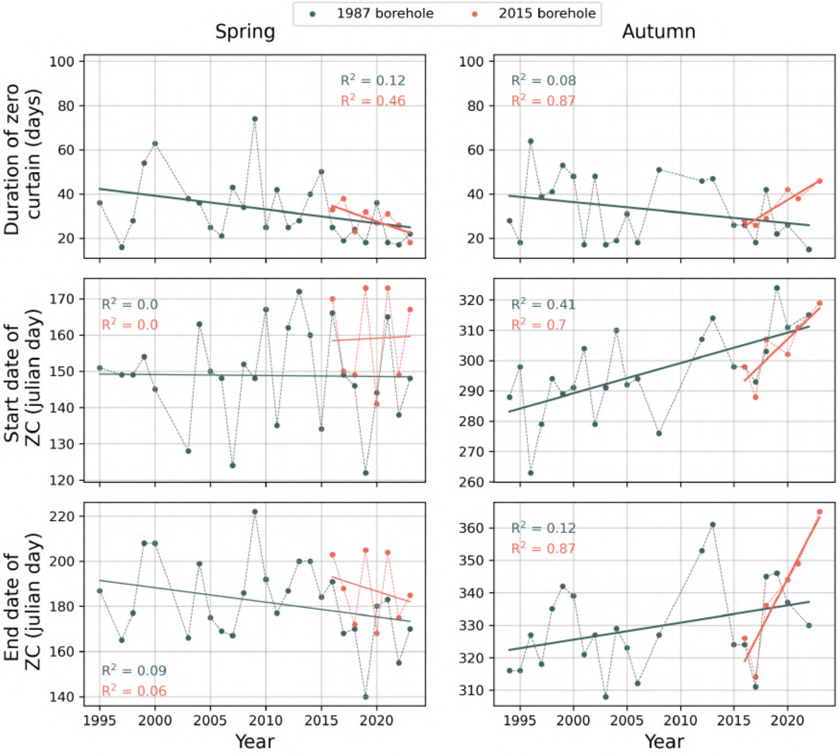

Figure 31: Long term regression analysis for the duration, start and end dates of the spring (left) and autumn (right) ZC using both the 1987 and 2015 borehole data. Data source: PERMOS.

## 4.3 Borehole stratigraphy

The following stratigraphy profile is based on a core analysis from 5 m to 33 m (Fig. 32). Above 5 m, the observations made during the drilling report that the coarse-blocky AL only extended to just before 3 m depth and below that ice was already observed. Note that between 3 m and 5 m no cores were available, so the presence of pure ice is also based on the limited observations during the drilling operation. Then, from 5 m onward the stratigraphy is based on the cores with mostly pure ice and some banded fine debris layers. At around 8.7 m a thicker layer of coarser rocks is found. At 9.6 m and 10.1 m there are two layers of sand mixed with some coarser gravel. From 10 m to about 15 m the ice has very little debris content. At around 15.3 m the fine debris content increases for a few decimeters and then there are sections of bulky ice around until at 16 m where debris content increases again. From 16.4 to 16.6 m there is a rocky layer with very little ice. From there to 19 m it is again a mix of fine to coarse grained ice. At 19.2 m there is another solid rock layer. Below that to 22.5 m it is again mostly pure bulky ice with larger grains. From 22.5 to 22.7 m there is a layer of coarse gravel debris followed by some layers of finer debris. Below 24 m is generally where the ice content begins to decrease. The core from 24.2 to 25.2 m has ice grains that are much coarser than all the other cores. At around 24.9 m there is a layer of solid rock. The core from 25.2 to 26 m was lost. From 26 m to 27 m, the ice content decreases to about 50%. From 27 m to 28 m, debris-rich ice is found with some coarser grains. Below 28 m, the ice is, for the most part, no longer present. From 29.5 to 33 m more coarse debris grains are observed, with also large air voids.

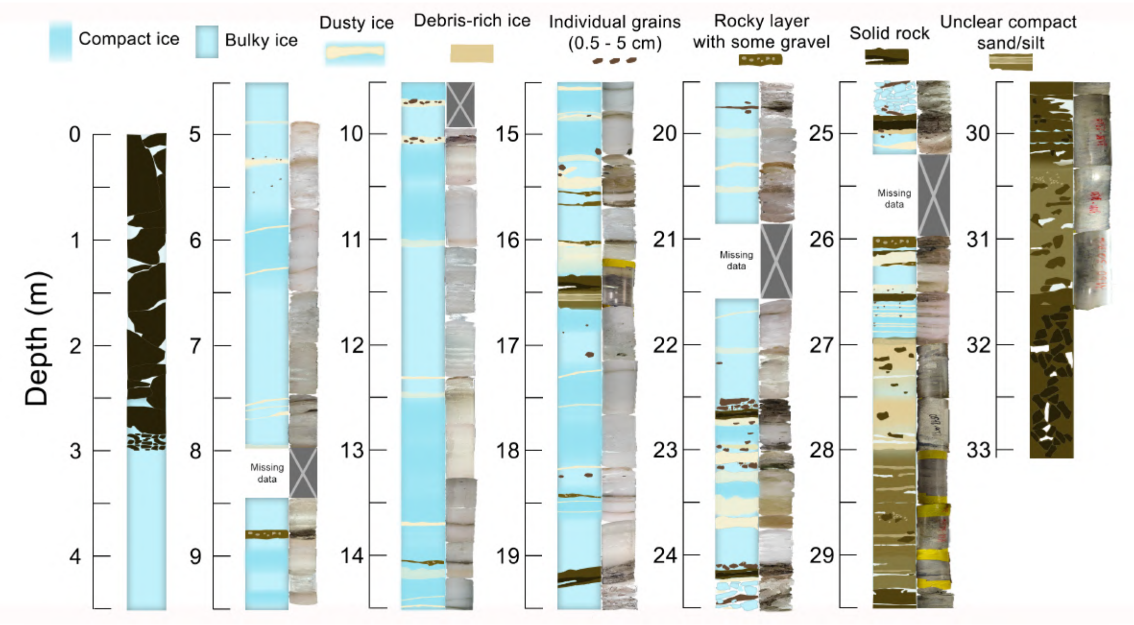

Figure 32: Stratigraphy based on the cores extracted from the 2015 drilling campaign. Both the sketch and the photos of each core ranging from 5 m to 33 m are shown. Compact ice refers to small-grained ice while bulky ice refers to ice with larger grains. Dusty ice describes layers with low debris content of very small grain sizes. Debris-rich ice is fine-debris that is saturated with ice. Unclear compact sand/silt is used for cores that were not taken outside their casing and it is difficult to assess the debris type and ice content. Data source: PERMOS. Core photos from PSI.

## 4.4 Borehole deformation patterns

The second section of the results aims to explore how the deformation in Murtèl rock glacier is distributed vertically in the borehole and at what depths seasonal cycles can be observed. The different surface deformation measurements available will also be compared. First, let us focus on the borehole deformation patterns with depth. It is important to understand that the deformation magnitudes measured by the inclinometer are integrated with depth, meaning that the surface deformation includes all the deformation below it. The highest borehole deformation is then, as expected, measured at the uppermost segment with an average of 12 cm/year and then decreases steadily with depth (Table 6). The total surface displacement measured by the borehole from May 2016 to July 2023 is 87 cm (Fig. 33). From the summer of 2017 onward, a secondary shear zone-like feature develops at 2 m depth. The depth of this secondary shallow shear zone decreases from 2 m to about 2.5 m by July 2023. The average annual deformation decreases by 2.5 cm/year from the surface to 2 m. The second highest average annual strain rates are found near the surface (Table 6). The highest standard error of the mean (SEM) is also found at the surface, indicating large inter-annual variability in deformation. In between the ALT and the primary shear zone the deformation gradually decreases with depth inside the ice-rich core. Around 7 m to 9 m, the deformation starts to decrease with depth in summer 2017 more rapidly and then inverts to increase with depth until 9 m (Fig. 33). Further down at around 21 m there is another increase in strain rate until the shear zone. In the middle of the main shear zone at 27.5 m the strain rate is highest at 0.04 year$^{-1}$ as the deformation drops to zero at the bottom of the shear zone. The shear zone depth range is quantified by inspecting the vertical profiles for the mean annual strain rate and the mean annual deformation (Fig. 34). The mean annual strain rate increases at about 26 m depth and reaches its peak at about 27.5 m, after which it drops to background rates at about 28.5 m depth.

Table 6: Average annual displacement and strain rate at various depths using the inclinometer data from the 2015 borehole at Murtèl rock glacier. Data source: PERMOS.

| **Depth (m)** | **Average annual displacement (cm/year) (±SEM)** | **Average annual strain rate (year$^{-1}$)** |
|---|---|---|
| 0 | $12(\pm 0.5)$ | $0.02$ |
| 2 | $9.5(\pm 0.7)$ | $3 \times 10^{-3}$ |
| 5 | $9.3(\pm 0.6)$ | $6 \times 10^{-4}$ |
| 10 | $9.1(\pm 0.5)$ | $7 \times 10^{-4}$ |
| 15 | $8.6(\pm 0.3)$ | $2 \times 10^{-3}$ |
| 20 | $8.0(\pm 0.3)$ | $1 \times 10^{-3}$ |
| 25 | $6.6(\pm 0.2)$ | $2 \times 10^{-3}$ |
| 27.5 | $3.5(\pm 0.1)$ | $0.04$ |
| 30 | $0.1(\pm 0.1)$ | $4 \times 10^{-3}$ |

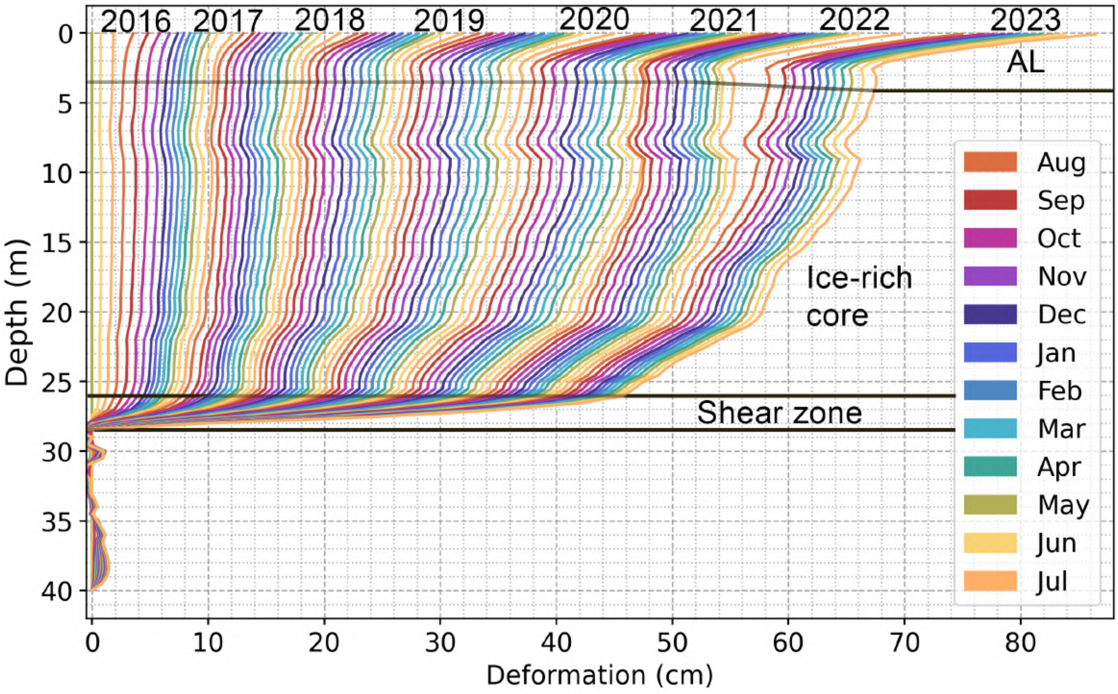

Figure 33: Monthly deformation profiles extracted from the inclinometer data in the 2015 borehole at Murtèl rock glacier starting in August 2016 and ending in July 2023. The three deformation-relevant layers of Murtèl rock glacier are labelled. Data source: PERMOS.

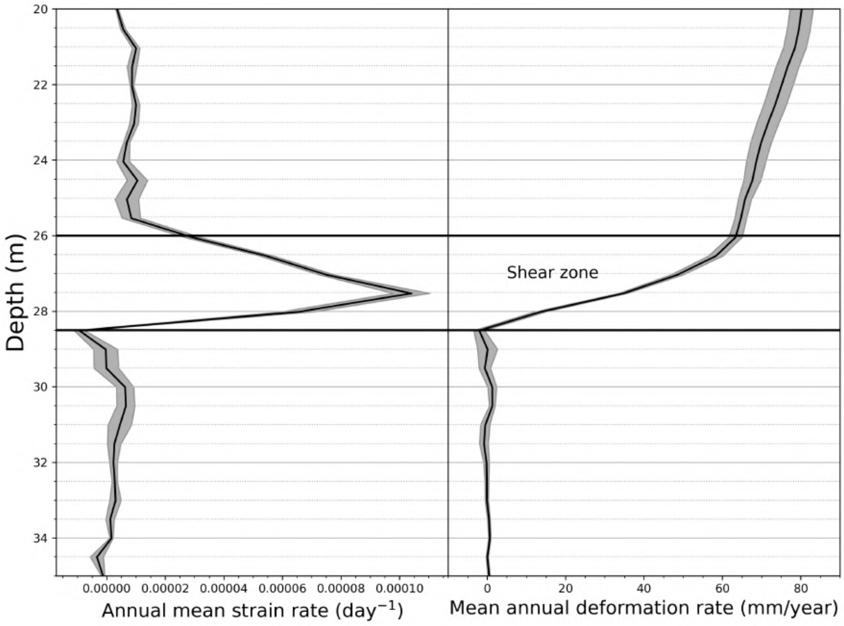

Figure 34: Vertical profiles of the annual mean strain rate and the mean annual deformation rate only from 20 to 35 m to identify the shear zone depth range. Data source: PERMOS.

The total horizontal deformation profile can also be split into horizontal cross sections to visualize the 2D directional movement of the inclinometer (Fig. 35). The general 2D direction of movement is northwest, which is also the aspect of Murtèl rock glacier. The length of a given year's segment is an indication of the total annual displacement of that given year. Note that both 2016 and 2023 are not complete, so their magnitude is not representative of the entire year. The 0 m and 1 m cross sections show seasonal changes in directions that occur during the warm phase. From the 2 m cross section down any seasonal changes in direction disappear, except during 2022 when the change in direction persists to somewhere between 10 m and 15 m. Below the shear zone, where in theory there is no deformation, the 2D direction is completely different and of much lower magnitude compared to above the shear zone. The unique deformation pattern seen in 2022 in both Figure 33 and Figure 35 will be discussed in Section 4.4.3.

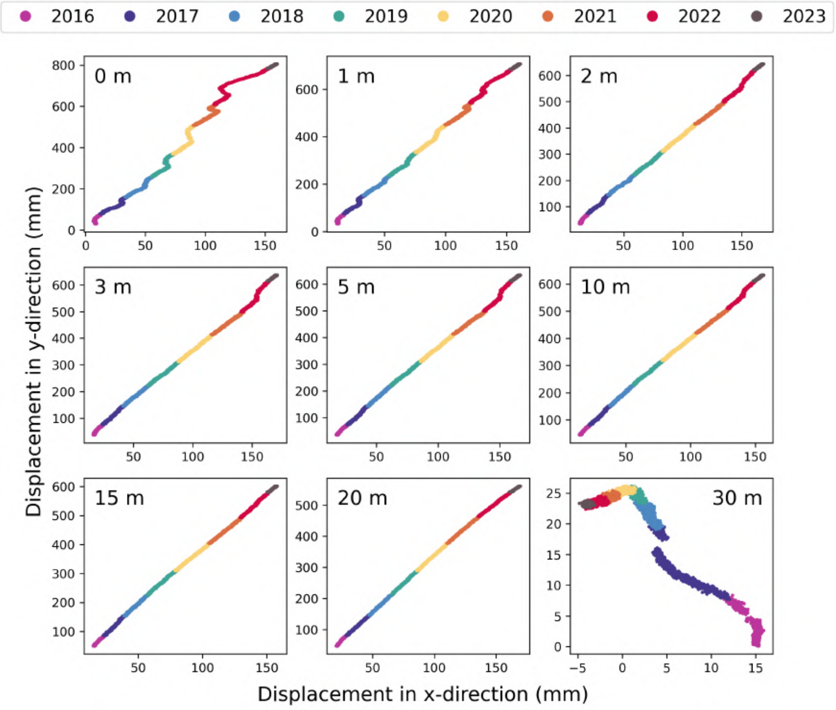

Figure 35: Top-down view of the horizontal direction of the borehole inclinometer movement where the x-direction aligns with West and y-direction with North. Data source: PERMOS.

### 4.4.1 Layer-specific annual deformation

Table 7: Average fraction of the total deformation at the surface that occurs in each layer with the corresponding depth range and layer-specific deformation rates. Data source: PERMOS.

| | **AL** | | **Ice-rich core** | | **Shear zone** | |
|---|---|---|---|---|---|---|
| **Fraction of total deformation at surface (%)** | 20.2 | | 23.6 | | 56.2 | |
| **Layer-specific deformation rate (cm/year)** | 2.6 | | 3.0 | | 5.9 | |
| | Top | Bottom | Top | Bottom | Top | Botom |
| **Depth (m)** | 0 | 3.5 | | 26.5 | | 28 |

There are three distinct layers in Murtèl rock glacier with each different deformation proportions: the AL, the ice-rich core and the shear zone. This next section focuses on describing the layer-specific deformation and its trends over time. The AL deformation represents about 20% of the total deformation at the surface (Table 7). Underneath the AL, the ice-rich core represents approximately 24% of the surface deformation. The shear zone contributes to the majority (56%) of the total surface deformation at Murtèl rock glacier. The annual contribution to the surface deformation of each layer varies from year to year (Fig. 36). The AL deformation is the most variable, with large increases during the years 2020 and 2022. Figure 36 also shows how the annual rates of GNSS deformation are almost consistently 3 cm/year higher than those measured at the top of the borehole. However, the year 2022 with the highest deformation has a good match between the GNSS and the borehole SAA deformation rate. For now, also note that the geodetic annual deformation rates differ from those of the GNSS and SAA. For a discussion between the difference surface deformation methods refer to Section 5.5. Figure 37 illustrates how the AL has the highest variation in annual strain rate, which is consistent with the high SEM values from Table 6. Over this period, the AL is accelerating at an average of 3.6 mm/year$^2$ (Table 8). The deformation of the ice-rich core is less variable, but follows a similar pattern to that of the AL, with higher contributions during 2020 and 2022 and an average acceleration of 2.5 mm/year$^2$. The year 2022 is unique because the fraction of ice-rich core deformation increases to about 34% compared to its average 23.6% (Table 7 and Fig. 37). On the other hand, years 2017 and 2021 have the lowest ice-rich core deformation at only about 10%. The fraction of deformation in the shear zone is generally consistent, providing approximately 7 cm/year of deformation. It experiences a general decelerating trend at a rate of 3.1 mm/year$^2$ from 2016 to 2023 (Table 8). Note that in Figure 36 the last year 2023 is not complete since the data ends in September due to the rockfall, hence why the deformation is much lower. The vertical annual profile of deformation rates shown in Figure 37 highlights the constant amount of shear zone deformation over the years.

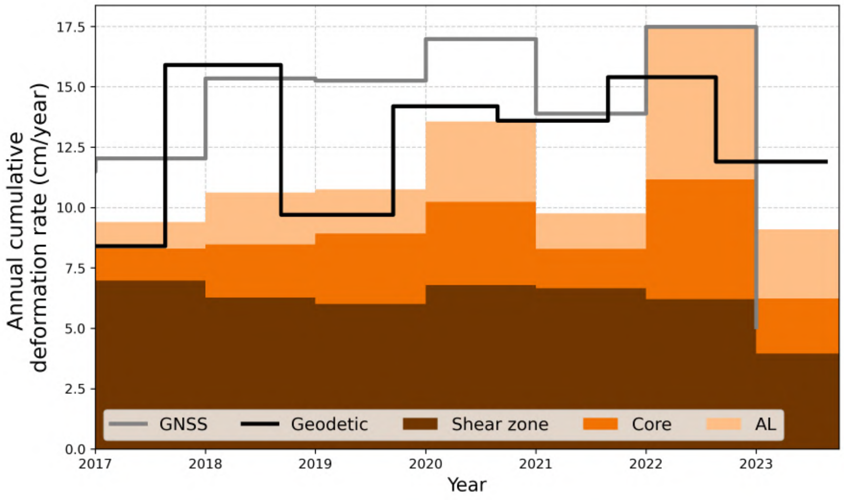

Figure 36: Layer-specific cumulative deformation measured in the borehole combined with the annual deformation measured by the GNSS and geodetic station. Data source: PERMOS and PermaSense.

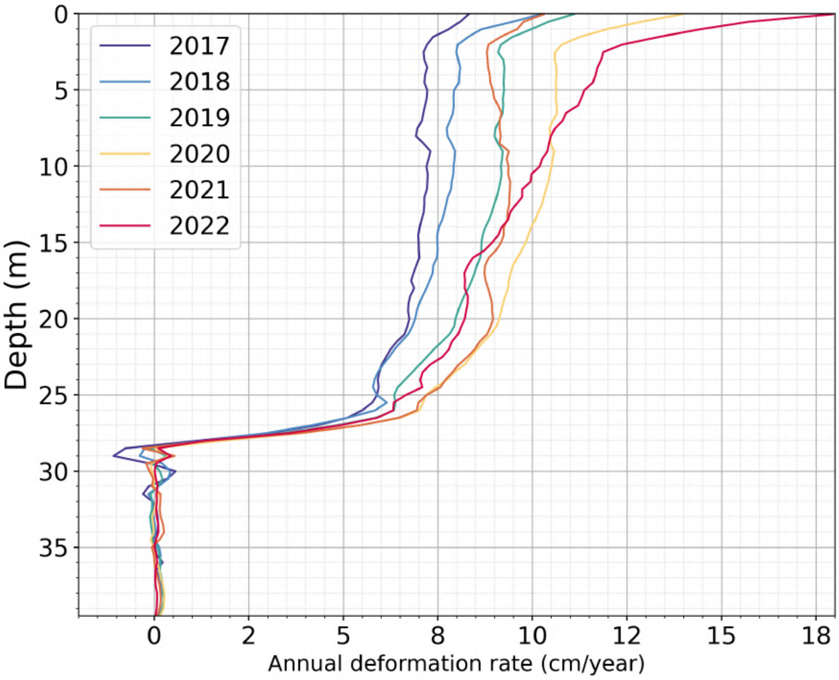

Figure 37: Vertical profile of annual deformation rate from 2017 to 2022 from Murtèl's 2015 borehole. Each profile line represents the amount of deformation from the first to the last day of that given calendar year. Data source: PERMOS.

Table 8: Layer-specific annual deformation rates for 2016 and 2023 and the corresponding deformation acceleration based on linear regression (Appendix 8.2) Data source: PERMOS.

| **Layer** | **Deformation rate 2016 (mm/year)** | **Deformation rate 2023 (mm/year)** | **Acceleration (mm/year$^2$)** |
|---|---|---|---|
| AL | 12.8 | 34.2 | 3.6 |
| Ice core | 19.2 | 34.0 | 2.5 |
| Shear zone | 70.1 | 51.7 | -3.1 |

### 4.4.2 Deformation seasonality with depth

So far annual or monthly data have been presented; next, the daily temporal resolution available from the borehole and GNSS deformation measurements is used to resolve seasonal patterns. Figure 38 shows the time series of the daily deformation rate of each layer. For most years, the deformation rate seasonal peaks are limited to the AL, while the ice-rich core and shear zone deformation remains constant. Seasonal peaks consistently occur around the beginning of September with a magnitude approximately three to four times higher than the background shear zone deformation rate of 0.25 mm/day. During the cold phase this background deformation drives the majority of total surface deformation which has rates close to 0.25 mm/day. For 2020 to 2022 a seasonal variation in daily deformation rates can also be observed down to the ice-rich core. The years 2020 and 2022 have relatively high surface deformation rates of 1-2 mm/day. In 2020 the seasonal peak in deformation rate can be seen roughly down to 5 m depth (Fig. 39). In 2022 the large increase in deformation rate during September can be observed down to almost 15 m. The time when the maximum deformation rate is reached stays the same across depths. The year 2021, on the other hand, strangely decreases in deformation during the warm phase, and the ice-rich core deformation drops below zero. For this year, the decreasing signal of the deformation rate can be observed down to 10 m. The unique deformation events of 2021 and 2022 will be described in Section 4.4.3. The year 2016 shows seasonality across all layers with the AL deformation reaching its peak first and then the ice-rich core and shear zone deformation peaking about a month later. During June 2016 in the top 2 m the deformation rate decreases to almost zero before accelerating for the rest of the summer (Fig. 39).

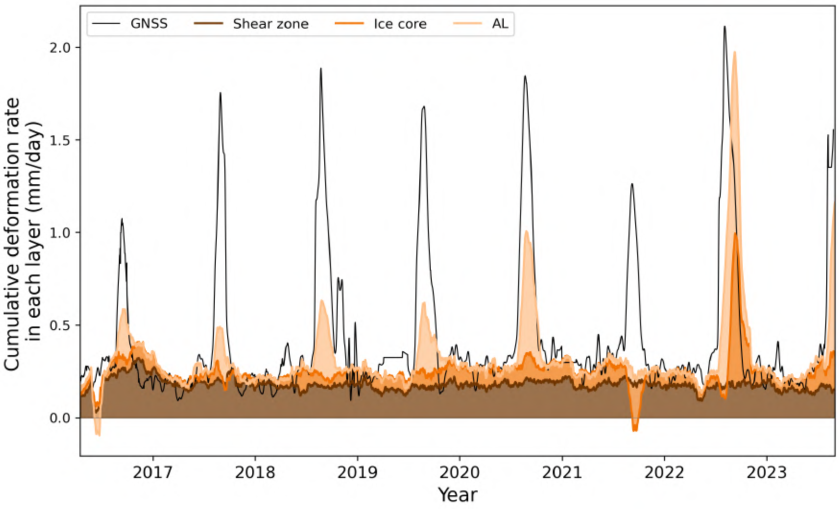

Figure 38: Daily borehole deformation rate cumulative over each layer and the daily deformation rate measured by the GNSS station. Data source: PERMOS and PermaSense.

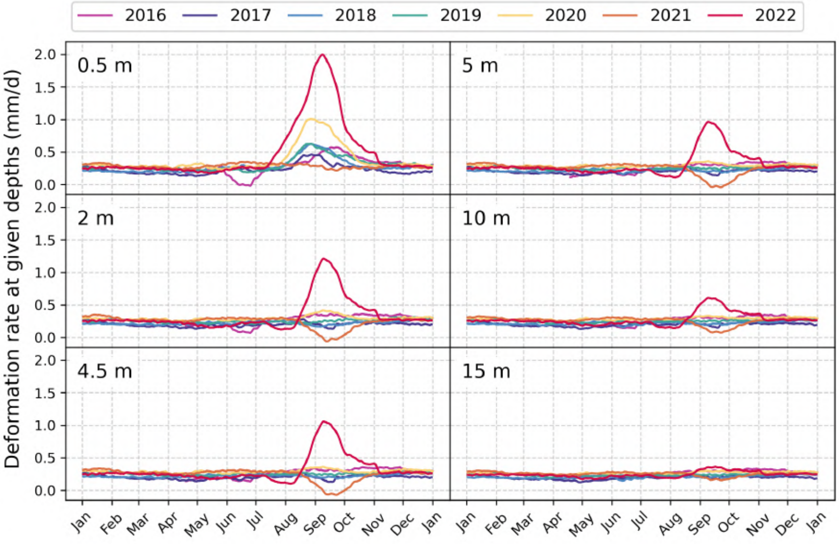

Figure 39: Annual cycle in daily deformation rate measured at various depths in the borehole at Murtèl rock glacier from 2016 to 2022. Data source: PERMOS.

### 4.4.3 Special borehole deformation events

For years 2021 and 2022 the deformation patterns with depth stand out. The 2021 deceleration starts in the middle of August, when segments from 1 m down to about 15 m start to slow down (Fig. 40). The minimum velocity is reached about one month later in the middle of September. It takes another month for the deformation rates to increase and return to pre-event rates. At depths of 2 to 5 m the deformation rate becomes negative during the peak of the event (Fig. 41 and 42). The deformation profile in Figure 41 shows that above the 2.5 m depth the AL continues to creep, even though at unusually slow rates. However, below 2.5 m the deformation is atypically increasing with depth. At deeper depths the deformation rate never goes below zero. The shear zone deformation remains unchanged during this period. The top-down view of the 2D position of the inclinometer segments illustrates the substantial double change in the direction of creep from the surface down to 1.5 m depth (Fig. 42). The first change in direction happens at the beginning of September, and the second at the beginning of October, which restores the original direction of movement. The first shift aligns with the midpoint of the period with decreasing deformation rates and the second shift aligns with the midpoint of the increasing deformation rates period. Further down, from 2 to 5 m there is backward movement in the 2D plane, which also starts in the beginning of September and ends in the beginning of October. Below 5 m the direction of creep is for the most part unaffected.

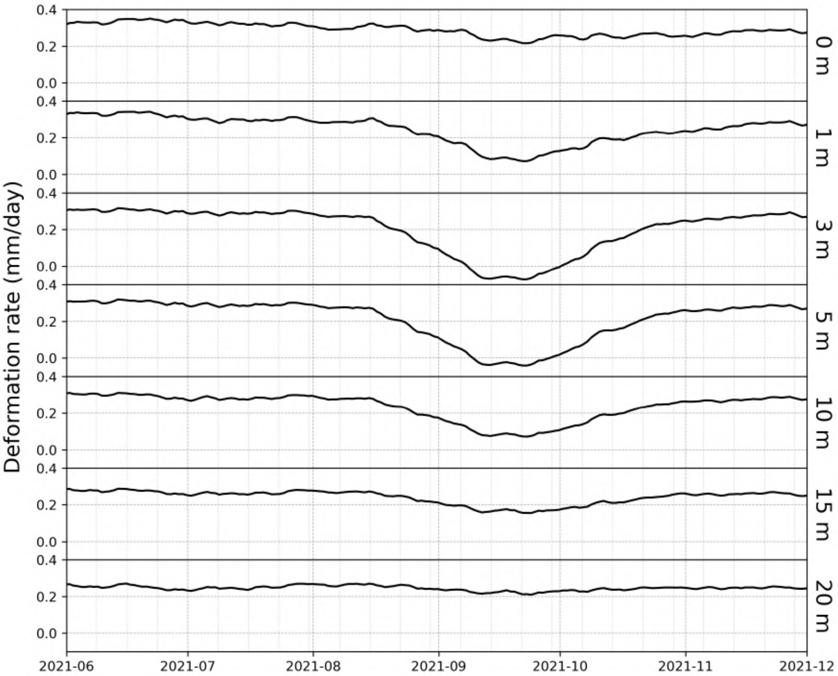

Figure 40: Deformation rate during the 2021 deceleration at various depths in the 2015 borehole. Data source: PERMOS.

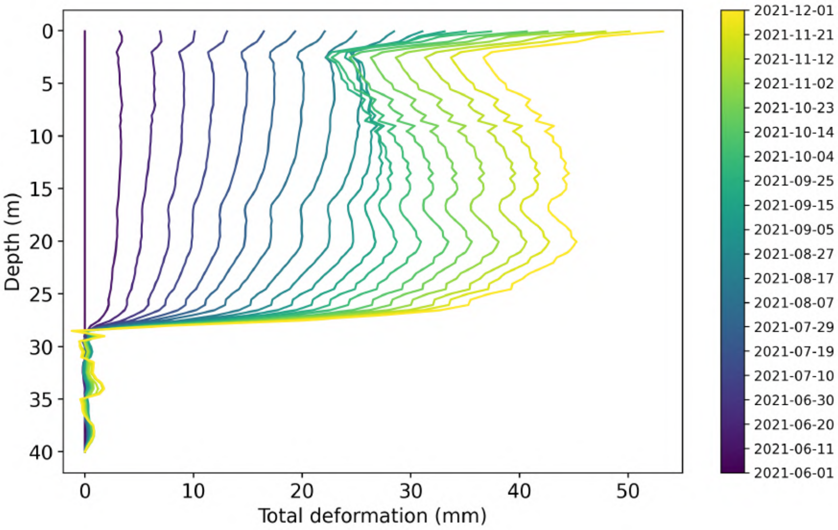

Figure 41: Deformation profile with depth from June to December 2021 during unique deceleration event in Murtèl 2015 borehole. Data source: PERMOS.

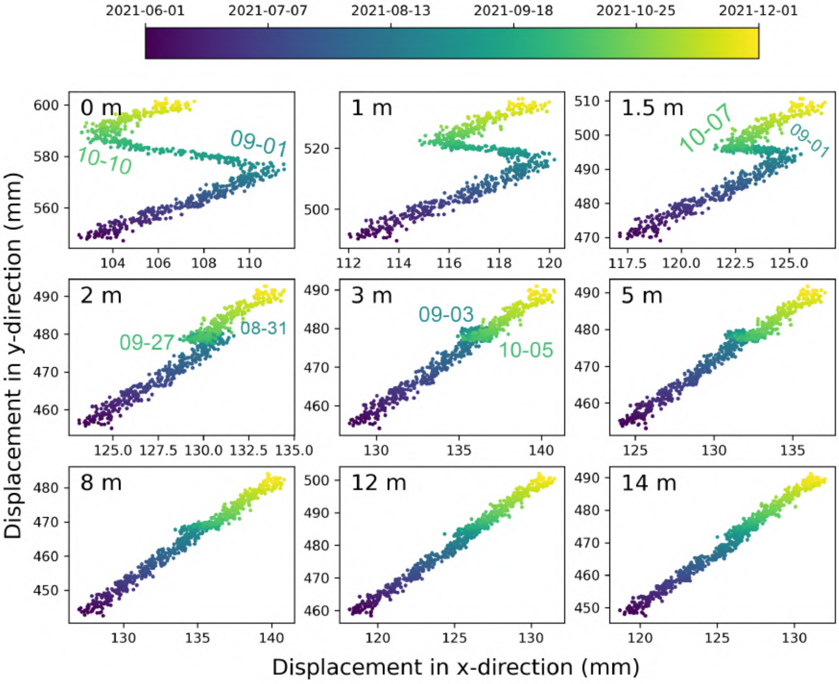

Figure 42: Top-down view of the horizontal direction of the borehole inclinometer movement where x-direction aligns with West and y-direction with North from June to December 2021. Data source: PERMOS.

The second unique deformation event occurred during the warm phase of 2022. From around mid-July to mid-September the borehole inclinometer measured about 10 cm of movement at the surface, which is the most pronounced warm phase displacement out of the whole 2016 to 2023 period. Around mid-May the segments near 2.5 m start to slow down above an inversion depth at around 3 m (Fig. 44). Then around mid-July the segments in the top 1.5 m begin to accelerate substantially while the others below it begin to decelerate with the lowest velocities achieved at around 2.5 m depth (Fig. 43 and Fig. 44). Two weeks later around 25 July the first major change in the 2D direction of movement occurs from 0 m to 1.5 m (Fig. 45). Then, also about two weeks later on 10 August the segments from 2.5 m to 15 m start to accelerate (Fig. 43). The secondary change in 2D direction in the top 1.5 m occurs sometime around mid-August. Toward the end of August depths from 2 m to around 8 m experience their single change in 2D direction. This lasts until early September, which is also when the peak deformation rate occurs on September 9 with maximum surface daily deformation of 2 mm/day. The acceleration is measured down to just over 15 m depth, which is the only year when this occurs. After the peak, the deformation rate decreases for about two months until pre-event rates of 0.25 mm/day are reached at the start of December (Fig. 43).

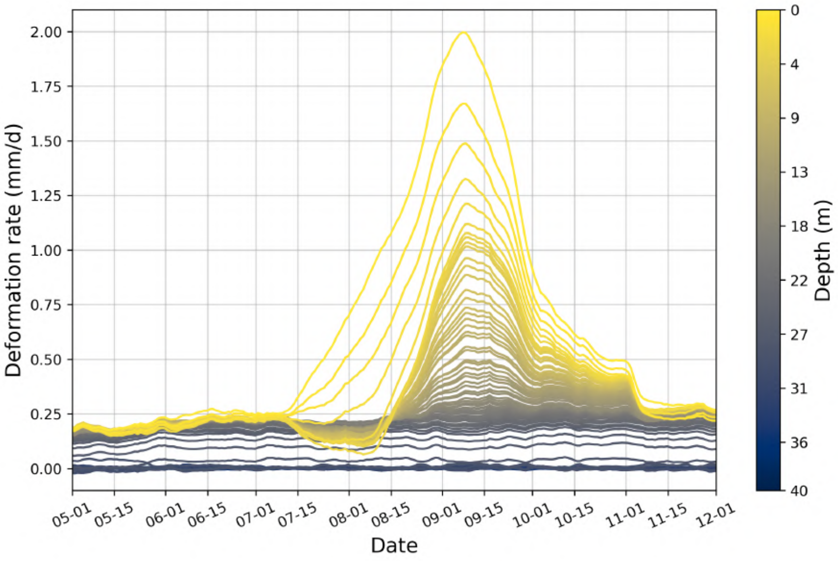

Figure 43: Deformation rate during the large 2022 acceleration for depths every 0.5 m. Data source: PERMOS.

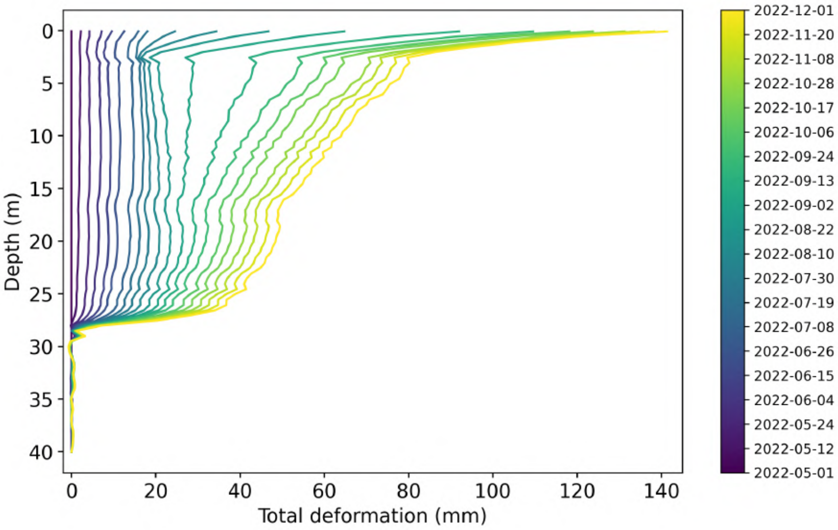

Figure 44: Deformation profile from May to November 2022 during unique acceleration event in Murtèl 2015 borehole. Data source: PERMOS.

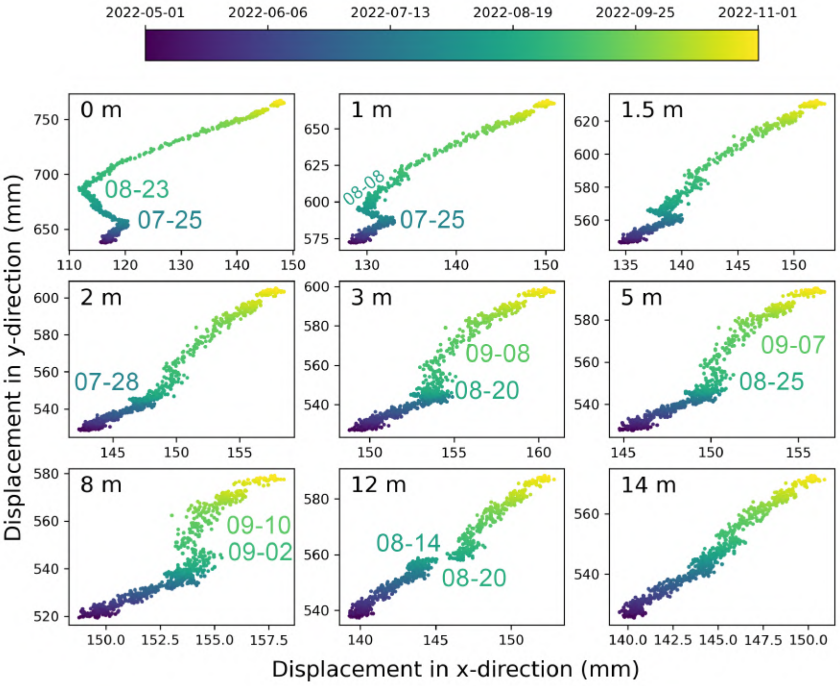

Figure 45: Top-down view of the horizontal direction of the borehole inclinometer movement where x-direction aligns with West and y-direction with North from May to November 2022. Data source: PERMOS.

# 5 Discussion

## 5.1 Patterns in the atmosphere and climate

The first part of the discussion will aim to address the first research question on long-term trends in the climate and state of permafrost at Murtèl rock glacier. For this rock glacier, like many other alpine locations, there has been significant atmospheric warming since the start of the climate record at the *in-situ* station in 1997. During the entire 25-year-long measurement period, air and surface temperatures have risen by about 1°C each. The MAAT in 2022 reached -0.9°C, which is beginning to exceed the lower limit of -1°C of the mountain permafrost distribution (Haeberli, 1985). The focus period of 2016-2023 is especially warm when considering the long-term temperature record. The mean air temperature during these last 8 years is -0.88°C, while over the entire measurement period the mean air temperature is -1.4°C. The annual temperature anomalies relative to the 1997-2005 baseline are constantly positive from 2014 onward. Murtèl is a relatively cold rock glacier compared to other rock glaciers in the Swiss Alps. For example, the surface temperature at Murtèl is about 1-2°C colder than that of Schafberg rock glacier (Mühll et al., 1998). In general, these warming temperatures are likely to continue to increase the area of mountain permafrost that is susceptible to degradation.

The long-term trends in annual mean air and surface temperatures are also not always synchronous (Section 4.1.1). The differences between air and surface temperatures on a rock glacier are largely driven by variability in the snow cover duration. During the spring when air temperatures start to go above 0°C the snow cover acts to maintain temperatures close to or below 0°C thanks to its high albedo. In fact, the years with especially cold surface temperatures (2003, 2009 and 2021) are also years with relatively warm permafrost temperatures which is indicative of long snow cover durations. During the warm phase, the surface temperature is usually higher than the air temperature because of the high absorption of incoming solar radiation from the rocky surface with a low albedo. The connection between annual surface temperature and snow cover can also be seen by the higher variability in annual surface temperature compared to air temperature due to the higher variability in snow cover. The coefficient of variation (CV) is the SD described as a percentage of the mean of the entire period. The mean annual snow height has a CV of 39%, while the warm phase liquid precipitation has a CV of 26%. This emphasizes how the interannual variability in the snow accumulation is greater than summer rainfall and hence why there are large fluctuations in annual means of surface temperature.

## 5.2 Borehole permafrost temperatures

As with the warming MAAT the borehole temperatures have also been a warming at Murtèl rock glacier. The mean annual borehole temperature has increased by 2.5°C, 1.25°C and 1.0°C at depths 2.5 m, 4.5 m and 9.5 m, respectively, over 25 years. Noetzli and Pellet (2024) compiled a large mountain permafrost dataset from around Europe and Svalbard to calculate an average warming rate of 0.41°C per decade from 2013 to 2022 at 10 m depth. At the same depth Murtèl warms on average 0.3°C per decade, which is slightly lower. However, it is important to remember that Murtèl is a very ice-rich mountain permafrost body. Noetzli and Pellet (2024) finds a decadal warming rate of only 0.05°C for ice-rich permafrost. So, when the high ice content of Murtèl rock glacier is considered, it is warming at an alarming rate. A correlation matrix between MAAT and mean annual borehole temperatures at various depths reveals that below 4.5 m the correlation coefficient starts to drop below the statistical significance level. This about the depth of the ALT which indicates that the AL at an annual timescale acts to decouple the atmospheric conditions to the permafrost conditions. Amschwand, Wicky, et al. (2024) using the data from the micrometeorological PERMA-XT station on Murtèl, found that indeed only 10% of the incoming surface ground heat flux penetrates below the AL. Interestingly, between 15 m and 21 m the correlation strength between MAAT and borehole temperature increases again. Processes such as energy advection through an intra-permafrost system of air voids or even channels may explain the strong synchronicity between MAAT and mean annual borehole temperatures at such depths (Wirz et al., 2016).

When distinguishing between the warm and cold phases, the warm phase has a much more consistent warming trend compared to the cold phase. Therefore, in the long term the warm phase drives the permafrost warming for Murtèl rock glacier. The warm phase mean temperature at 4.5 m surpasses the freezing point in 2019, which is probably a direct cause of the ALT deepening starting one to two years after. In general, the ice-rich Murtèl rock glacier is warming at a rate faster than most ice-rich permafrost landforms and this is largely driven by the increasing warm phase temperatures. The cold phase borehole temperature in the top 5 m has much higher interannual variability compared to the warm phase temperature at the same depth (Fig. 22 and 23). This is further evidence that the largely variable annual snow depth is the main control of the subsurface temperature, whereas the air temperature drives the shallow depth temperatures of the warm phase. In fact, there is no significant correlation between the cold phase air temperature and the cold phase borehole temperature down to 8.5 m (Fig. 24). This supports the idea that snow cover is an effective insulator for permafrost at shallow depths. At deeper depths, the cold phase borehole temperature is influenced by the mean air temperature of the preceding warm phase (Fig. 46). This is because it takes more than five months for surface temperature changes to reach those depths, which exceeds the duration of the warm phase.

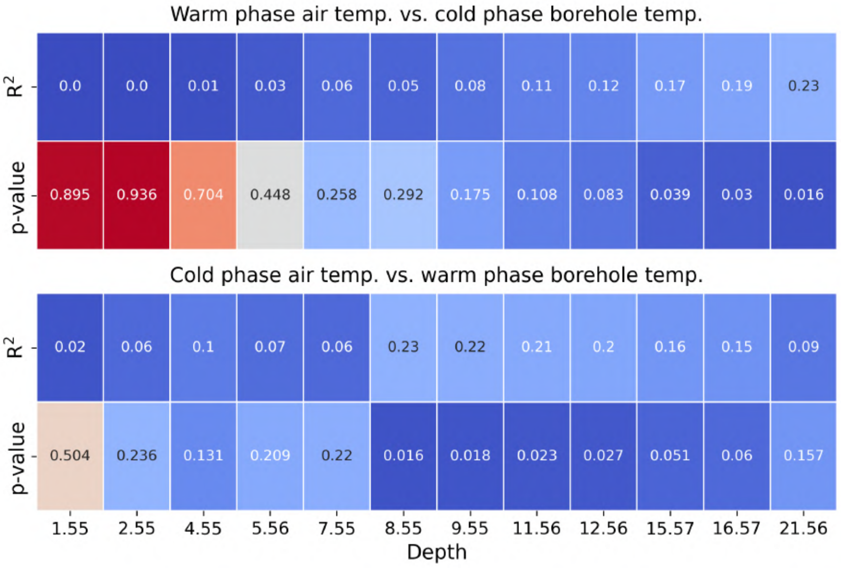

Figure 46: Linear correlation analysis results between the warm phase mean air temperature and cold phase mean borehole temperatures (top) and the cold phase mean air temperature and warm phase mean borehole temperature (bottom) at depths with continuous records from 1998 to 2022 in the 1987 borehole at Murtèl rock glacier. Data source: PERMOS.

### 5.2.1 ALT

The ALT of Murtèl rock glacier is roughly consistent between the 1987 and 2015 boreholes at 3.5 m to 4 m. However, towards the end of both boreholes' time series the ALT starts to increase. For 2016 and 2017 there are ALT measurements from both boreholes and the older borehole measures an ALT that is about 1 m larger than the ALT from the 2015 borehole. The explanation of this discrepancy is unclear. The 1987 shallow-depth thermistors show no signs of drift when inspecting the ZC temperature values. When comparing the 2.5 m sensor from the 1987 borehole and the 2 m sensor from the 2015 borehole the temperature records match closely. The two boreholes are only a few meters apart so local spatial variations in permafrost temperatures are unlikely to play a role. The 1987 borehole does not produce an ALT for after 2017 as too many relevant sensors stopped working. A similar increase to that of the 1987 borehole from 2012 to 2017 can also be observed at the end of the 2015 borehole record from 2021 to 2023. There are no signs of sensor drift in the 2015 borehole temperatures. It is possible to compare the 3 m sensor in the 2015 borehole with the 4.5 m sensor in the 1987 borehole to observe that both thermistor chains measure gradual warming of the warm phase after 2021. The increase in ALT of 2022 and 2023 is visualized in Figure 47 and one can see how the increase originates from a short-lasting increase in the depth of the 0°C isotherm. The increase occurs towards the end of the warm phase. For both of those years, the warm phase in the AL is especially warm and long-lasting. This might have resulted in there being enough time and ground heat flux to melt permafrost ice at the permafrost table and thereby increasing the ALT.

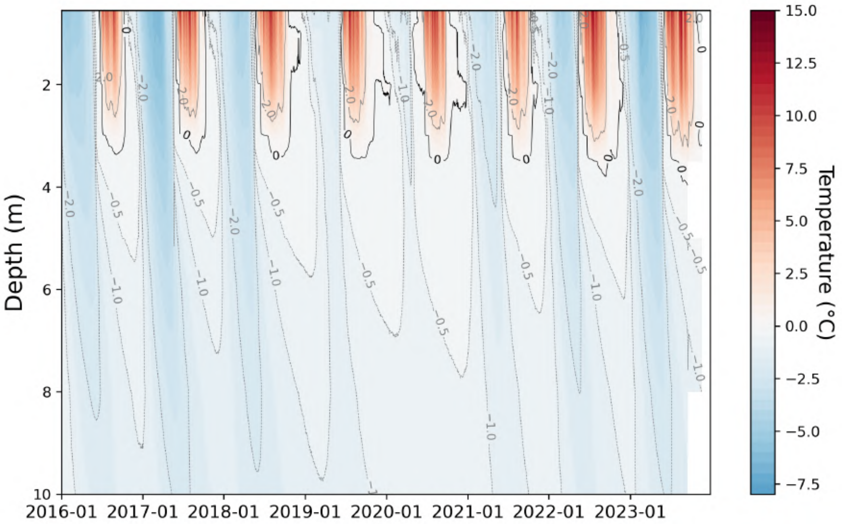

Figure 47: Temperature contour plot from the surface down to 10 m depth from the 2016 to 2023 period measured in the 2015 borehole at Murtèl rock glacier. The extracted 0°C isotherm is highlighted.

### 5.2.2 Zero curtain

The novel method developed in this thesis to extract ZC periods is compared to the ZCs dates extracted by Kenner et al. (2020) also from the 1987 Murtèl borehole, but using the 2.5 m temperature series. The exact method they used is not described. Although the temperature time series used comes from a depth differing by 50 cm, the extracted dates match closely. Kenner et al. (2020) only report the start date for the SZC and the end dates for the AZC. The distribution of the SZC start dates from Kenner et al. (2020) and this thesis are very similar (Fig. 48). The AZC end dates match relatively less well with the ones from Kenner et al. (2020). In general, this supports the robustness of the extraction method developed in this thesis. From 1995 to 2023 the SZC shows a slight shortening pattern which may be caused by the warming cold phase temperatures in the AL allowing less seasonal ice to form. The AZC is steadily shifting later in the year due to the general increase in air temperature, which leads to the AL reaching freezing temperatures later in the year. For example, October 2022 in Switzerland was 3.2 - 4.7°C above the mean air temperature in 1981-2010 (Noetzli and Pellet, 2023). The pattern is observed for the 1987 borehole, but even more pronounced in the 2015 borehole period, suggesting an accelerated delay of the AZC timing. This also aligns with the later start of the cold phase in more recent years described in Section 4.2.2. The duration of the AZC has also been linked to the amount of moisture in the AL before the freezing begins (Renette et al., 2023). The higher water content in the AL before the AZC, the more energy and thus the longer it takes to complete the phase change. The only proxy available for water storage in the AL before the start of the AZC is the sum of rainfall from September and October. However, no correlation was found between the September and October precipitation and the duration of the AZC at Murtèl rock glacier ($R^2 = 0.02$). Hoelzle et al. (2002) also reports a general trend for a later occurrence of the AZC, resulting in an overall shorter period when the AL experiences below-freezing temperatures.

The depth of the temperature series used to extract the ZC periods has an important effect on the result. By comparing the spring ZC timing across different depths, the SZC seems to start and end earlier for shallower depths. Although, the ZC extraction was not successful using the ground surface temperature (GST) time series, but only the borehole temperature, manual extraction can be done using the GST in 2019 to find that the snow melt begins on June 3 compared to the AL spring ZC starting on June 22 in 2019. Similarly, the snowmelt energy peaks illustrated in Figure 52 occur primarily just before the start of the ZC period extracted from the bottom of the AL. So, the snowmelt-based ZC happens before the melt phase in the AL. Moreover, some of the snowmelt water may refreeze in the AL and contribute to a longer AL melt phase, which extends the AL SZC duration. This would suggest that the spring melt is a top-down process that starts at the surface and continues down through the AL. Ikeda et al. (2008) also found the SZC to end earlier at shallow depths in Büz North rock glacier, although the start of the SZC was similar from the ground surface temperature series to the temperature series at 2 m depth. In a permafrost soil site in Alaska the shallowest temperature sensor at 8 cm had the earliest start to the SZC (Hinkel and Outcalt, 1994). So, this top-down melting process during the SZC also applies to non-rock glacier permafrost sites.

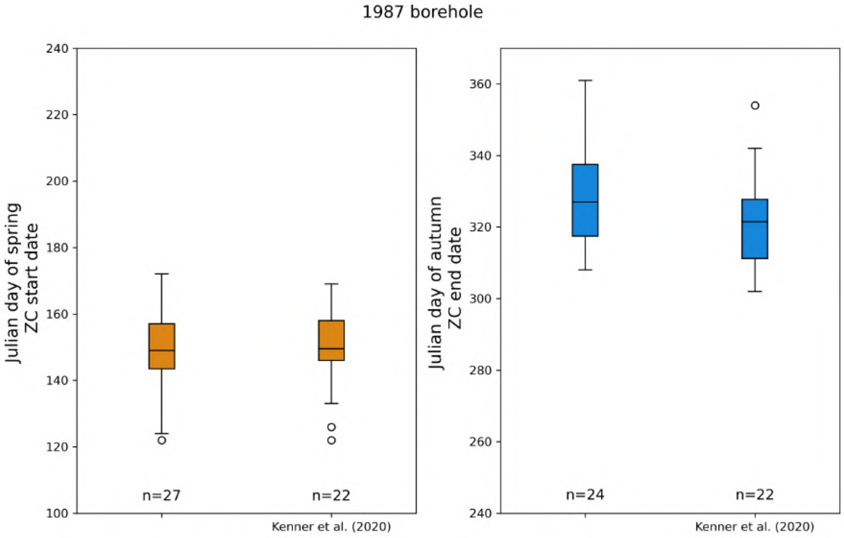

Figure 48: Comparison of the extracted SZC start dates (left) and the AZC end dates (right) between the values from this investigation using the 1987 borehole 2 m temperature series and those from Kenner et al. (2020) using the 1987 borehole 2.5 m temperature series. Data source: PERMOS.

On the other hand, the AZC seems to start and end later for shallower depths. This indicates that the freezing at the end of the warm phase may be a bottom-up process in which the AL starts to freeze first near its bottom. However, the difference in dates is not as substantial as for the SZC. In fact, Hinkel and Outcalt (1994) observed an opposite process described as a freezing front lowering from the surface downward during the AZC. This is more likely to be the case, as the snow-free surface is the most coupled to atmospheric cooling. In general, the timing of the ZCs is sensitive to the depth from which the temperature series is used. The ZC periods are important for describing the amount of meltwater that is likely to be produced during seasonal melt and available to infiltrate the rock glacier, which may have a role in explaining deformation patterns.

## 5.3 Borehole deformation

The second part of this discussion concentrates on the second research question regarding the deformation patterns with depth at various time scales. First, it is worth acknowledging that the inclinometer installed in the 2015 borehole is the longest available record of daily borehole deformation in a rock glacier. This allows for the patterns of the vertical distribution of deformation described in this section to have high validity specific to Murtèl rock glacier. The current eight-year lifespan of the SAAF inclinometer is due to the slow deformation rate of Murtèl rock glacier. The surface average annual deformation rate of 12 cm/year measured by the inclinometer is in good agreement with previous values reported by L. Arenson et al. (2002) and Noetzli and Pellet (2024). The first measurements of Mutèl surface deformation using aerial photos from 1932 to 1971 were in the range of a few centimeters per year (Barsch and Hell, 1976). The annual inclinometer measurements from L. Arenson et al. (2002) report a surface average annual deformation rate of 7 cm/year. Based on this, Murtèl rock glacier during the 2016-2022 period is 71% faster at the surface compared to the 1987 - 1995 period.

Moving below the surface in the AL, the vertical deformation profile has a very distinct secondary shear zone-like feature at around 2 - 2.5 m depth, where the deformation increases suddenly with depth. This does not align with the ALT at around 3.5 - 4.5 m. A possible reason for this could be vertical protrusions of seasonal ice that act as a sliding plane for the loose coarse debris above. During the drilling in late summer of 2015 it was reported that at 2.7 m some ice was found. It could be that below 2.5 m the air voids become smaller and ice can form more easily. The bottom of this secondary shear zone drops by 0.5 m from 2017 to 2023, which is discussed in Section 5.8.1. This secondary shear zone should be counted as a real natural signal because when comparing the cumulative surface deformation of the inclinometer and the geodetic measurements the values only differ by 2 cm (Fig. 66). The inclinometer installed at Ritigraben rock glacier also produced a similar secondary shear zone at the bottom of the AL (Lugon and Stoffel, 2010). However, the deformation profiles reported by Buchli et al. (2018) do not show this feature near the surface. The depth of the uppermost sensor in their inclinometer profiles actually decreases in depth over time. It is not clear whether this is due to some added correction for the loss of elevation due to the downslope movement or over time the top few sensors were omitted in the visualization.

The AL, on average, makes up 20% of the surface deformation. The fraction of deformation in the AL varies a lot annually with some years like 2022 experiencing 7 cm of horizontal displacement in the AL which is about 37% of the surface deformation. In comparison to the few values available in the literature, this is a very high fraction of deformation that occurs in the AL. From the inclinometer measurements from 1987 to 1995 in the older borehole at Murtèl only 8% of the total surface deformation was driven by the AL (Table 9) (L. Arenson et al., 2002). On Büz North rock glacier a shallow borehole measured AL movements of only 0.8 - 1.6 cm/year while total surface displacements ranged from 83 - 107 cm/year based on geodetic measurements (Ikeda et al., 2008). The grain size distribution of the AL may affect how much deformation it experiences. The AL of Büz North rock glacier has pebble-sized debris, as well as sand and silt that partly fills the pore spaces (Ikeda et al., 2008). On the other hand, Murtèl has a much coarser AL with some boulders ranging in diameters of a few meters. However, the effect of grain size of AL deformation processes, such as stick-slip events, needs further research to evaluate its importance.

Further down in the borehole, the ice-rich core, on average, contributes to 26% of the total surface deformation, which is relatively large. For instance, Buchli et al. (2018) found that above the shear zone almost no deformation could be measured in the 7-10 months of data collected by their inclinometers. Murtèl rock glacier has abnormally high ice content in its core, and it is likely that this allows higher plastic deformation to occur within the more than 20 m of close to pure ice layer. The ice-rich core deformation contribution from the 1987-1995 period was even higher at 33% (Table 9). This might indicate that at Murtèl rock glacier the ice-rich core might be decelerating in the long term. However, within the 2016-23 period the ice-rich core deformation has been accelerating at a 2.5 mm/year$^{-2}$ rate. So, there is not enough conclusive evidence for claiming a general temporal trend in the ice-rich core deformation component.

Below the ice-rich core the shear zone is found to be from 26 to 28.5 m which is shallower than the 28 to 31 m shear zone described by the 1987 borehole data (L. Arenson et al., 2002). Assuming a similar identification approach between this thesis and L. Arenson et al. (2002), the shear zone has risen by about 2 m over a 25-year period. Part of this change may be due to the vertical loss in permafrost ice due to thaw over two decades. However, given the cold permafrost temperatures, it is unlikely that there has been more than a few centimeters of annual vertical loss in permafrost (Appendix 8.6). The rising shear zone towards the surface would have implications on the rock glacier deformation as a shallower shear zone can receive more meltwater infiltration. This is seen, for instance, when comparing Murtèl and Schafberg rock glaciers. Schafberg has two main shear zones at 11 to 16 m and 24 to 26 m, which have been observed to be more sensitive to meltwater input (L. Arenson et al., 2002, Kenner et al., 2020, Bast et al., 2024). Murtèl, on the other hand, did not show a significant correlation between the amount of snow available to melt in spring and the maximum deformation. In fact, the year 2021 had the highest snowmelt but one of the lowest deformation. The shear zone, on average, accounts for 56% of the surface deformation. This matches closely with the 59% that L. Arenson et al. (2002) reports from the 1987 - 1995 period also at Murtèl. The small decrease in the shear zone contribution to surface deformation aligns with the decreasing trend found within the 2017 to 2023 period of -1.5 mm/year$^2$. Compared to the few other rock glaciers with borehole deformation data, this shear zone contribution is rather small. At Muragl rock glacier, the shear zone is claimed to make up 77% - 82% of the surface deformation (L. Arenson et al., 2002). At Schafberg rock glacier the first shallower shear zone accounts for 97% of surface deformation (L. Arenson et al., 2002). At Furggwanghorn rock glacier almost all surface deformation occurs at the shear zone (Buchli et al., 2018). The amount of deformation that occurs at the shear zone is important to consider when describing the controlling processes of rock glacier deformation (see Section 5.4).

Table 9: Fraction of the total surface deformation at the end of the study period that occurs in each layer in comparison to the 1987–1995 period measured by L. Arenson et al. (2002) and PERMOS.

| | AL | | Ice-rich core | | Shear zone | |
|---|---|---|---|---|---|---|
| | 1987–95 | 2016–23 | 1987–95 | 2016–23 | 1987–95 | 2016–23 |
| Fraction of total deformation at surface (%) | 8 | 20.2 | 33 | 23.6 | 59 | 56.2 |

### 5.3.1 Seasonal deformation patterns with depth

The high temporal resolution borehole deformation data spanning multiple years allows for the first time to assess at which depth seasonality in deformation can be observed in a rock glacier. So far, the literature has been limited to identifying seasonal cycles only at the surface of rock glaciers (Fig. 49). For the slow-moving Murtèl rock glacier, there is a clear seasonal cycle with AL deformation peaking in the warm phase and decreasing in the cold phase (Fig. 38). For the two special deformation events in 2021 and 2022 there is also a seasonal signal down to 15 m depth. In 2020 the large acceleration in the AL is also partially due to an acceleration in the ice-rich core. There is no seasonal cycle for the shear zone deformation at Murtèl rock glacier. However, at Furggwanghorn rock glacier Buchli et al. (2016) lower shear zone strain rates are reported in winter than in summer, suggesting that at some sites the shear zone can experience seasonal variations in deformation. At Murtèl, the shear zone is below the depth of zero annual amplitude of temperature variations, so it does not experience sufficient changes in temperature to show seasonality in deformation. Cicoira et al. (2019) claim that if there is water infiltrating the shear zone, the shear zone deformation can change as a result. However, at Murtèl there is no data available to say whether the pore water pressure at the shear zone varies seasonally and if its absence is the direct cause of the absence of seasonality in shear zone deformation. So, the seasonal cycle of deformation at Murtèl rock glacier for most years occurs only in the AL, except for some years with higher deformation in which the ice-rich core deformation also increases in the warm phase.

The timing of the seasonal peaks in AL deformation is consistent year-to-year. The acceleration begins towards the beginning of August and reaches its peak in the beginning of September (Fig. 56). There are only two years, 2019 and 2022, when the acceleration in deformation starts shortly after the end of the spring ZC. This does not match the findings from Büz North rock glacier where at 4-5 m an acceleration in the strain rate was regularly measured a few days after the start of the spring ZC (Ikeda et al., 2008). Moreover, at Schafberg rock glacier the acceleration in surface deformation was observed to start even a few days before the start of the SZC (Kenner et al., 2020). Buchli et al. (2013) also reports a higher AL deformation in their inclinometer during spring melt at Furggwanghorn rock glacier. The Gemmi and Grosses Gufer rock glaciers

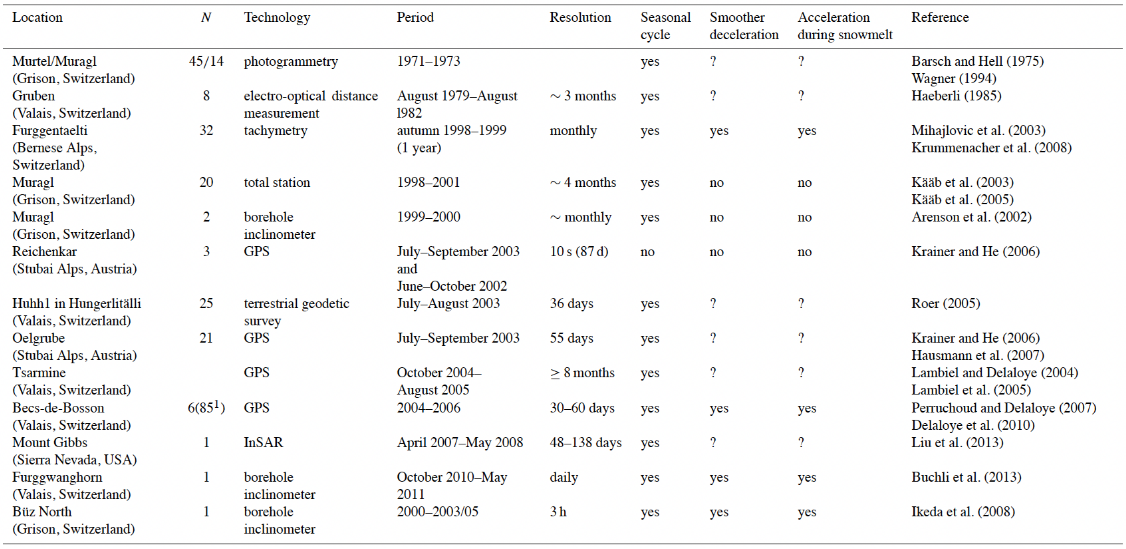

| Location | $N$ | Technology | Period | Resolution | Seasonal cycle | Smoother deceleration | Acceleration during snowmelt | Reference |
|---|---|---|---|---|---|---|---|---|
| Murtel/Muragl (Grison, Switzerland) | 45/14 | photogrammetry | 1971–1973 | | yes | ? | ? | Barsch and Hell (1975)<br>Wagner (1994) |
| Gruben (Valais, Switzerland) | 8 | electro-optical distance measurement | August 1979–August 1982 | $\sim$ 3 months | yes | ? | ? | Haeberli (1985) |
| Furggentaelti (Bernese Alps, Switzerland) | 32 | tachymetry | autumn 1998–1999 (1 year) | monthly | yes | yes | yes | Mihajlovic et al. (2003)<br>Krummenacher et al. (2008) |
| Muragl (Grison, Switzerland) | 20 | total station | 1998–2001 | $\sim$ 4 months | yes | no | no | Kääb et al. (2003)<br>Kääb et al. (2005) |
| Muragl (Grison, Switzerland) | 2 | borehole inclinometer | 1999–2000 | $\sim$ monthly | yes | no | no | Arenson et al. (2002) |
| Reichenkar (Stubai Alps, Austria) | 3 | GPS | July–September 2003 and June–October 2002 | 10 s (87 d) | no | no | no | Krainer and He (2006) |
| Huhh1 in Hungerlitälli (Valais, Switzerland) | 25 | terrestrial geodetic survey | July–August 2003 | 36 days | yes | ? | ? | Roer (2005) |
| Oelgrube (Stubai Alps, Austria) | 21 | GPS | July–September 2003 | 55 days | yes | ? | ? | Krainer and He (2006)<br>Hausmann et al. (2007) |
| Tsarmine (Valais, Switzerland) | | GPS | October 2004–August 2005 | $\geq$ 8 months | yes | ? | ? | Lambiel and Delaloye (2004)<br>Lambiel et al. (2005) |
| Becs-de-Bosson (Valais, Switzerland) | 6(85[1]) | GPS | 2004–2006 | 30–60 days | yes | yes | yes | Perruchoud and Delaloye (2007)<br>Delaloye et al. (2010) |
| Mount Gibbs (Sierra Nevada, USA) | 1 | InSAR | April 2007–May 2008 | 48–138 days | yes | ? | ? | Liu et al. (2013) |
| Furggwanghorn (Valais, Switzerland) | 1 | borehole inclinometer | October 2010–May 2011 | daily | yes | yes | yes | Buchli et al. (2013) |
| Büz North (Grison, Switzerland) | 1 | borehole inclinometer | 2000–2003/05 | 3 h | yes | yes | yes | Ikeda et al. (2008) |

Figure 49: List of rock glacier kinematics studies with high enough temporal resolution to resolve a seasonal cycle at the surface. Table from Wirz et al. (2016).

in the Valais also show seasonal surface acceleration in April to May during or shortly after the spring snow-melt (Noetzli and Pellet, 2024). Including the Wirz et al. (2016), Kenner et al. (2020) and Noetzli and Pellet (2024) studies, there are 8 out of 11 rock glacier kinematic studies that identified surface acceleration during or a few days after the snowmelt period (Fig. 49). The time lag between the end of the SZC and the acceleration in AL deformation is relatively long for Murtèl rock glacier compared to other monitored rock glaciers. The average end of the SZC is around mid-July at Murtèl, which means that it still takes two to three weeks until the surface begins to accelerate around the beginning of August. Then from the end of the SZC to the maximum peak in GNSS there is on average a time lag of 50 days. The spring-melt processes controlling seasonal acceleration in rock glacier deformation will be explored in Section 5.4.2.

### 5.3.2 Interannaul trends in Murtèl RGV

The annual rate of borehole deformation measured near the surface reaches annual maxima in 2020 and 2022 while relatively low magnitudes in 2017, 2018 and 2021. The borehole deformation in 2021 and 2022 shows unique deformation vertical profiles and this might raise the question of its validity in terms of rock glacier wide velocity. However, the GNSS station also measures low annual deformation in 2021 and high deformation in 2022. Therefore, part of the origin of the very different 2021 and 2022 borehole deformation profiles is still likely to be due to natural processes (see Section 5.6). Other notable patterns in the annual GNSS deformation are the low magnitude in 2017 and the high magnitude in 2020 which also aligns with that of the borehole surface. From 2017 to 2020 Noetzli and Pellet (2024) report a general increase in

RGV from most of the rock glaciers monitored in Switzerland. This aligns with the pattern observed at Murtèl rock glacier of a peak annual deformation in 2020. In 2021 most rock glaciers around the Alps experienced a strong acceleration in annual velocity (Fig. 50) (Bast et al., 2024; Kellerer-Pirklbauer et al., 2024). However, Murtèl in 2021 had a noticeably lower annual velocity compared to the rest of the 2016-23 period. Noetzli and Pellet (2024) claim that in 2022-23 most rock glaciers in Switzerland experienced a deceleration likely due to lower winter precipitation. Murtèl, on the other hand, shows signs of substantial acceleration in 2022 and 2023, even though measurements end in August 2023. Figure 50 shows how the Engadin region, where Murtèl is located, does not experience as much acceleration from 2017 to 2020 compared to the other regions of the Alps. The conflicting interannual patterns between Murtèl and most other rock glaciers in the Alps hints at the unique dynamics of Murtèl rock glacier. It is a much slower rock glacier than the others around the Engadin (Fig. 50). The other slow-moving rock glacier in Figure 50 is Marmagnun, which is located in the same catchment and aspect as Murtèl rock glacier. The annual trends in Murtèl RGV were found to correlate with less than 10% of the other RGV time series from the Alps (Kellerer-Pirklbauer et al., 2024). The same study suggests that for a rock glacier's velocity to be used as a mountain permafrost ECV parameter it needs to correlate with at least 60% of the other available RGV time series Kellerer-Pirklbauer et al., 2024). The different kinematics of Murtèl rock glacier are probably due to its unique internal structure, which is discussed in Section 4.3. Therefore, the annual velocity of Murtèl rock glacier should not be used as an ECV parameter as it is not synchronous with most of the rock glaciers monitored in the Alps.

Although the surface velocity of Murtèl is not in sync with most of the other rock glaciers in the region, it still shows strong correlations with its MAAT. The relationship between the MAAT and the annual deformation measured in the few uppermost sensors of the inclinometer is relatively strong (p-value = 0.08) (Fig. 51). The correlation strength between the MAAT and the annual deformation rate decreases until it weakens at around 4 - 6 m. So, this would suggest that the annual air temperature is not related to the annual deformation rates at depths below the AL. The link between MAAT and the annual deformation rates of a rock glacier is the basis to RGV being a parameter of the Mountain Permafrost ECV. For Murtèl rock glacier this correlation is only valid in the AL.

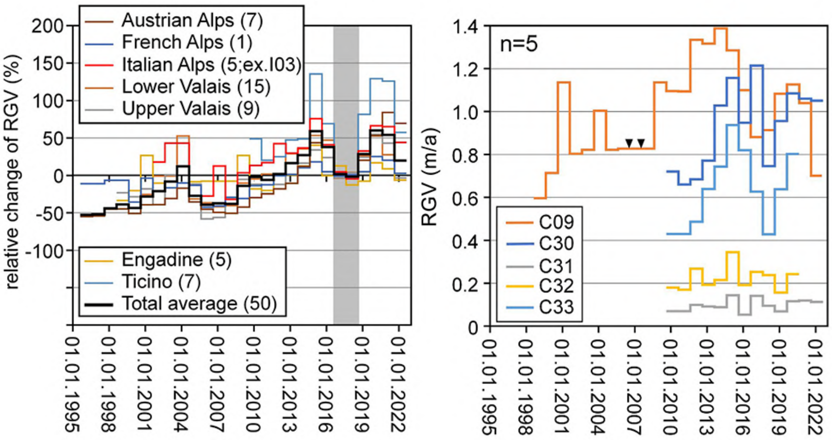

Figure 50: Left: annual long term trends in rock glacier velocity (RGV) displayed as a change (%) relative to the reference period of 2016-18 from rock glaciers across the Alps. Right: Annual trends in absolute RGV for the monitored rock glaciers in the Engadin region where C09 = Büz North, C30 = Muragl, C31 = Murtèl, C32 = Marmugnun, C33 = Chastelets. (Kellerer-Pirklbauer et al., 2024).

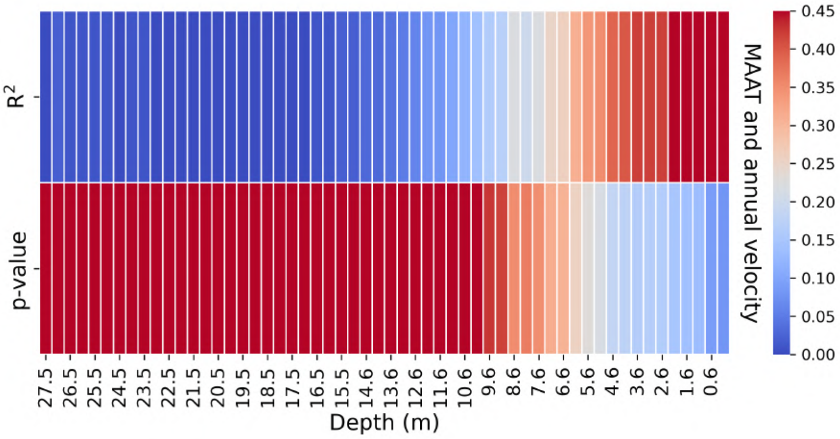

Figure 51: Matrix of linear regression results between the MAAT and the annual deformation rate measured from the surface to the bottom of the shear zone in the borehole from 2017 to 2022. Data source: PERMOS.

## 5.4 Seasonal controls of rock glacier deformation

The third part of this discussion considers the third research question on the potential seasonal controls of deformation with depth at Murtèl rock glacier. The high temporal resolution borehole deformation data allows one to inspect the potential thermal and hydrological processes driving seasonal deformation variations with depth. The driving processes for the annual cycle in rock glacier deformation can be divided into winter, spring, and summer processes. The first section will discuss how snow accumulation affects permafrost temperatures within the rock glacier and how this might affect seasonal acceleration. The later sections will explore the importance of the AL thermal regime for deformation.

### 5.4.1 Winter controls

Winter snow conditions play an important role for permafrost temperatures, which in turn affect deformation. The effect of snow cover on ground temperatures is easily observed when comparing the air temperature and the borehole temperature at 0.25 m during the cold phase in Figure 52. The cold phase borehole temperatures at 0.25 m are milder compared to the air temperature due to the insulating effect of the snow cover. The dynamics of early winter snow accumulation are crucial in determining the borehole temperatures for both the cold and the following warm phase. Mühll et al. (1998) found that the mean snow height from November to January had a strong positive correlation ($R^2 = 0.64$) with the mean temperature at 3.5 m in March and April at Murtèl rock glacier. This investigation also found that years with more early winter snow experience warmer temperatures at the top of the permafrost table (TTOP) for the following spring in both the 1987 and 2015 borehole (p-value = $1 \times 10^{-6}$, 0.01 respectively) (Fig. 53). The high snow depth early in the winter acts to insulate the shallow permafrost from cold winter air temperatures so that by next spring the permafrost is relatively warm compared to a snow-poor early winter. For instance, the 2019-20 winter was relatively dry, but early in the winter there was large snow accumulation and the cold phase borehole temperatures are milder than the more generally snow-rich 2017-18 winter (Fig. 52, Appendix 8.3). The other important winter characteristic is the duration of an insulating snow cover. The threshold thickness of the snowpack to decouple the underlying permafrost from the atmosphere is about 70 cm (Keller, 1994; Mühll et al., 1998; Hoelzle et al., 2002; Amschwand et al., 2023). A long duration of when snow height is greater than 70 cm leads to higher warm phase ice-rich core temperatures measured both in the 1987 and 2015 borehole (p-value = $2 \times 10^{-4}$, 0.08 respectively) (Fig. 53). So, only considering the expected future decrease in the duration of snow cover under a warming climate, permafrost temperatures at Murtèl rock glacier can be expected to actually decrease in the long term. Figure 52 illustrates how, for shallow depths, the cold phase temperature is not necessarily representative of the warm phase temperature. However, for the 8 m depth, when the cold phase temperatures are cold, then the warm phase also tends to be colder. In fact, the mean temperature of the ice-rich core during the cold phase has a significant positive correlation with the warm phase temperature at depths below the AL (p-value = 0.003) (Fig. 54). In the AL the warm phase temperatures are strongly coupled to the atmosphere, and therefore are independent from the temperatures of the preceding cold phase. The cold phase air temperature is found to have strong correlations with the warm phase borehole temperatures from 8 to

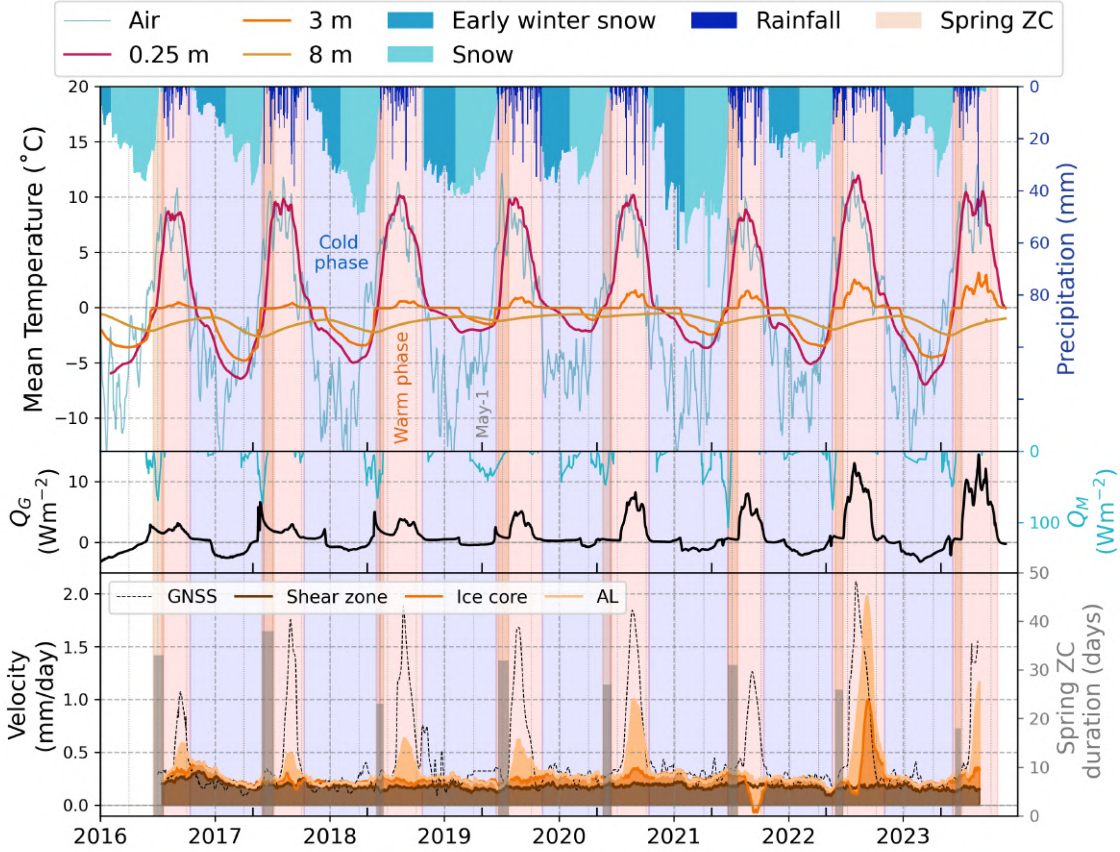

Figure 52: Thermal, hydrological controls of daily layer-specific deformation rates with emphasis of cold (blue-shaded) versus warm (orange-shaded) phase aspects. The spring ZC is shaded in the darker orange. Top: daily snow height, daily precipitation rate for Murtèl, air temperature, borehole temperatures at 0.25, 3, and 8 m from 2015 borehole. Middle: ground heat flux ($Q_G$) calculated at 3.5 m in 2015 borehole and snowmelt energy flux ($Q_M$). Bottom: daily layer-specific deformation rate for AL, ice core and shear zone; GNSS daily deformation rate; spring ZC duration. Data source: PERMOS, PermaSense and MeteoSwiss.

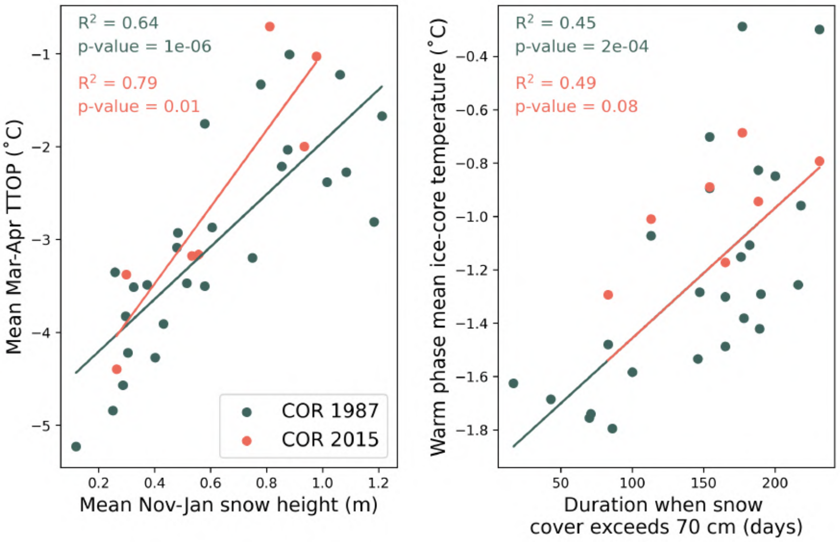

Figure 53: Linear regressions between: mean early winter snow and early spring TTOP (left) and duration of snow >70 cm and warm phase ice core temperature (right) for both the 1987 borehole (1997-2022) and 2015 borehole. Data source: PERMOS.

16 m. So, the snowpack development regulates winter permafrost temperatures, which, in the ice-rich core, influence the temperatures during the following warm phase, potentially altering deformation dynamics.

From classical ice flow laws it is known that ice deformation depends on its viscosity, which in turn is temperature sensitive (Glen, 1955). There is a strong correlation ($R^2 = 0.85$ ) between the mean ice-core temperature of the warm phase and the annual deformation rate at 10 m in the borehole. So, for an ice-rich rock glacier like Murtèl, it is plausible to claim that warmer permafrost temperatures lead to higher deformation and for below 5 m they are strongly controlled by the snowpack characteristics. Another aspect raised by Ikeda et al. (2008) is that a long duration of a thick snow cover prevents the widespread refreezing of any water found in the pores of the AL. The persistence of liquid water throughout the winter leads to higher saturation and hence high hydraulic conductivity during the next spring melt. So, the extent of a thick snow cover in winter can have an impact on the meltwater infiltration in spring, which has been proposed to be important for driving higher deformation rates (Ikeda et al., 2008, Kenner et al., 2020, Fey and Krainer, 2020).

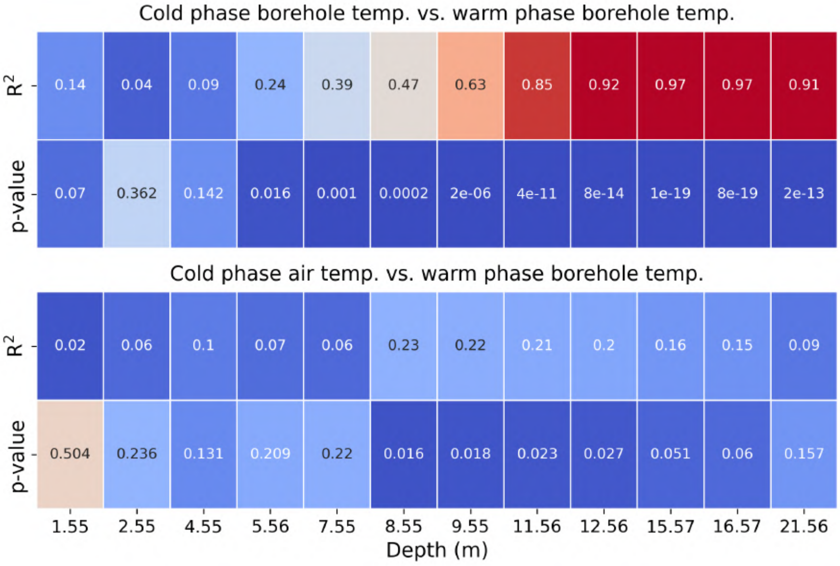

Figure 54: Matrices of R$^2$ and p-values from linear regression between the mean cold phase borehole temperature and the mean warm phase borehole temperature at varying depths (top); and between the mean cold phase air temperature and the mean warm phase borehole temperature at varying depths (bottom) from 1998 to 2022. Data source: PERMOS.

### 5.4.2 Spring controls

As mentioned in Section 5.3.1 the dynamics of the spring melt are important in relation to the onset of seasonal acceleration in rock glacier deformation. First, it is important to acknowledge that $Q_G$ and $Q_M$ have their maximum before the spring ZC, which is when the ground ice in the AL is melting (Fig. 52). The dynamics of the spring ZC discussed here are limited to the AL and not the surface snow. The date when the spring ZC ends has a significant negative correlation with the mean temperature of the AL (p-value = 0.05) (Fig. 55). In other words, the AL temperatures are higher for years when the spring ZC ends earlier. The end date of the spring ZC also has a strong negative correlation with when the AL thickness reaches its maximum (p-value = 0.02) (Fig. 55). After the end of the SZC the $Q_G$ starts to increase again and for years after 2020 it reaches its annual maximum later in the warm phase. So, for years when the spring ZC ends earlier, the AL reaches its maximum thickness later in the warm phase and has a higher temperature as there is more time for the positive ground heat flux to contribute to the AL's thermal energy.

Both the timing of the end of the melt period and the AL temperatures are important for the surface deformation measured at the GNSS station. The end date of the spring ZC and the date of maximum snow-melt energy both have a significant negative correlation with the annual maximum GNSS velocity (p-value = 0.04 and $3 \times 10^{-4}$ respectively) (Fig. 55). In other words, years with earlier ends to the snow and ice melt periods experience a larger seasonal peak in surface deformation rate. At first, this seems to suggest that the earlier the production of meltwater, the higher the maximum surface velocity. However, on average, it takes 50 days from the end of the spring ZC to when the GNSS maximum deformation occurs. This is a much longer time delay from the spring ZC to when the inclinometer and GNSS begin to accelerate compared to other rock glaciers (Section 5.3.1). So, even though the timing of the end of the melt phase has strong correlations with the maximum surface velocity, it is likely not due to hydrological processes, but rather to thermal processes. In fact, the mean AL temperature and the date of maximum ALT both have a positive moderate correlation with the annual maximum GNSS deformation rate (p-value = 0.08 and 0.06 respectively) (Fig. 55). The thermal controls of deformation will be further discussed in Section 5.4.3.

The hydrological processes during the melt phase were still found to be important in past rock glacier kinematics research. Most of the previous literature indicates a strong link between meltwater infiltration and creep in rock glaciers (Ikeda et al., 2008, Kenner et al., 2020, Fey and Krainer, 2020, Bast et al., 2024). Generally, the large, coarse air voids in the AL lead to a high drainage efficiency and a fast discharge with flow velocities measured at Büz North rock glacier of 15-43 m/hour (Buchli et al., 2013). Other tracer measurements from the rooting zone to the front of Lazaun rock glacier also produced fast flow velocities of 54-327 m/hour (Krainer and Mostler, 2002). This suggests that meltwater is transported as quick flow over the permafrost table and has low residence times. Kenner et al. (2020) claim that the ALT can be a proxy for water storage in the AL. In fact, Buchli et al. (2013) report that when the ALT was larger, the water took slower flow-paths and the tracer velocities were lower. Figure 56 illustrates how for some years, such as 2019 and 2022, the seasonal acceleration in deformation at Murtèl begins at the end of the spring ZC. Those years had a relatively early increase in ALT, which means that meltwater spent more time in the AL and so likely led to a larger increase in the pore water pressure, causing a faster response in deformation. Wirz et al. (2016) report short surface acceleration events after snowmelt or intense precipitation. So, although the water in the AL has high flow velocities, it can be linked to the near-surface deformation of rock glaciers. However, for most years at Murtèl the seasonal acceleration in deformation is not directly triggered from the increase in meltwater in the AL and has a delay of almost a month.

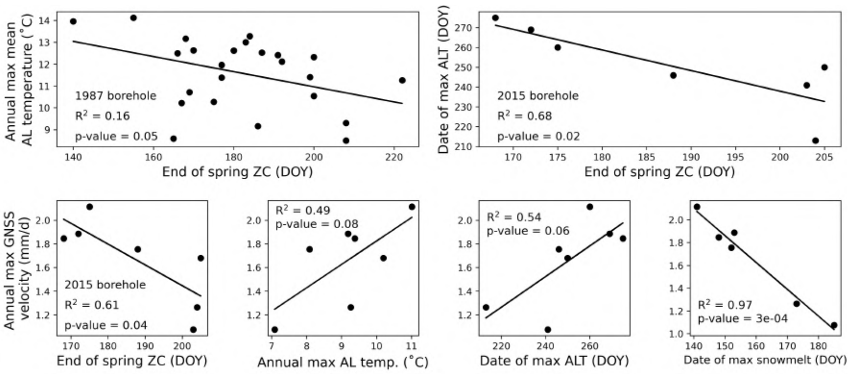

Figure 55: Spring controls on subsurface thermal and deformation conditions. Top-left: day when the spring ZC ends based on 1987 borehole data and the annual maximum mean AL temperature. Top-right: day when the spring ZC ends based on 2015 borehole data and the date when ALT reaches its maximum. Bottom: the end of the spring ZC, annual maximum AL temperature, date when ALT reaches its maximum, and date when snow-melt is the highest as drivers for the annual maximum GNSS deformation rate for years 2016-2022. Data source: PERMOS.

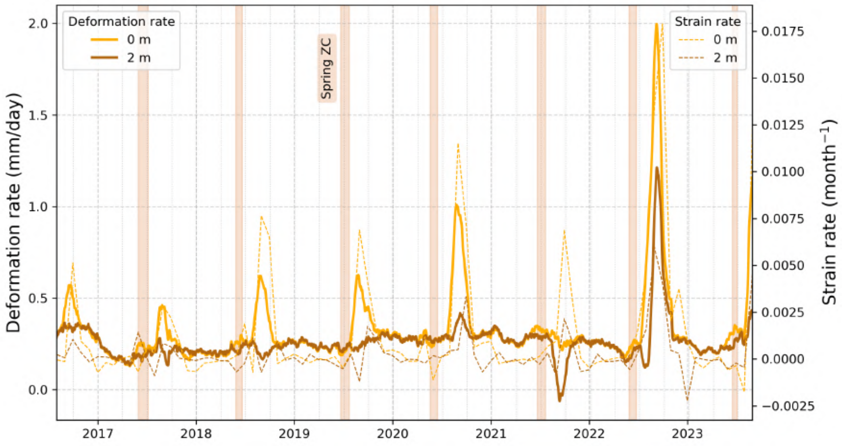

Figure 56: Time series of inclinometer daily deformation and strain rates at the surface and 2 m, spring ZC periods are highlighted. Data source: PERMOS.

Spring meltwater is not restricted to influencing pore water pressure in the AL, but may also penetrate deeper into the permafrost body of a rock glacier. There have been observations of liquid water below the AL in rock glaciers that support this. During the boreholes drilled in the year 2000 at Murtèl rock glacier pressurized water was observed flowing out of the borehole from depths around 3-4 m, but also from 20 m or even over 40 m (L. Arenson et al., 2002). In the 2015 borehole campaign at Murtèl, the same phenomenon was observed when drilling at 31.6 - 32.4 m, which is below the shear zone where large air voids are found. At Lazaun rock glacier the outflow stream water from the rock glacier tongue was measured to have a temperature of 1.3°C, suggesting that it was in contact with ice before leaving the rock glacier (Krainer and Mostler, 2002, Krainer et al., 2015). On Schafberg rock glacier, a piezometer was installed and high pore water pressures were measured at depths around the shear zone (Bast et al., 2024). So, there is evidence of liquid water found at depth in rock glaciers where the ice content decreases and debris grain size allows for suitable pore space. Ikeda et al. (2008) claim that since the permafrost temperatures remained constant near 0°C while the deformation rate varied, the internal pore water pressure is the most likely alternative to have modulated the deformation. The water found deeper in a rock glacier cannot be largely derived from the melt of permafrost ice, as it only makes up 2.3% of the total rock glacier discharge (Krainer et al., 2015). Intra-permafrost flow paths may develop in the early warm phase and then eventually freeze toward the end of the warm phase. The paths may be channel-like or a series of conduits through interconnected air voids and cracks. Liquid water can remain present even below freezing temperatures in permafrost if found in fine pore spaces (L. U. Arenson et al., 2022, Phillips et al., 2023, Bast et al., 2024). The stratigraphy of the Murtèl 2015 core described in Section 4.3 includes observations of thin cracks within the debris layers found in the ice-rich core that may act to transport water during the warm phase. All of these of observations show that, at least for some rock glaciers, there may be transient liquid water within the permafrost which is likely to influence the creep via changes in pore water pressure.

### 5.4.3 Summer controls

After the snow cover is gone and most of the AL ground ice is melted, the warm air temperatures drive the ground heat flux that warms the AL and the permafrost below. Around the time of maximum near-surface temperatures is when the maximum ground heat flux through 3.5 m is also observed for most years. The annual maximum $Q_G$ has been steadily increasing over time with years 2022 and 2023 measuring values close to 15 W/m$^2$ (Fig. 52). Mittaz et al. (2000) calculated peak $Q_G$ values of 28 W/m$^2$. The ground heat flux can vary due to advective fluxes, which on Murtèl are reported to be non-negligible based on an energy budget closure calculation by Mittaz et al. (2000). The temporal trend in $Q_G$ aligns with that of the ALT outlined in Section 4.2.1. In fact, the ALT is strongly coupled with the warm phase thermal conditions. Figure 58 shows that for both the 1987 and 2015 borehole data periods there are significant positive correlations between the warm phase maximum $Q_G$, annual maximum TTOP, annual maximum AL mean temperature, and the ALT. The thermal state of the AL is then correlated with deformation variables. The ALT, the AL mean temperature, the TTOP and the $Q_G$ at 3.5 m all have positive correlations with the annual maximum surface deformation rate (Fig. 57). For the annual maximum GNSS deformation rate, the ALT is not a significant control; however, the warm phase duration does have a significant correlation (p-value = 0.01). Generally, the thermal regime of the AL is observed to have a strong impact on the magnitude of surface velocity peaks.

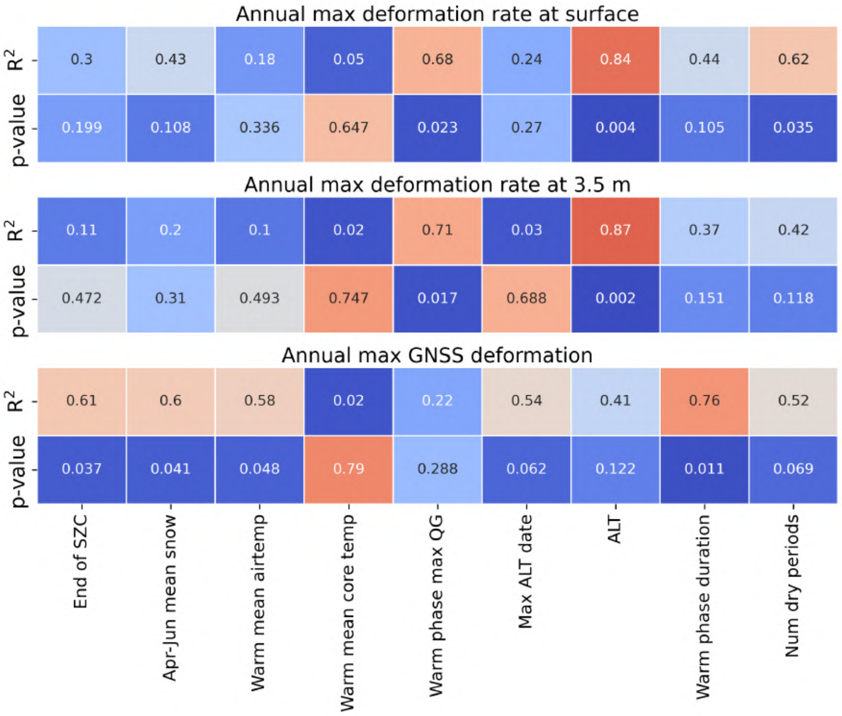

Figure 57: Linear regression matrices for the selected driving annual variables and three deformation response variables: annual maximum deformation rate measured at the top of the 2015 borehole inclinometer (top), annual maximum deformation rate at 3.5 m from 2015 borehle (middle), annual maximum GNSS deformation rate (bottom). Data source: PERMOS, PermaSense and MeteoSwiss.

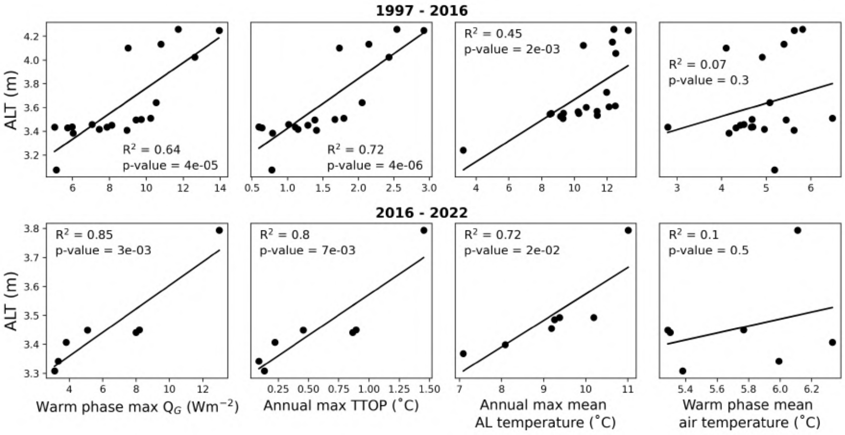

Figure 58: Linear regression for the thermal drivers of the ALT: warm phase maximum ground heat flux $Q_G$, annual maximum temperature at top of permafrost (TTOP), annual maximum AL mean temperature, warm phase mean air temperature for both the 1997-2016 period from the 1987 borehole (top) and 2016-2022 period from the 2015 borehole (bottom). Data source: PERMOS.

The same thermal variables of the AL, but at a monthly temporal resolution, are used to train a MLR model. Figures 59 and 60 show that both models are statistically significant; however, their performance is limited. The model for predicting the GNSS deformation rate explains about 60% of the variance of the true GNSS deformation rate value for both the training and testing subsets (Fig. 59). The model for predicting the SAA 50 cm deformation rate does not perform as well with only 40% of the variance explained in the training subset and 28% in the testing subset (Fig. 60). The model regression coefficients indicate that out of all driving variables, $Q_G$ was the most important control of surface deformation on a monthly timescale (Table 10). This MLR model supports the claim that the thermal conditions of the AL are relatively indicative of the AL creep. The ground heat flux is a direct indication of the magnitude of heat penetration with depth, which is a driver of temperature gradients and melting of ground ice, both important for surface deformation. This should motivate further incorporation of ground heat flux into rock glacier kinematics studies with available borehole temperature measurements.

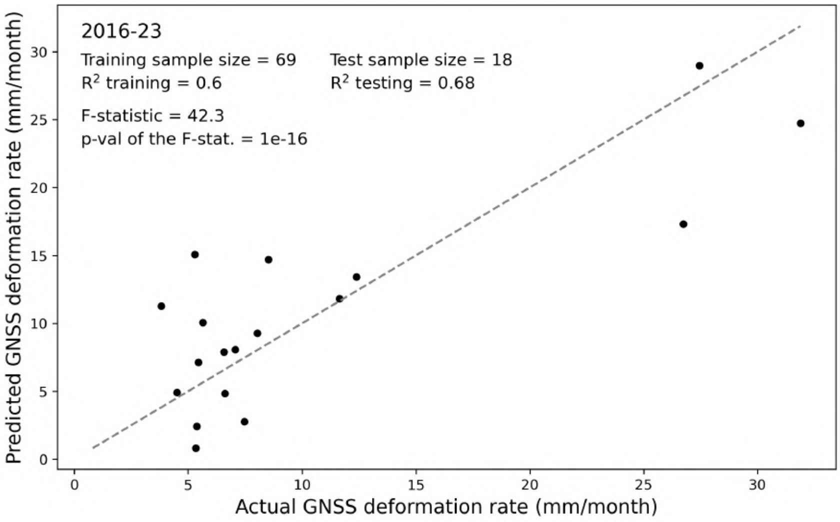

Figure 59: MLR model results from the testing data subset using the monthly-averaged air and surface temperature, AL mean temperature, and $Q_G$ at 3.5 m depth as drivers of the GNSS deformation rate. Grey dashed line is a 1:1 line for scale. Data source: PERMOS and PermaSense.

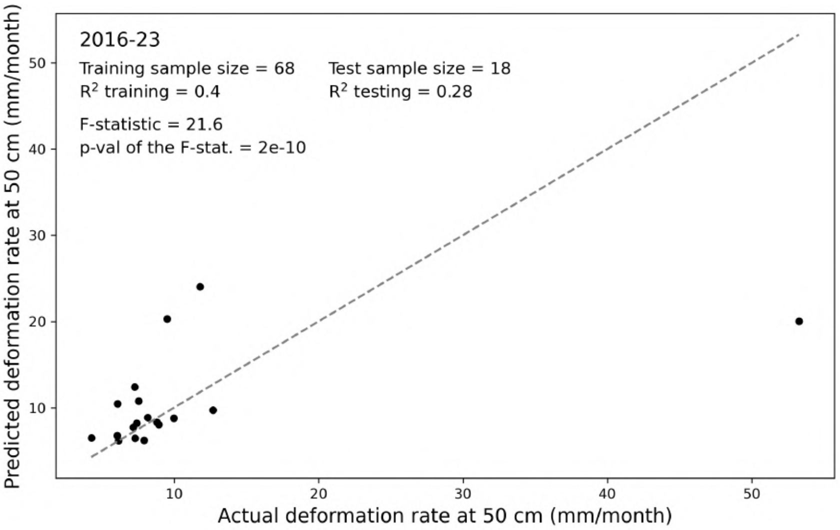

Figure 60: MLR model results from the testing data subset using the monthly-averaged air and surface temperature, AL mean temperature, and $Q_G$ at 3.5 m depth as drivers of the SAA 50 cm deformation rate. Grey dashed line is a 1:1 line for scale. Data source: PERMOS.

Table 10: MLR model regression coefficients for each driving variable and each response variable: SAA at 50 cm and GNSS at a monthly timescale.

| | **SAA** | **GNSS** |
|---|---|---|
| Intercept | 7.43 | 8.52 |
| Air temperature | 0.22 | 0.23 |
| Surface temperature | -0.27 | -0.26 |
| AL mean temperature | -0.15 | 0.44 |
| $Q_G$ at 3.5 m | 2.30 | 2.88 |

The process behind the link between AL thermal conditions and surface deformation is unclear. The AL should not contain much ice to experience temperature-sensitive creep. Amschwand, Tschan, et al. (2024) highlight that a lot of the percolating meltwater in the AL actually refreezes during the early warm phase. This could be a source of ground ice at the bottom of the AL that may persist past the spring ZC. Approximately twice as much ground ice melt was observed during the summer heatwave of 2022 compared to the cooler summer of 2021 (Amschwand, Tschan, et al., 2024). So, this refrozen ground ice could act to provide more meltwater, especially during the warmer summers. Another plausible process is that a higher $Q_G$ can lead to higher temperatures at the top of the permafrost table (TTOP) and increase the liquid water content found there, which in turn acts to lubricate the bottom of the AL and add a sliding component to the surface deformation. Given the very large strain rates observed by the inclinometer near the bottom of the AL, this possibility should not be ignored. The time delay between when various temperature signals reach their annual maximum and when deformation rates reach their maximum is also interesting to consider in terms of process understanding. The average delay between the maximum air temperature and the maximum annual surface GNSS deformation rate is 15 days (Appendix 8.4). The average time lag between the maximum GST from 2018-22 to the maximum annual surface SAA deformation rate is 8 days, whereas for GNSS it is longer. Years with a high maximum GST also experience a high maximum GNSS deformation rate (Fig. 61). For the two years 2020 and 2022 with larger magnitudes of peak velocity, the time delay from peak GST is the shortest. These are relatively short time delays which again support the claim that the near-surface thermal conditions are important for surface deformation. The time lag for temperature maxima to occur from the surface to 10 m depth is 5 months, which is much longer than a few days. Mühll and Haeberli (1990) also found that it took 6 months from when the annual maximum temperature occurred at the surface versus when it occurred at 10 m depth. The much longer temperature penetration time lag relative to the surface temperature to the deformation time lag confirms that most of the seasonal acceleration happens near the surface. Although of the long delay for temperature penetration with depth, still the warm phase mean ice-core temperature is found to be strongly correlated with the deformation rate at 10 m at longer timescales. This relation can be seen in Figure 62 which illustrates how during the period of warming permafrost from 2019 to 2021 the deformation rate at the same depth also increases steadily. Then, excluding the unique 2021 and 2022 deformation events, a de-

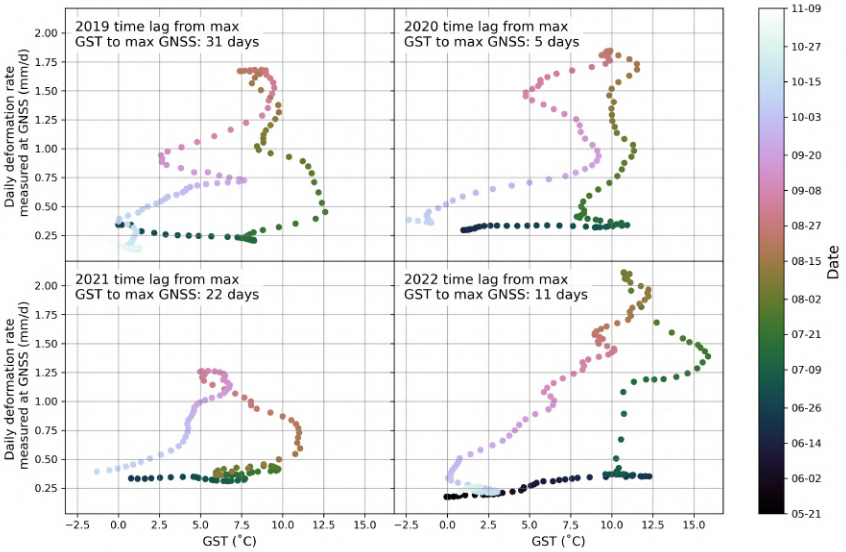

Figure 61: Relationship between warm phase daily GST and GNSS deformation rate for years 2019 to 2022 divided in each subplot. Data source: PERMOS and PermaSense.

creasing trend in the deformation aligns with the decreasing trend in temperature at 10 m from 2021 to 2023. It is important to recall that the ice-rich core temperatures are not driven only by the summer air temperature, but also by the winter snow conditions (Section 5.4.1). So, at short seasonal timescales, the summer thermal near-surface conditions play an important role in determining surface deformation, while at longer interannual timescales the thermal processes also influence ice-core deformation.

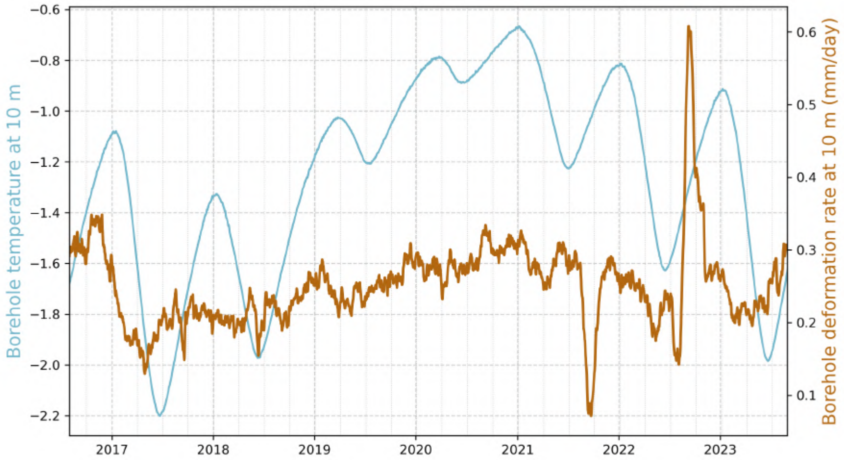

Figure 62: Comparison of daily borehole temperature and deformation rate at 10 m depth from the 2015 borehole at Murtèl rock glacier. Data source: PERMOS.

At three rock glaciers in the Mattertal valley in Switzerland, short peaks in surface deformation during the snow-free period were observed to occur almost always shortly after a strong precipitation event of more than 10 mm/day (Wirz et al., 2016). In contrast, analysis of *in-situ* rainfall data at Murtè showed that rainfall before peak surface deformation rates was not particularly strong. However, the number of dry periods, defined by at least 5 consecutive dry days, has a significant positive correlation with the annual maximum surface deformation measured by the inclinometer (p-value = 0.04) and a strong positive correlation with the annual maximum GNSS velocity (p-value = 0.07) (Fig. 57). So, rainfall does not influence deformation rates on the short term at Murtèl, but rather at a season-long scale. The possible reason for this is that a generally drier warm phase reduces the evaporative cooling from rainwater in the AL which then results in greater $Q_G$ which, as discussed, leads to higher surface deformation (Amschwand, Wicky, et al., 2024).

## 5.5 Comparison of surface deformation measurements

Most of the annual rock glacier kinematic data come from GNSS stations, aerial photogrammetry, or geodetic techniques. Murtèl has the unique situation of having a GNSS station, geodetic measurements, and a SAA borehole inclinometer, which are all able to measure surface deformation at various timescales. First, these different instruments will be compared on an annual timescale. Methods such as geodetic measurements require annual field surveys, usually carried out toward the end of August. The resulting measured annual surface displacement is found to be very sensitive to when exactly these field surveys are done (Fig. 63). The daily deformation data series from the GNSS and SAA show that peak deformation rates are usually observed during the beginning of September and can last until the middle of October. So, by conducting geodetic surveys at the end of August, it is likely that only part or none of the annual deformation peak will be captured. This can be seen in Figure 63 when the vertical dashed-lines, representing the date of maximum daily deformation rate, lie on or after the right end of the annual survey step. For example, the large 2017-18 geodetic deformation rate is caused by the measurement including both parts of the 2017 peak and the 2018 peak, because the previous 2017 survey date did not contain all the warm phase acceleration (Fig. 63). The end of September is found to be the most appropriate field survey time to ensure that most of the seasonal peak in surface deformation is measured (Fig. 63). There is not much annual displacement difference if the survey dates are done at the end of September or the middle of October (Appendix 8.5). The timing of field surveys should be adjusted accordingly, within the limits of safety and practical considerations, such as the onset of snow cover. However, even when a survey captures well only the desired seasonal acceleration of that year, the measured annual displacement can still be lower than that measured by the GNSS or the borehole (Fig. 63). In addition, when the annual GNSS and SAA displacements are computed at the end of September, the values still differ by approximately 5 cm/year. This would suggest that there may be spatial heterogeneity in surface deformation even when the three measurement stations on Murtèl are within a few meters of each other. The surface of Murtèl is composed especially of coarse blocks that are large enough to tilt and tumble independently of the general rock glacier creep. The GNSS station is mounted on a few meters large boulder which is also the same as where the geodetic marker is found, and this boulder may behave differently from area surrounding the top of the borehole.

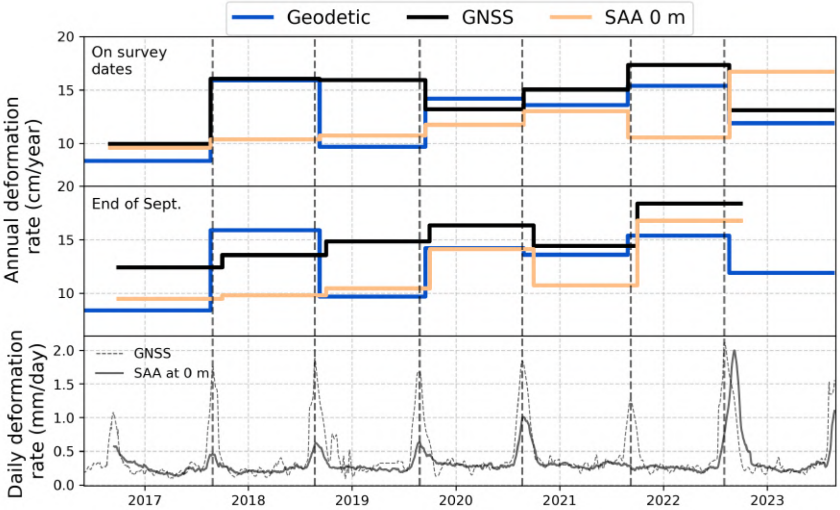

Figure 63: Annual deformation rates measured at geodetic station (COR_021) closest to borehole, GNSS station and uppermost sensor of borehole. Rates are calculated based on the geodetic survey dates (top) and on the end of September (middle). The daily deformation rate measured at the top of the borehole and at the GNSS station is shown, the timing of the annual maximum daily deformation rate is the vertical dashed line (bottom). Data source: PERMOS and PermaSense.

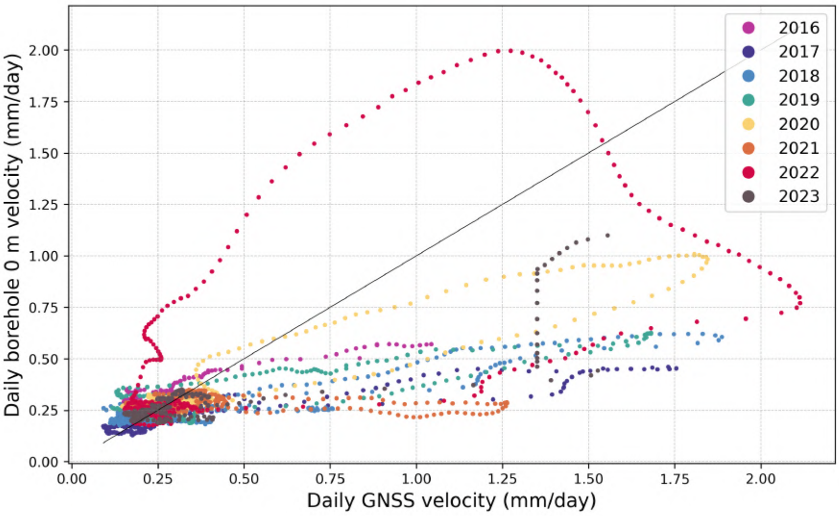

Figure 64: Comparison of the daily deformation rate measured by the GNSS station and the borehole SAA inclinometer at the surface of Murtèl rock glacier. Black line is a one to one line for scale. Data source: PERMOS and PermaSense.

The difference between various measurement methods can also be observed at shorter time scales. Both the GNSS station and the SAA inclinometer can record data at a daily temporal resolution, so these two are now compared. First, for most years, there is a large magnitude difference in the maximum daily deformation rate during the seasonal peaks between the GNSS and SAA measurements. Figure 64 illustrates how for most years except 2022 the maximum daily deformation rate measured by the GNSS is about 55% to 133% higher than that measured by the top of the SAA inclinometer. During the cold phase, when most of the deformation occurs in the shear zone, the GNSS and top of SAA measurements match relatively well. As already mentioned, the boulder onto which the GNSS station is mounted cannot be fully assumed to be well anchored to the rest of the AL and may experience extra rotational movement, adding another displacement term to the general translational movement. Figure 65 shows that indeed during every seasonal peak in deformation the tilt of the GNSS station always decreases by about $0.1^{\circ}$ to $1^{\circ}$. The timing of the seasonal acceleration measured by the GNSS and SAA matches well for most years except for 2022 when the GNSS reaches its peak around two weeks before the SAA does (Fig. 65). This is also visualized in the double-lobed loop for the 2022 points in Figure 64. The explanation for this will be explored in the next section, discussing the special deformation events in the borehole for 2021 and 2022. This GNSS-SAA difference is compounded when comparing the cumulative displacement measured over the entire period (Fig. 66). The GNSS cumulative deformation is about 23-25 cm larger than the SAA and geodetic total surface displacement and has an annual deformation rate of 15 cm/year. Figure 66 shows how over the seven years of measurements the cumulative deformation measured at the top of the borehole and at the nearby geodetic marker differs by only 2 cm. Each had an average annual deformation rate of 11.9 cm/year. The lower total SAA surface displacement compared to the GNSS is also partly caused by the lack of a seasonal peak in 2021, while the GNSS still measured a peak in deformation.

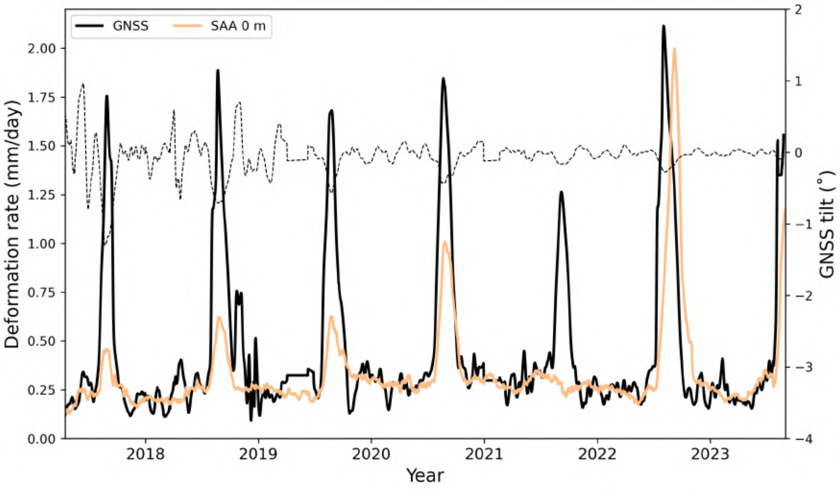

Figure 65: Time series comparison of the daily deformation rate measured at the surface of the SAA inclinometer in the 2015 borehole and that by the GNSS station. The inclination (tilt) angle measured by the GNSS station is also plotted. Data source: PERMOS and PermaSense.

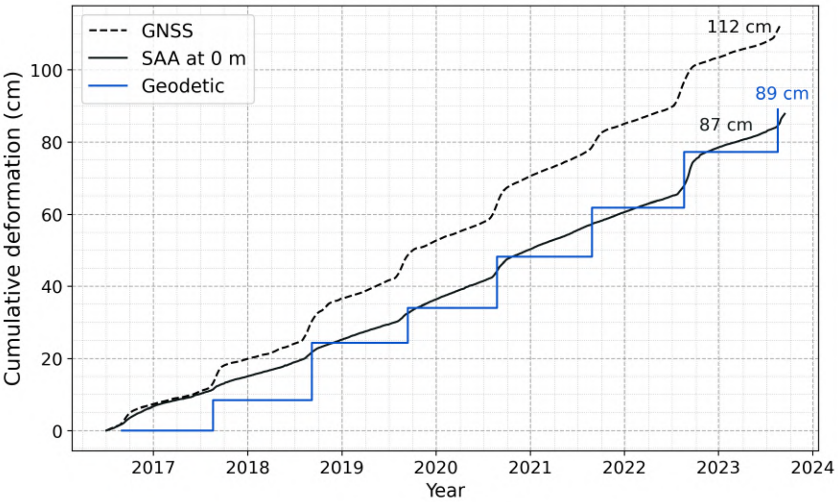

Figure 66: Cumulative deformation time series for the three different approaches available to measure surface deformation at Murtèl rock glacier (GNSS, borehole SAA, and geodetic). The total cumulative deformation measured by each at the end of the period is shown. Data source: PERMOS and PermaSense.

## 5.6 Special borehole deformation events

### 5.6.1 2021 deceleration

The first unique borehole deformation event occurs in the warm phase of 2021 when backward movement is measured for about two weeks in September at depths of 2 to 5 m (Fig. 40). The source of this deceleration must derive from the depths around the bottom of the AL because that is where the highest backward movement is measured. The deceleration signal is measured down to around 15 m; however, below that the shear zone deformation is not affected. During the event, the negative velocities around the bottom of the AL and the unchanged velocities at the shear zone mean that in the ice-rich core the deformation rate actually increases with depth. Buchli et al. (2018) also observed a slight increase in deformation rate with depth in the core at Büz North rock glacier and described it as rotational movement. This is the first time negative velocities have been observed with rock glacier borehole deformation, and thus only a few inferred reasons can be hypothesized. Some blocks around the borehole near the bottom of the AL may have become interlocked with each other. This in combination with the added stress from the large change in direction of horizontal movement and the rigidity of the inclinometer segments may have caused a backward bend near the bottom of the AL. The year 2021 has a very snow-rich preceding winter and also a cool, short, and wet warm phase. Given these conditions, it is plausible that not all the ground ice in the AL may have melted during the spring ZC. This in turn may support the idea of the interlocking of blocks frozen to each other near the AL bottom partially initiating the backward bend at those same depths. Interestingly, the GNSS station does measure a seasonal acceleration in 2021. The 2021 GNSS velocity peak of about 1.25 mm/day is the smallest in magnitude from the 2016-23 period (Fig. 65). It can be that this is the difference in deformation rate between the GNSS and the SAA seen in the other years, which usually is approximately 1 mm/day. Therefore, the GNSS station in summer 2021 is likely to be measuring a signal unique to its boulder caused by shallow subsurface accelerations and not by deformation deeper in the rock glacier. In general, it is difficult to say what caused the backward movement of the 2 - 5 m segments of the inclinometer, but it is likely to involve the processes regarding the interlocking of blocks combined with the added stress from the drastic change in surface movement direction and the continued creeping at depth.

### 5.6.2 2022 acceleration

The second unique borehole deformation event occurred in the warm phase of 2022. The largest magnitudes of AL and ice-rich core deformation from the 2016-23 period were measured during this time. It is the only case where borehole deformation was able to measure a seasonal acceleration at depths even greater than 10 m. Similarly to the 2021 event, the processes responsible for this novel signal in rock glacier borehole deformation are difficult to interpret. The following interpretations of the event are limited to conjectures based on current understanding of the inclinometer dynamics. The first phase of this event starts with the inclinometer segments in the top 2 m accelerating already in early July, while the ones below to around 10-15 m began to decelerate. The most pronounced deceleration occurred around the bottom of the AL, similar to the event in 2021. There is no backward movement, but the segments at around 2.5 - 3.5 m move only around 0.2 mm/day. This occurs during the first change of 2D direction of movement. During the second phase of this event, all segments start to drastically accelerate down to about 15 m during the second change of 2D movement of direction (Fig. 39). It is also the only year where a detectable change of 2D movement was observed down to 8 m. This might suggest that the deformation measurements of the inclinometer are highly sensitive to changes in the direction of horizontal movement. The most pronounced acceleration occurs at 2.5 - 3.5 m where it is likely that a slip event occurred from some blocks that had become interlocked given the antecedent deceleration (Jansen and Hergarten, 2006). The acceleration is likely to also have originated at around these depths near the bottom of the AL. The ALT reached nearly 4 meters this year, indicating increased ground ice melt, which could have contributed to higher pore water pressure and triggered the slip event. In addition to this very large AL deformation, the ice-rich core deformation also reached its highest out of the 2016-23 period. The warm phase of 2022 was the second hottest on record since 1994. It was also the driest and longest warm phase of the 2016-23 period. The dry warm phase AL experienced low turbulent fluxes to export the incoming radiation, which led to a very high ground heat flux through the AL and into the ice-rich core. The spring ZC had the second earliest ending, which also provided with more snow-free time for the solar radiation to penetrate into the core. This high input of ground heat flux is likely to have contributed to the especially high ice-rich core deformation in combination with the potential of stick-slip events.

## 5.7 Role of internal structure for deformation

The almost eight-year-long deformation data from the borehole provides a robust deformation profile to compare with the detailed stratigraphy description. The following discussion between strain rates and stratigraphy is based on Figure 67. The top few meters of the AL without summer ice content show very high strain rates, suggesting low shear strength. L. U. Arenson and Springman (2005) found that the maximum shear strength in rock glacier cores occurs with very low ice contents or with pure ice. The ice-poor cores with high shear strength measured by L. U. Arenson and Springman (2005) consisted mainly of silty sand debris, which contrasts with the ice-poor but coarse-blocky AL at Murtèl. So, in addition to the debris content, the grain size is also important in modulating the shear strength of rock glacier material. In the AL the large decrease in strain rate with depth stops at around 2.5 m, which is where the ice content was observed to increase during the drilling operation. Below the AL to about 7 m the strain rate is roughly constant as the ice content remains close to 100%. Between 7-9 m there is an inversion of deformation with depth as the strain rate decreases until about 8.8 m where a stiff rock layer holds back the inclinometer segment while above and below the segments experience higher displacement. Then, from 9 - 15.5 m the core is made up mainly of pure ice and again the strain rate is uniform with depth. From 15.5 - 19.5 m the strain rate begins to slowly decrease with depth. This is also where the debris content increases, which Goughnour and Andersland (1968) found to increase the compressive strength of the material. Further down between 19.5 and 21 m the strain rate increases as the ice grains become larger causing lower shear strength. There are a few bands of fine sediment at these depths, but not enough to fully explain the increase in strain rate. Then, from 21- 25.5 m the strain rate is roughly constant even though the debris content from 22.5 m to 25 m clearly is increasing. In these last few meters, the stratigraphy alone cannot fully explain the strain rate pattern with depth.

The shear zone spans from 26 to 28.5 m, where the highest strain rates are found throughout the borehole. At the top of the shear zone there are a few solid rock layers with below ice-rich debris. From 27 - 28.5 m the fine sediment concentration increases drastically, but still with the pores being fully saturated with ice. This layer of frozen fine debris experiences high strain rates. There is some uncertainty in the literature on the rheological behavior of debris-rich ice. Moore (2014) report that when the debris content exceeds 42% the shear strength begins to rapidly increase. On the other hand, Bucki and Echelmeyer (2004) found that debris-rich ice is seven times softer than pure ice as interstitial water between the fine particles can allow slip and reduce the material's viscosity. Fine sediment can hold liquid interstitial water even at temperatures below the freezing point, as low ERT resistivity was observed for fine-grain ice-saturated layers in rock glaciers (Emmert and Kneisel, 2017). The rheology of frozen fine sediment requires further quantitative investigation to better determine its mechanical properties in the context of rock glaciers. The peak strain rate is observed where the stratigraphy changes from ice-saturated debris to ice-poor debris. The high degree of anisotropy around the shear zone causes a high strain localization, which explains the high deformation rates. Below the shear zone, it is likely that the debris reaches its maximum packing density and the shear strength increases (Moore, 2014). In general, the stratigraphy of Murtèl rock glacier can explain the vertical profile in the strain rate, except for some depths around the shear zone.

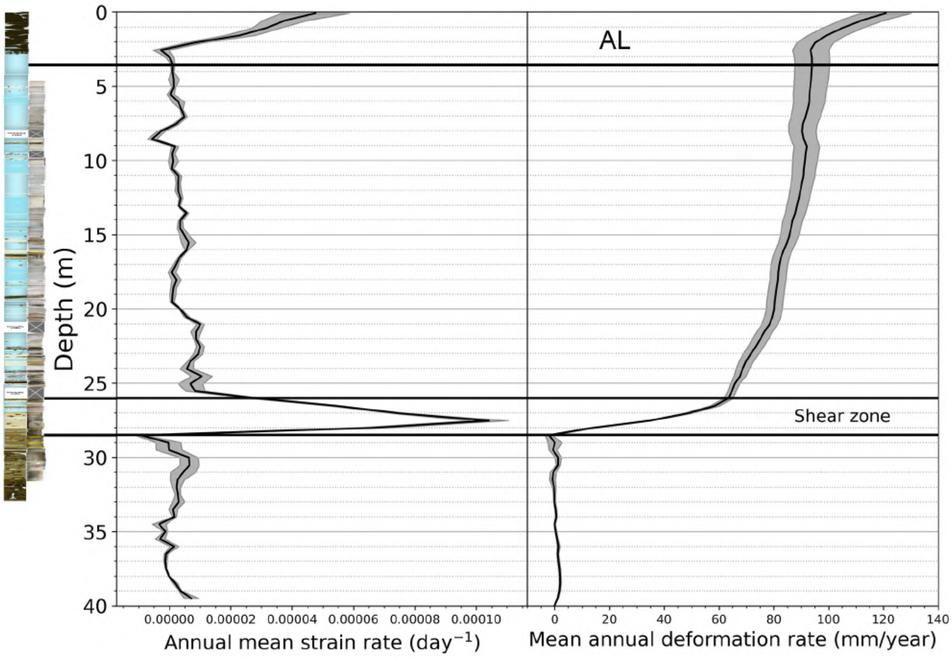

Figure 67: The average strain rate and deformation profiles across all years from the 2015 Murtèl borehole with its corresponding stratigraphy. Data source: PERMOS.

## 5.8 Limitations

### 5.8.1 Methodological limitations

The weather data used from the *in-situ* PERMOS station is reliable following the accuracy of standard instruments. One consideration is that the snow height measurements from the ultrasonic transducer were used to calculate the snowmelt energy based on the decrease in height. However, a reduction in snow height can also be caused by snow compaction as it undergoes metamorphism. The snowmelt energy was only calculated for days when the air temperature was greater than -3°C which should help reduce the potential of snowmelt overestimation. Furthermore, the lack of liquid precipitation data introduces some uncertainties, as the regression used to extend the PERMA-XT precipitation back in time by extrapolating the Piz Corvatsch precipitation is moderately strong ($R^2 = 0.77$). Its main weakness lies in the days when one station measures precipitation, but the other does not (Fig. 68). There are more days when the PERMA-XT rain gauge is not measuring precipitation, while the Piz Corvatsch one is. The Piz Corvatsch gauge is a standard MeteoSwiss heated rain gauge capable of measuring solid precipitation. As Piz Corvatsch is a few hundred meters higher elevation than the PERMA-XT station, it is possible that even during the warm phase there was snowfall that was not measured on the rock glacier. These data points are skewing the regression line so that it underestimates the precipitation for the wetter days. The precipitation data is mainly found to be relevant for calculating the number of dry periods during the warm phase, so the implication of its uncertainty is limited. The method developed to extract ALT from the borehole temperatures also has limitations. Performing linear interpolation between neighboring sensors to find the 0°C isotherms may not be very accurate, as it is likely that for some days the temperature profile with depth can be non-linear. However, this is still more precise than being limited to choosing the depth with an available thermistor that is closest to 0°C as the ALT. The annual maximum depth of the 0°C isotherm is taken to be the ALT. This was used instead of the mean 0°C isotherm depth because of the time series of 0°C isotherm depths was not always continuous during the warm phase. However, the 0°C isotherm for some years exhibits short drops to deeper depths that may not be representative of the ALT when the maximum depth is taken. This is what is observed to cause

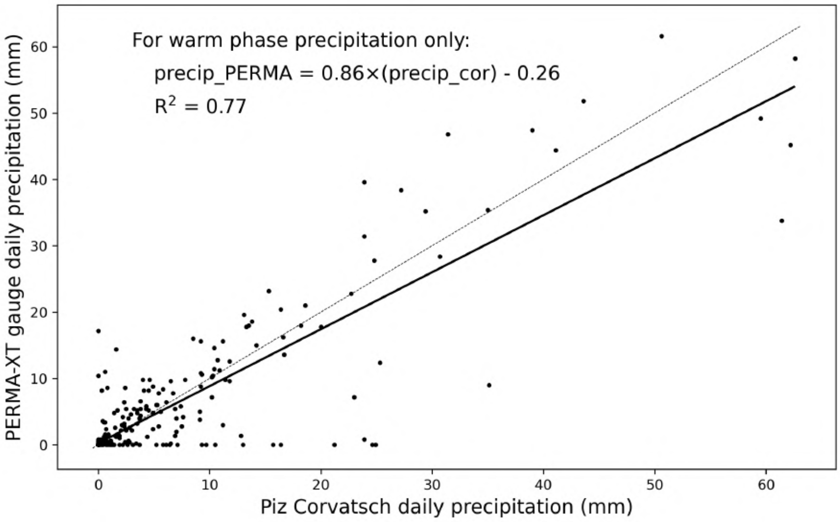

Figure 68: Regression between the MeteoSwiss Piz Corvatsch warm phase precipitation and the PERMA-XT warm phase precipitation at Murtèl rock glacier from 2020 to 2023. The dotted line shows a 1:1 line. Data source: PERMA-XT and MeteoSwiss.

the increase in ALT in 2022 to 2023 and should be addressed with caution.

The SAA inclinometer borehole deformation measurements provide novel and insightful results; however, they also come with some uncertainty that is difficult to quantify. The proprietary Measurand software is required to convert the raw inclination data to the 3D displacement data. Buchli et al. (2016) report that based on the Measurand software version used they find up to 30% differences in deformation magnitude from the SAA measurements. This underlines that this data processing step may introduce a substantial amount of uncertainty in the data. The Measurand software is not open-source and, therefore, it is not possible to understand what the data processing steps are. It would be beneficial to have more metadata from the manufacturer regarding the raw data which might help in understanding how the 3D displacement values are computed. They provide information that the instrument has an accuracy of $\pm 1.5$ mm in the horizontal direction over at least 1.5 years, which is difficult to interpret. The deformation measured below the shear zone can be used to make a gross estimate of the uncertainty as in theory at those depths the deformation should be zero. The segments below the shear zone measure at most 2 cm of deformation over the entire period of about 7.25 years, and this corresponds to an uncertainty of 0.3 cm/year. This is not sufficient to explain the strange events, such as the negative deformation rates, in 2021, which might be a side effect of the way the raw data is processed. The correlation analysis in Section 5.4 shows that there are more significant correlations between driving variables and the GNSS maximum deformation rate than with the SAA maximum deformation rate on the surface. This also may hint at the fact that the magnitude in the peaks of deformation rate comes with hidden uncertainty.

The reliability of the depth of the inclinometer sensors after more than 7 years can also be questioned. The top of the inclinometer is anchored at the surface; however, it cannot be directly known whether the bottom of the chain has become frozen to the bed or is free to be uplifted as the rock glacier deforms. The segments that measure the highest deformation rates in the lower shear zone remain those at the same depths for the whole period, suggesting that there should be no inclinometer lift from the bottom. The top 2.5 m of the inclinometer experiences the second highest strain rates, and as it bends the vertical joint-to-joint distance of the segments becomes smaller than the original 50 cm. Over time, this means that a sensor originally 2.5 m below the surface is now closer to the surface (Fig. 69). However, there is no way of proving whether this is happening, since the vertical displacement measured by the SAA sensors is relative to their starting position and not the sloping surface. As the inclinometer chain bends over time, its entire length should stretch, unless there is significant thinning of the permafrost body. Using the geometry of the final inclination of the chain parts in each layer, it can be estimated that the entire chain should have stretched by 10 cm over the entire period (Appendix 8.6). The Measurand manufacturer of the SAA chain does not provide any direct specification about the chain's ability to stretch; however, they report two different segment joint diameters one in case of compression and one in case of extension, which suggests that extension may be possible. Based on a similar geometric calculation, the estimated extension of the inclinometer chain for the deformation profile of Furggwanghorn rock glacier is 20-80 cm (Buchli et al., 2018). After this point, the inclinometer stopped working, which could suggest that there may be a limit of extension that the inclinometer can withstand before failure. For future studies that wish to analyze the borehole deformation data in more detail, it is important to acknowledge these unknowns about the uncertainty of deformation and vertical position of the inclinometer sensors.

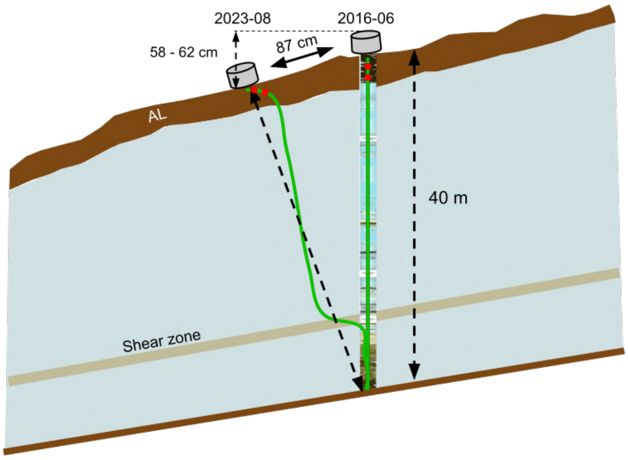

Figure 69: Drawing of initial position of the SAA inclinometer (green, right) in 2016-06 and final position in 2023-08 (green, left) after 87 cm of horizontal displacement at the surface and a vertical displacement meausred by the GNSS and geodetic stations. The two red dots on each inclinometer line represent the location of two example sensors. The sketch is not drawn to scale.

### 5.8.2 Limitations in process understanding

Multiple studies have observed a large spatial heterogeneity in surface velocity within a single rock glacier. This is often the case for rock glaciers with multiple lobes that experience different seasonal accelerations in velocity (Kääb et al., 1997; Kääb et al., 1998; Fey and Krainer, 2020; Gärtner-Roer et al., 2022; Crivelli, 2024). The highest surface velocity of a rock glacier is not always located near its center. Some glaciers may even experience localized destabilization events that lead to very high velocities only in certain parts of the rock glacier (Delaloye et al., 2010). Photogrammetry studies from Murtèl rock glacier show that the surface velocity varies by 10 cm/year longitudinally, with the highest values near the steeper section of the rooting zone

(Kääb et al., 1998). The location of the boreholes on the lower part of the rock glacier represents the lower end of surface velocities of Murtèl rock glacier. So, it can be said that the velocities measured near the borehole are representative of the lower part of Murtèl rock glacier, but not of the rooting zone and the margins. In addition to heterogeneity within a single rock glacier, different rock glaciers can vary in terms of the processes that control deformation. Murtèl rock glacier has especially high ice content compared to other rock glaciers with data on their internal structure. For example, Schafberg rock glacier only has 5 m with ice content up to 80%, otherwise it stays only at around 30-40% (Kenner et al., 2020). A different ice content affects the role of temperature in deformation and how meltwater percolates through the rock glacier core. Rock glaciers with warm or cold permafrost may also experience different controlling processes. For warm permafrost, the structure of the ice crystals becomes more heterogeneous, and this can form preferential flow paths for meltwater to percolate, increasing the dominance of hydrological controls (Bast et al., 2024). The depth of the shear zone varies between rock glaciers, which can also affect the seasonal contribution of shear zone deformation. Schafberg rock glacier has a shallower shear zone compared to Murtèl and experiences seasonal fluctuations in shear zone deformation. The dominance of hydrological or thermal factors in deformation depends on the internal structure of the rock glacier. These considerations likely limit the generalization of the processes explored in Section 5.4 to Murtèl rock glacier, but promote the value of collecting data on the internal structure of rock glaciers.

# 6 Conclusion

The slow-moving Murtèl rock glacier is now host of two unique borehole datasets. First, the 1987 borehole long-term temperature record, which shows that, for an ice-rich permafrost landform, Murtèl rock glacier is warming at a rapid rate of 0.3°C/year. The ALT of Murtèl rock glacier has been stable at 3.5 m for almost 30 years, and only in the last two years it began showing signs of deepening. The borehole temperature record also shows how, when extracting the ZC, the depth from which the temperature series is taken should be chosen carefully. The second more recent borehole drilled in 2015 has the longest available record of rock glacier borehole deformation data with more than seven years of data. This new borehole provided data which allowed for the stratigraphy record from the 1987 borehole to be updated. From around 3.5 to 26 m the ice-rich core is found with only a few thin layers of debris. The shear zone is located at 26 to 28.5 m in a transition area from ice-rich to ice-poor debris below which no ice is found.

The borehole inclinometer, for the first time, is able to resolve seasonal deformation patterns with depth in a rock glacier. The annual acceleration that occurs in the late summer is found to be limited to the AL. The strain rates in the AL are very similar to those observed in the shear zone, creating a secondary shear zone at the permafrost table. The year 2021 showed a unique deformation profile with negative deformation rates around the bottom of the AL during the warm phase. The year 2022 stands out with the largest seasonal acceleration, which was measured down to 15 m. The shear zone depth has decreased from 28-31 m in 1987-95 to 26-28.5 m in 2016-23. The shear zone deformation, compared to the ice-rich core and AL, has very small interannual variability, but it contributes to 56% of surface deformation, which is similar to what L. Arenson et al. (2002) found. The shear zone can be assumed to be at depths with drastic changes in the stratigraphy.

The summer thermal conditions appear to be the dominant driver of the magnitude of the seasonal deformation peak, and not the hydrological factors. A MLR model trained on variables describing the thermal state of the AL was able to predict the monthly surface deformation. Unlike previous studies reporting a very fast response in surface deformation during the seasonal melt, Murtèl rock glacier has an average time delay from the end of the spring ZC to the start of the surface acceleration of one month. The timing of the seasonal melt of snow and AL ice is more important to determine the duration of the warm phase with positive ground heat flux. Future investigations should consider installing piezometers to directly measure water pressure with depth in a rock glacier borehole to provide a better understanding of the kinematic role of seasonal meltwater. In the summer of 2024 an inclinometer was installed in the new borehole on Muragl rock glacier in the Engadin. Future borehole deformation data should be analyzed using an approach motivated by this thesis. In particular, acknowledging the usefulness of calculating the strain rate with depth, identifying layers with unique deformation characteristics, and thereafter computing layer-specific deformation rates.

The daily surface deformation data at Murtèl suggests that annual geodetic surveys should be carried out in late September to mid-October to ensure capturing most of the seasonal peak. However, over periods of multiple years, the total geodetic displacement measured differs only by 2 cm from the total displacement measured at the top of the borehole inclinometer. Other active rock glaciers with only surface deformation measurements should consider the possibility that the measured seasonal variations in deformation are largely limited to AL-only deformation. The link between the MAAT and the annual deformation rate becomes very weak for depths below the AL for Murtèl. The RGV of Murtèl is determined to not be suitable as an ECV parameter on its own. This emphasizes how RGV as an ECV should be used primarily on a regional scale and not for individual rock glaciers. The extent to which surface deformation is representative of deformation at depth will depend on the internal structure of the rock glacier, such as ice content, debris grain size, and depth of the shear zone. Ultimately, this investigation aims to motivate future projects to install inclinometers in relatively slow-moving rock glaciers to advance the process understanding of rock glacier kinematics and to test whether a given rock glacier is suitable for having its velocity as an ECV parameter.

# 7 References

ALPUG. (2015). Borehole temperature logging system 2015 murtel.

Amschwand, D., Wicky, J., Scherler, M., Hoelzle, M., Krummenacher, B., Haberkorn, A., Kienholz, C., & Gubler, H. (2024). Sub-surface processes and heat fluxes at coarse-blocky murt\'{e}l rock glacier (engadine, eastern swiss alps). *EGUsphere*, *2024*, 1–47. https://doi.org/10.5194/egusphere-2024-172

Amschwand, D., Scherler, M., Hoelzle, M., Krummenacher, B., Haberkorn, A., Kienholz, C., & Gubler, H. (2023, September 29). Surface heat fluxes at coarse-blocky murtèl rock glacier (engadine, eastern swiss alps). https://doi.org/10.5194/egusphere-2023-2109

Amschwand, D., Tschan, S., Scherler, M., Hoelzle, M., Krummenacher, B., Haberkorn, A., Kienholz, C., Aschwanden, L., & Gubler, H. (2024, April 18). On the hydrological significance of rock glaciers: A case study from murtèl rock glacier (engadine, eastern swiss alps) using below-ground energy-flux measurements, ground-ice melt observations and hydrological measurements. https://doi.org/10.5194/egusphere-2024-844

Arenson, L., Hoelzle, M., & Springman, S. (2002). Borehole deformation measurements and internal structure of some rock glaciers in switzerland. *Permafrost and Periglacial Processes*, *13*(2), 117–135. https://doi.org/10.1002/ppp.414

Arenson, L. U., Harrington, J. S., Koenig, C. E. M., & Wainstein, P. A. (2022). Mountain permafrost hydrology—a practical review following studies from the andes. *Geosciences*, *12*(2), 48. https://doi.org/10.3390/geosciences12020048

Arenson, L. U., & Springman, S. M. (2005). Mathematical descriptions for the behaviour of ice-rich frozen soils at temperatures close to 0 °c. *Canadian Geotechnical Journal*, *42*(2), 431–442. https://doi.org/10.1139/t04-109

Barsch, D., & Hell, G. (1976). Photogrammetrische bewegungsmessungen am blockgletscher murtèl i, oberengadin, schweizer alpen. *Zeitschrift für Gletscherkunde und Glazialgeologie*, *11*(2), 111–142.

Bast, A., Kenner, R., & Phillips, M. (2024, February 5). Short-term cooling, drying and deceleration of an ice-rich rock glacier. https://doi.org/10.5194/egusphere-2024-269

Bearzot, F., Garzonio, R., Di Mauro, B., Colombo, R., Cremonese, E., Crosta, G. B., Delaloye, R., Hauck, C., Morra Di Cella, U., Pogliotti, P., Frattini, P., & Rossini, M. (2022). Kinematics of an alpine rock glacier from multi-temporal UAV surveys and GNSS data. *Geomorphology*, *402*, 108116. https://doi.org/10.1016/j.geomorph.2022.108116

Benedict, J. B., Benedict, R. J., & Sanville, D. (1986). Arapaho rock glacier, front range, colorado, u.s.a.: A 25-year resurvey. *Arctic and Alpine Research*, *18*(3), 349–352. https://doi.org/10.1080/00040851.1986.12004096

Biskaborn, B. K., Smith, S. L., Noetzli, J., Matthes, H., Vieira, G., Streletskiy, D. A., Schoeneich, P., Romanovsky, V. E., Lewkowicz, A. G., Abramov, A., Allard, M., Boike, J., Cable, W. L., Christiansen, H. H., Delaloye, R., Diekmann, B., Drozdov, D., Etzelmüller, B., Grosse, G., … Lantuit, H. (2019). Permafrost is warming at a global scale. *Nature Communications*, *10*(1), 264. https://doi.org/10.1038/s41467-018-08240-4

Bolch, T., & Marchenko, S. (2009). Significance of glaciers, rockglaciers and ice-rich permafrost in the northern tien shan as water towers under climate change conditions [Publisher: IHP UNESCO]. https://doi.org/https://doi.org/10.5167/uzh-137250

Brown, W. (1925). A probable fossil glacier. *Journal of Geology*, *33*, 464–66.

Buchli, T., Kos, A., Limpach, P., Merz, K., Zhou, X., & Springman, S. M. (2018). Kinematic investigations on the furggwanghorn rock glacier, switzerland. *Permafrost and Periglacial Processes*, *29*(1), 3–20. https://doi.org/10.1002/ppp.1968

Buchli, T., Laue, J., & Springman, S. M. (2016). Amendments to interpretations of SAAF inclinometer data from the furggwanghorn rock glacier, turtmann valley, switzerland: Results from 2010 to 2012. *Vadose Zone Journal*, *15*(4), 1–3. https://doi.org/10.2136/vzj2015.09.0132

Buchli, T., Merz, K., Zhou, X., Kinzelbach, W., & Springman, S. M. (2013). Characterization and monitoring of the furggwanghorn rock glacier, turtmann valley, switzerland: Results from 2010 to 2012. *Vadose Zone Journal*, *12*(1), 1–15. https://doi.org/10.2136/vzj2012.0067

Bucki, A. K., & Echelmeyer, K. A. (2004). The flow of fireweed rock glacier, alaska, u.s.a. *Journal of Glaciology*, *50*(168), 76–86. https://doi.org/10.3189/172756504781830213

Chaix, A. (1923). Les coulées de blocs du Parc national suisse d'Engadine (Note préliminaire). *Le Globe. Revue genevoise de géographie*, *62*(1), 1–35. https://doi.org/10.3406/globe.1923.5609

Cicoira, A., Beutel, J., Faillettaz, J., & Vieli, A. (2019). Water controls the seasonal rhythm of rock glacier flow. *Earth and Planetary Science Letters*, *528*, 115844. https://doi.org/10.1016/j.epsl.2019.115844

Cicoira, A., Marcer, M., Gärtner-Roer, I., Bodin, X., Arenson, L. U., & Vieli, A. (2021). A general theory of rock glacier creep based on in-situ and remote sensing observations. *Permafrost and Periglacial Processes*, *32*(1), 139–153. https://doi.org/10.1002/ppp.2090

Cicoira, A., Weber, S., Biri, A., Buchli, B., Delaloye, R., Da Forno, R., Gärtner-Roer, I., Gruber, S., Gsell, T., Hasler, A., Lim, R., Limpach, P., Mayoraz, R., Meyer, M., Noetzli, J., Phillips, M., Pointner, E., Raetzo, H., Scapozza, C., … Beutel, J. (2022). In situ observations of the swiss periglacial environment using GNSS instruments. *Earth System Science Data*, *14*(11), 5061–5091. https://doi.org/10.5194/essd-14-5061-2022

Cremonese, E., Gruber, S., Phillips, M., Pogliotti, P., Boeckli, L., Noetzli, J., Suter, C., Bodin, X., Crepaz, A., Kellerer-Pirklbauer, A., Lang, K., Letey, S., Mair, V., Morra Di Cella, U., Ravanel, L., Scapozza, C., Seppi, R., & Zischg, A. (2011). Brief communication: &Quot;an inventory of permafrost evidence for the european alps&quot; *The Cryosphere*, *5*(3), 651–657. https://doi.org/10.5194/tc-5-651-2011

Crivelli, G. (2024). *Seasonal variability of rock glaciers kinematics using GNSS and UAV photogrammetry: Four case studies in the southern swiss alps, canton ticino.* [Doctoral dissertation, University of Zürich].

Cross, W., & Howe, E. (1905). *Geography and general geology of the quadrangle* (No. 120). Silverton Folio, Colorado.

Delaloye, R., Lambiel, C., & Gärtner-Roer, I. (2010). Overview of rock glacier kinematics research in the swiss alps. *Geographica Helvetica*, *65*(2), 135–145. https://doi.org/10.5194/gh-65-135-2010

Delaloye, R., Pellet, C., & Vivero, S. (2021). *Rock glacier inventories and kinematics (RGIK).* GCOS-CH. https://www.meteoswiss.admin.ch/dam/jcr:65b55832-88d6-4929-821c-64e4f11b4c43/RGIK_Final_report_GCOS-website_v2.1.pdf

Dobiński, W. (2020). Permafrost active layer. *Earth-Science Reviews*, *208*, 103301. https://doi.org/10.1016/j.earscirev.2020.103301

Durisch, F. (2023). *Long-term evolution of different permafrost landforms on the northern slope of piz corvatsch, engadin.* [Doctoral dissertation, University of Zürich].

Emmert, A., & Kneisel, C. (2017). Internal structure of two alpine rock glaciers investigated by quasi-3-d electrical resistivity imaging. *The Cryosphere*, *11*(2), 841–855. https://doi.org/10.5194/tc-11-841-2017

Fey, C., & Krainer, K. (2020). Analyses of UAV and GNSS based flow velocity variations of the rock glacier lazaun (ötztal alps, south tyrol, italy). *Geomorphology*, *365*, 107261. https://doi.org/10.1016/j.geomorph.2020.107261

Frauenfelder, R., & Kääb, A. (2000). Towards a palaeoclimatic model of rock-glacier formation in the swiss alps. *Annals of Glaciology*, *31*, 281–286. https://doi.org/10.3189/172756400781820264

Fukui, K., Sone, T., Strelin, J. A., Torielli, C. A., Mori, J., & Fujii, Y. (2008). Dynamics and GPR stratigraphy of a polar rock glacier on james ross island, antarctic peninsula. *Journal of Glaciology*, *54*(186), 445–451. https://doi.org/10.3189/002214308785836940

Gärtner-Roer, I., Brunner, N., Delaloye, R., Haeberli, W., Kääb, A., & Thee, P. (2022). Glacier–permafrost relations in a high-mountain environment: 5 decades of kinematic monitoring at the gruben site, swiss alps. *The Cryosphere*, *16*(5), 2083–2101. https://doi.org/10.5194/tc-16-2083-2022

Glen, J. (1955). The creep of polycrystalline ice. *Proceedings of the Royal Society of London. Series A. Mathematical and Physical Sciences*, *228*(1175), 519–538. https://doi.org/10.1098/rspa.1955.0066

Goughnour, R. R., & Andersland, O. B. (1968). Mechanical properties of a sand-ice system. *Journal of the Soil Mechanics and Foundations Division*, *94*(4), 923–950. https://doi.org/10.1061/JSFEAQ.0001179

Griffiths, T. (1958). A theory of rockstream morphology. *Annals of the Association of American Geographers*, *48*, 265–66.

Haeberli, W. (1985). *Creep of mountain permafrost: Internal structure and flow of alpine rock glaciers* [Doctoral dissertation, ETH Zürich].

Haeberli, W., Hallet, B., Arenson, L., Elconin, R., Humlum, O., Kääb, A., Kaufmann, V., Ladanyi, B., Matsuoka, N., Springman, S., & Mühll, D. V. (2006). Permafrost creep and rock glacier dynamics. *Permafrost and Periglacial Processes*, *17*(3), 189–214. https://doi.org/10.1002/ppp.561

Haeberli, W., Hoelzle, M., Kääb, A., Keller, F., Mühll, D. V., & Wagner, S. (1998). Ten years after the drilling through the permafrost of the active rock glacier murtel, eastern swiss alps : Answered questions and new perspectives. *55*, 403–410. https://api.semanticscholar.org/CorpusID:51799942

Haeberli, W., Huder, J., Keusen, H. R., Pika, J., & Röthlisberger, H. (1988). CORE DRILLING THROUGH ROCK GLACIER-PERMAFROST. https://www.researchgate.net/publication/245800726

Hinkel, K. M., & Outcalt, S. I. (1994). Identification of heat-transfer processes during soil cooling, freezing, and thaw in central alaska. *Permafrost and Periglacial Processes*, *5*(4), 217–235. https://doi.org/10.1002/ppp.3430050403

Hoelzle, M., & Haeberli, W. (1995). Simulating the effects of mean annual air-temperature changes on permafrost distribution and glacier size: An example from the upper engadin, swiss alps. *Annals of Glaciology*, *21*, 399–405. https://doi.org/10.3189/S026030550001613X

Hoelzle, M., Hauck, C., Mathys, T., Noetzli, J., Pellet, C., & Scherler, M. (2022). Long-term energy balance measurements at three different mountain permafrost sites in the swiss alps. *Earth System Science Data*, *14*(4), 1531–1547. https://doi.org/10.5194/essd-14-1531-2022

Hoelzle, M., Mühll, D. V., & Haeberli, W. (2002). Thirty years of permafrost research in the corvatsch-furtschellas area, eastern swiss alps: A review. *Norsk Geografisk Tidsskrift - Norwegian Journal of Geography*, *56*(2), 137–145. https://doi.org/10.1080/002919502760056468

Hoelzle, M., Wegmann, M., & Krummenacher, B. (1999). Miniature temperature dataloggers for mapping and monitoring of permafrost in high mountain areas: First experience from the swiss alps. *Permafrost and Periglacial Processes*, *10*, 113–124. https://doi.org/10.1002/(SICI)1099-1530(199904/06)10:23.0.CO;2-A

Ikeda, A., Matsuoka, N., & Kääb, A. (2008). Fast deformation of perennially frozen debris in a warm rock glacier in the swiss alps: An effect of liquid water. *Journal of Geophysical Research: Earth Surface*, *113*, 2007JF000859. https://doi.org/10.1029/2007JF000859

Ishikawa, M., Watanabe, T., & Nakamura, N. (2001). Genetic differences of rock glaciers and the discontinuous mountain permafrost zone in kanchanjunga himal, eastern nepal. *Permafrost and Periglacial Processes*, *12*(3), 243–253. https://doi.org/10.1002/ppp.394

Jansen, F., & Hergarten, S. (2006). Rock glacier dynamics: Stick-slip motion coupled to hydrology. *Geophysical Research Letters*, *33*(10), 2006GL026134. https://doi.org/10.1029/2006GL026134

Kääb, A., Haeberli, W., & Hilmar Gudmundsson, G. (1997). Analysing the creep of mountain permafrost using high precision aerial photogrammetry: 25 years of monitoring gruben rock glacier, swiss alps. *Permafrost and Periglacial Processes*, *8*, 409–426. https://doi.org/10.1002/(SICI)1099-1530(199710/12)8:43.0.CO;2-C

Kääb, A., Frauenfelder, R., & Roer, I. (2007). On the response of rockglacier creep to surface temperature increase. *Global and Planetary Change*, *56*(1), 172–187. https://doi.org/10.1016/j.gloplacha.2006.07.005

Kääb, A., Gudmundsson, G. H., & Hoelzle, M. (1998). Surface deformation of creeping mountain permafrost. photogrammetric investigations on murtèl rock glacier, swiss alps. *55*, 531–537. https://www.researchgate.net/publication/285889057

Keller, F. (1994). *Interaktionen zwischen schnee und permalrost: Eine grundlagenstudie im oberengadin.* (No. 127). Versuchsanstalt für Wasserbau, Hydrologie und Glaziologie. ETH Zürich.

Kellerer-Pirklbauer, A., Bodin, X., Delaloye, R., Lambiel, C., Gärtner-Roer, I., Bonnefoy-Demongeot, M., Carturan, L., Damm, B., Eulenstein, J., Fischer, A., Hartl, L., Ikeda, A., Kaufmann, V., Krainer, K., Matsuoka, N., Morra Di Cella, U., Noetzli, J., Seppi, R., Scapozza, C., ... Zumiani, M. (2024). Acceleration and interannual variability of creep rates in mountain permafrost landforms (rock glacier velocities) in the european alps in 1995–2022. *Environmental Research Letters*, *19*(3), 034022. https://doi.org/10.1088/1748-9326/ad25a4

Kellerer-Pirklbauer, A., Lieb, G. K., & Kleinferchner, H. (2012). A new rock glacier inventory of the eastern european alps. *Austrian Journal of Earth Sciences*, *105*(2), 78–93. https://ajes.at/images/AJES/archive/Band%20105_2/kellerer_at_al_ajes_105_2.pdf

Kenner, R., Pruessner, L., Beutel, J., Limpach, P., & Phillips, M. (2020). How rock glacier hydrology, deformation velocities and ground temperatures interact: Examples from the swiss alps. *Permafrost and Periglacial Processes*, *31*(1), 3–14. https://doi.org/10.1002/ppp.2023

Knight, J., Harrison, S., & Jones, D. B. (2019). Rock glaciers and the geomorphological evolution of deglacierizing mountains. *Geomorphology*, *324*, 14–24. https://doi.org/10.1016/j.geomorph.2018.09.020

Krainer, K., Bressan, D., Dietre, B., Haas, J. N., Hajdas, I., Lang, K., Mair, V., Nickus, U., Reidl, D., Thies, H., & Tonidandel, D. (2015). A 10,300-year-old permafrost core from the active rock glacier lazaun, southern ötztal alps (south tyrol, northern italy). *Quaternary Research*, *83*(2), 324–335. https://doi.org/10.1016/j.yqres.2014.12.005

Krainer, K., & Mostler, W. (2002). Hydrology of active rock glaciers: Examples from the austrian alps. *Arctic, Antarctic, and Alpine Research*, *34*(2), 142–149. https://doi.org/10.1080/15230430.2002.12003478

Lambiel, C., & Delaloye, R. (2004). Contribution of real-time kinematic GPS in the study of creeping mountain permafrost: Examples from the western swiss alps. *Permafrost and Periglacial Processes*, *15*(3), 229–241. https://doi.org/10.1002/ppp.496

Lugon, R., & Stoffel, M. (2010). Rock-glacier dynamics and magnitude–frequency relations of debris flows in a high-elevation watershed: Ritigraben, swiss alps. *Global and Planetary Change*, *73*(3), 202–210. https://doi.org/10.1016/j.gloplacha.2010.06.004

Martin, H. E., & Whalley, W. B. (1987). Rock glaciers: Part 1: Rock glacier morphology: Classification and distribution. *Progress in Physical Geography: Earth and Environment*, *11*(2), 260–282. https://doi.org/10.1177/030913338701100205

Merz, K., Maurer, H., Buchli, T., Horstmeyer, H., Green, A. G., & Springman, S. M. (2015). Evaluation of ground-based and helicopter ground-penetrating radar data acquired across an alpine rock glacier: Evaluation of ground-based and helicopter GPR. *Permafrost and Periglacial Processes*, *26*(1), 13–27. https://doi.org/10.1002/ppp.1836

Messerli, B., & Zurbuchen, M. (1968). Blockgletscher im weissmies und aletsch und ihre photogrammetrische kartierung. *Die Alpen SAC*, (3), 139–152.

Millar, C. I., & Westfall, R. D. (2008). Rock glaciers and related periglacial landforms in the sierra nevada, CA, USA; inventory, distribution and climatic relationships. *Quaternary International*, *188*(1), 90–104. https://doi.org/10.1016/j.quaint.2007.06.004

Mittaz, C., Hoelzle, M., & Haeberli, W. (2000). First results and interpretation of energy-flux measurements over alpine permafrost. *Annals of Glaciology*, *31*, 275–280. https://doi.org/10.3189/172756400781820363

Monnier, S., Camerlynck, C., & Rejiba, F. (2008). Ground penetrating radar survey and stratigraphic interpretation of the plan du lac rock glaciers, vanoise massif, northern french alps. *Permafrost and Periglacial Processes*, *19*(1), 19–30. https://doi.org/10.1002/ppp.610

Monnier, S., Camerlynck, C., Rejiba, F., Kinnard, C., Feuillet, T., & Dhemaied, A. (2011). Structure and genesis of the thabor rock glacier (northern french alps) determined from morphological and ground-penetrating radar surveys. *Geomorphology*, *134*(3), 269–279. https://doi.org/10.1016/j.geomorph.2011.07.004

Monnier, S., & Kinnard, C. (2013). Internal structure and composition of a rock glacier in the andes (upper choapa valley, chile) using borehole information and ground-penetrating radar. *Annals of Glaciology*, *54*(64), 61–72. https://doi.org/10.3189/2013AoG64A107

Moore, P. L. (2014). Deformation of debris-ice mixtures: DEFORMATION OF DEBRIS-ICE MIXTURES. *Reviews of Geophysics*, *52*(3), 435–467. https://doi.org/10.1002/2014RG000453

Mühll, D. V., & Haeberli, W. (1990). Thermal characteristics of the permafrost within an active rock glacier (murtèl/corvatsch, grisons, swiss alps). *Journal of Glaciology*, *36*(123), 151–158. https://doi.org/10.3189/S0022143000009382

Mühll, D. V., Stucki, T., & Haeberli, W. (1998). BOREHOLE TEMPERATURES IN ALPINE PERMAFROST: A TEN YEAR SERIES. *55*, 1089–1095. https://www.arlis.org/docs/vol1/ICOP/40770716/CD-ROM/Proceedings/PDF001189/164016.pdf

Muller, S. W. (1947). *Permafrost or permanently frozen ground and related engineering problems.* W. Edwards, Inc.

Mutter, E., & Phillips, M. (2012). Thermal evidence of recent talik formation in ritigraben rock glacier: Swiss alps, 479–483. https://www.researchgate.net/publication/234125372

Noetzli, J., & Pellet, C. (2023). *Swiss permafrost bulletin 2022* (No. 4). PERMOS. https://www.permos.ch/fileadmin/Files/publications/swiss_permafrost_bulletin/PERMOS_bulletin_2023.pdf

Noetzli, J., Arenson, L. U., Bast, A., Beutel, J., Delaloye, R., Farinotti, D., Gruber, S., Gubler, H., Haeberli, W., Hasler, A., Hauck, C., Hiller, M., Hoelzle, M., Lambiel, C., Pellet, C., Springman, S. M., Vonder Muehll, D., & Phillips, M. (2021). Best practice for measuring permafrost temperature in boreholes based on the experience in the swiss alps. *Frontiers in Earth Science*, *9*, 607875. https://doi.org/10.3389/feart.2021.607875

Noetzli, J., & Pellet, C. (2024). *Swiss permafrost bulletin 2023* (No. 5). PERMOS.

Nye, J. F. (1952). The mechanics of glacier flow. *Journal of Glaciology*, *2*(12), 82–93. https://doi.org/10.3189/S0022143000033967

Phillips, M., Buchli, C., Weber, S., Boaga, J., Pavoni, M., & Bast, A. (2023). Brief communication: Combining borehole temperature, borehole piezometer and cross-borehole electrical resistivity tomography measurements to investigate seasonal changes in ice-rich mountain permafrost. *The Cryosphere*, *17*(2), 753–760. https://doi.org/10.5194/tc-17-753-2023

Renette, C., Aalstad, K., Aga, J., Zweigel, R. B., Etzelmüller, B., Lilleøren, K. S., Isaksen, K., & Westermann, S. (2023). Simulating the effect of subsurface drainage on the thermal regime and ground ice in blocky terrain in norway. *Earth Surface Dynamics*, *11*, 33–50. https://doi.org/10.5194/esurf-11-33-2023

Roer, I., Kääb, A., & Dikau, R. (2005). Rockglacier acceleration in the turtmann valley (swiss alps): Probable controls. *Norsk Geografisk Tidsskrift - Norwegian Journal of Geography*, *59*(2), 157–163. https://doi.org/10.1080/00291950510020655

Scherler, M., Schneider, S., Hoelzle, M., & Hauck, C. (2014). A two-sided approach to estimate heat transfer processes within the active layer of the murtèl–corvatsch rock glacier. *Earth Surface Dynamics*, *2*(1), 141–154. https://doi.org/10.5194/esurf-2-141-2014

Schneider, S., Hoelzle, M., & Hauck, C. (2012). Influence of surface and subsurface heterogeneity on observed borehole temperatures at a mountain permafrost site in the upper engadine, swiss alps. *The Cryosphere*, *6*(2), 517–531. https://doi.org/10.5194/tc-6-517-2012

Schwarb, M., Frei, C., Schär, C., & Daly, C. (2000). Mean annual precipitation throughout the european alps 1971–1990. In *Hydrological atlas of switzerland.*

Spencer, A. (1900). A peculiar form of talus. *Science*, *11*(188).

Wahrhaftig, C., & Cox, A. (1959). ROCK GLACIERS IN THE ALASKA RANGE. *Geological Society of America Bulletin*, *70*(4), 383. https://doi.org/10.1130/0016-7606(1959)70[383:RGITAR]2.0.CO;2

Williams, M. W., Knauf, M., Caine, N., Liu, F., & Verplanck, P. L. (2006). Geochemistry and source waters of rock glacier outflow, colorado front range. *Permafrost and Periglacial Processes*, *17*(1), 13–33. https://doi.org/10.1002/ppp.535

Wirz, V., Gruber, S., Purves, R. S., Beutel, J., Gärtner-Roer, I., Gubler, S., & Vieli, A. (2016). Short-term velocity variations at three rock glaciers and their relationship with meteorological conditions. *Earth Surface Dynamics*, *4*(1), 103–123. https://doi.org/10.5194/esurf-4-103-2016

# 8 Appendix

## 8.1 Thermistors depths for each chain

Location of the thermistors in the 1987 borehole (first left), 2015 borehole showing all chains (second left), and then the locations of the sensors for each chain separately. Figure credit: Andreas Vieli.

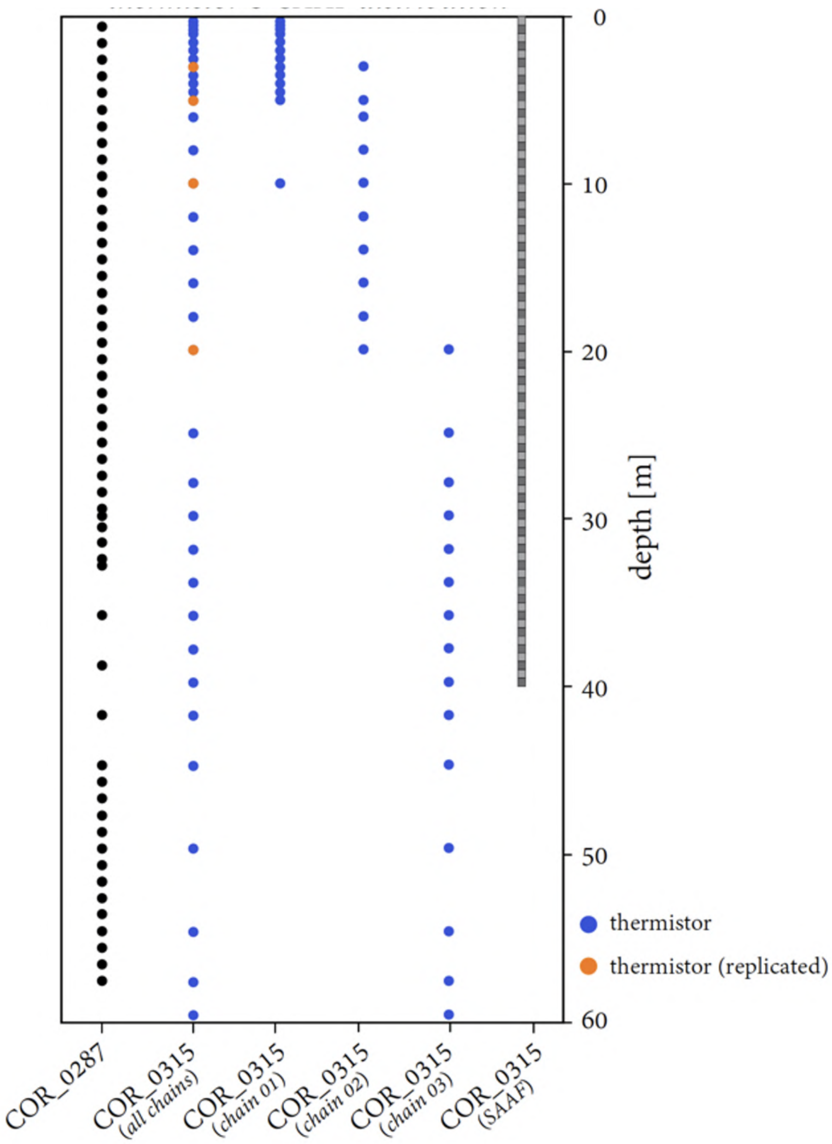

## 8.2 Layer-specific annual deformation trends

Linear regression analysis on the 2016 to 2023 period of annual layer-specific borehole deformation, showing the deceleration in shear zone deformation and the acceleration of the AL and ice-core deformation. Data source: PERMOS.

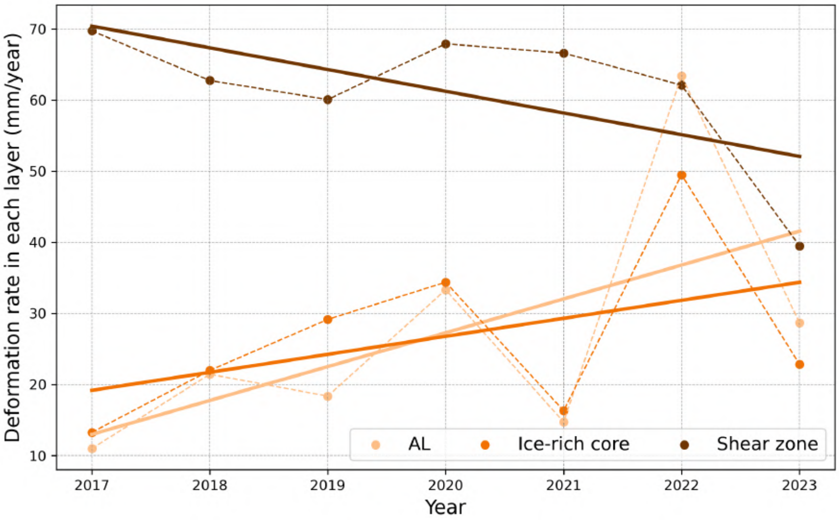

## 8.3 SAA temperature profiles

The shallow permafrost from 0 to 5 m monthly temperature profiles for each year from 2016 to 2023 measured by the SAA temperature sensors. The early winter snow accumulation from November to January is displayed for each year. Data source: PERMOS.

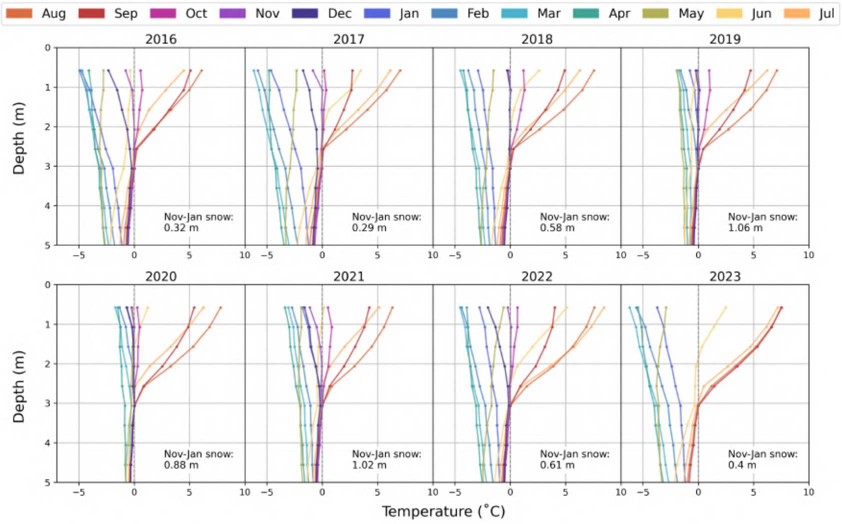

## 8.4 Timing of temperature and deformation peaks

The daily time series of air temperature (top), near-surface borehole temperature (middle), and surface velocity (bottom). The vertical dashed lines indicate the date of annual peaks for each variable to show that the velocity peaks happen shortly after the temperature peaks.

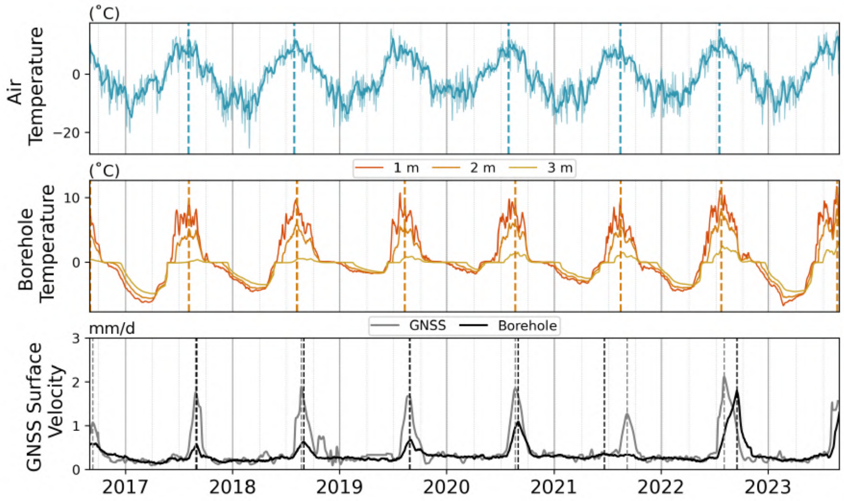

## 8.5 Annual deformation sensitivity to survey dates

Annual GNSS deformation calculated based on different date cut-offs: geodetic survey dates, end of August, middle of September, end of September, and middle of October. The daily GNSS deformation rate is plotted to show exactly when the surface deformation peaks occur. Data source: PermaSense.

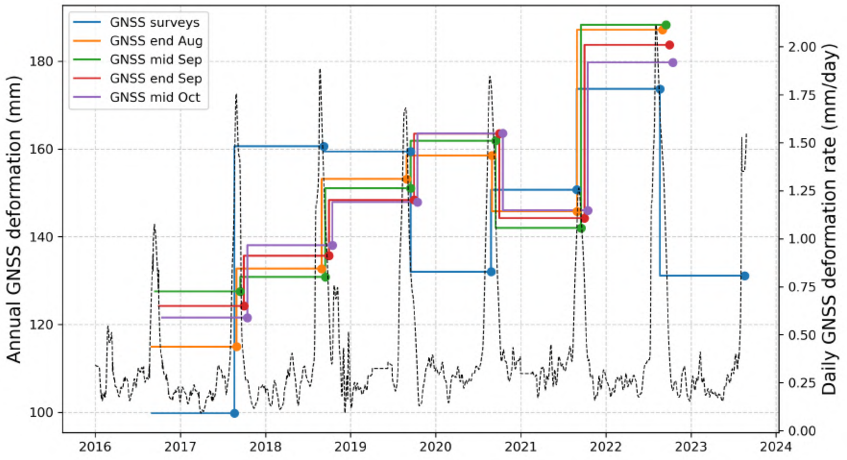

## 8.6 Inclinometer stretch potential

The sketch of the initial and final positions of the inclinometer chain (in green) with each layer (AL, ice-rich core, and shear zone) extracted to calculate the layer-specific chain stretch based on geometry. In the top left the estimated loss of 13 cm in elevation based on an average surface slope of 9° is calculated, resulting in an estimate of 45 cm of permafrost thinning over this time period, which is likely to be an overestimate.

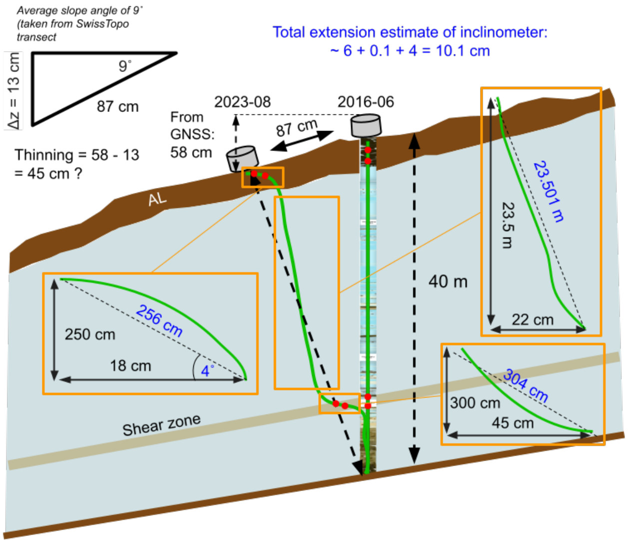

### 8.6.1 GNSS vertical displacement

The cumulative vertical displacement measured by the GNSS station at Murtèl rock glacier from 2016 to 2023. There is about 7 cm of vertical loss in elevation per year, which is made up of the downslope movement component and the ice thawing component. Data source: PermaSense.

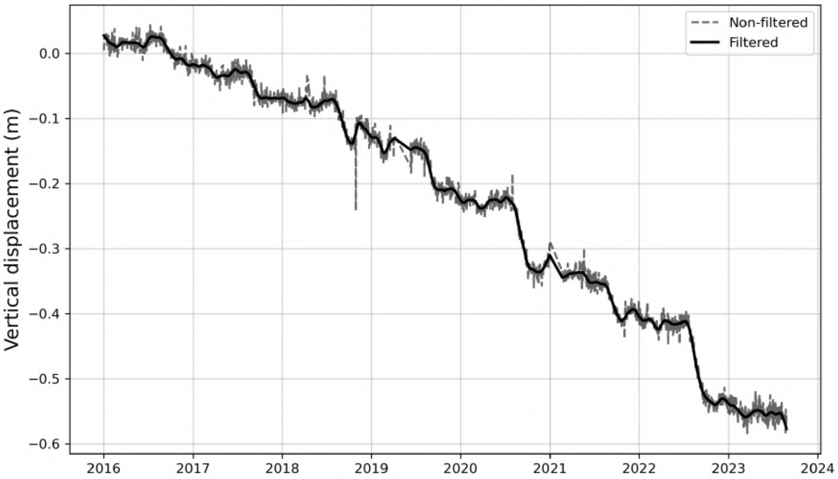
Non-filtered
Filtered
Vertical displacement (m)
0.0
−0.1
−0.2
−0.3
−0.4
−0.5
−0.6
2016
2017
2018
2019
2020
2021
2022
2023
2024

# Personal Declaration

I hereby declare that the submitted thesis is the result of my own, independent work. All external sources are explicitly acknowledged in the thesis.

Zurich, April 2025

Giulio Saibene